nature

SUPPLEMENTARY INFORMATION

https://doi.org/10.1038/s41586-018-0332-7

In the format provided by the authors and unedited.

Complex silica composite nanomaterials templated with DNA origami

Xiaoguo Liu[1,2,10], Fei Zhang[3,4,10], Xinxin Jing[1,10], Muchen Pan[1], Pi Liu[5,6], Wei Li[7], Bowen Zhu[1], Jiang Li[1,8], Hong Chen[9], Lihua Wang[1], Jianping Lin[5,6], Yan Liu[3,4], Dongyuan Zhao[7], Hao Yan[3,4]* & Chunhai Fan[1]*

[1]Division of Physical Biology and Bioimaging Center, Shanghai Synchrotron Radiation Facility, CAS Key Laboratory of Interfacial Physics and Technology, Shanghai Institute of Applied Physics, Chinese Academy of Sciences, University of Chinese Academy of Sciences, Shanghai, China. [2]School of Chemistry and Chemical Engineering, and Institute of Molecular Medicine, Renji Hospital, School of Medicine, Shanghai Jiao Tong University, Shanghai, China. [3]Center for Molecular Design and Biomimetics, Biodesign Institute, Tempe, AZ, USA. [4]School of Molecular Sciences, Arizona State University, Tempe, AZ, USA. [5]State Key Laboratory of Medicinal Chemical Biology, College of Pharmacy and Tianjin Key Laboratory of Molecular Drug Research, Nankai University, Haihe Education Park, Tianjin, China. [6]Biodesign Center, Tianjin Institute of Industrial Biotechnology, Chinese Academy of Sciences, Tianjin, China. [7]Department of Chemistry, Laboratory of Advanced Materials, Shanghai Key Lab of Molecular Catalysis and Innovative Materials, iChEM and State Key Laboratory of Molecular Engineering of Polymers, Fudan University, Shanghai, China. [8]Shanghai Key Laboratory of Green Chemistry and Chemical Processes, School of Chemistry and Molecular Engineering, East China Normal University, Shanghai, China. [9]Pen-Tung Sah Institute of Micro-Nano Science and Technology, Xiamen University, Xiamen, China. [10]These authors contributed equally: Xiaoguo Liu, Fei Zhang, Xinxin Jing. *e-mail: hao.yan@asu.edu; fchh@sinap.ac.cn

Supplementary Information for

Complex silica composite nanomaterials templated with DNA origami

Xiaoguo Liu[1,6†], Fei Zhang[2,7†], Xinxin Jing[1†], Muchen Pan[1], Pi Liu[3,8], Wei Li[4], Bowen Zhu[1], Jiang Li[1,9], Hong Chen[5], Lihua Wang[1], Jianping Lin[3,8], Yan Liu[2,7], Dongyuan Zhao[4], Hao Yan[2,7*], Chunhai Fan[1*]

[1]Division of Physical Biology and Bioimaging Center, Shanghai Synchrotron Radiation Facility, CAS Key Laboratory of Interfacial Physics and Technology, Shanghai Institute of Applied Physics, Chinese Academy of Sciences, University of Chinese Academy of Sciences, Shanghai 201800, China

[2]Center for Molecular Design and Biomimetics, Biodesign Institute, Tempe, Arizona 85287, USA

[3]State Key Laboratory of Medicinal Chemical Biology, College of Pharmacy and Tianjin Key Laboratory of Molecular Drug Research, Nankai University, Haihe Education Park, 38 Tongyan Road, Tianjin 300353, China

[4]Department of Chemistry, Laboratory of Advanced Materials, Shanghai Key Lab of Molecular Catalysis and Innovative Materials, iChEM and State Key Laboratory of Molecular Engineering of Polymers, Fudan University, Shanghai 200433, China

[5]Pen-Tung Sah Institute of Micro-Nano Science and Technology of Xiamen University, Xiamen University, Xiamen, 361005, China

[6]School of Chemistry and Chemical Engineering, and Institute of Molecular Medicine, Renji Hospital, School of Medicine, Shanghai Jiao Tong University, Shanghai 200240, China

[7]School of Molecular Sciences, Arizona State University, Tempe, Arizona 85287, USA

[8]Biodesign Center, Tianjin Institute of Industrial Biotechnology, Chinese Academy of Sciences, Tianjin 300308, China

[9] Shanghai Key Laboratory of Green Chemistry and Chemical Processes, School of Chemistry and Molecular Engineering, East China Normal University, 500 Dongchuan Road, Shanghai, 200241, China

These authors contributed equally to the work[†]

Corresponding authors[*]: fchh@sinap.ac.cn, hao.yan@asu.edu

This PDF file includes:

Other Supplementary Material for this manuscript includes the following:

Methods

Materials. Staple DNA strands were purchased from Jie Li Biology Co. Ltd (Shanghai, China). Scaffold DNA strands were purchased from New England Biolabs. All DNA strands were stored at -20 °C in DNA LoBind Tubes which were purchased from Eppendorf North America Inc. N-trimethoxysilylpropyl-N, N, Ntrimethylammonium chloride (TMAPS) (50% in methanol) and tetraethyl orthosilicate (TEOS) were purchased from TCI, Japan. Other chemicals were purchased from Sinopharm and Sigma-Aldrich. Carbon/silicon nitride-film-coated copper grids were purchased from Beijing Zhongjingkeyi Technology Co., Ltd (Beijing, China). Amicon Ultra-0.5 mL centrifugal filters were purchased from Merck Millipore Ltd. Tullagreen, Carrigtwohill Co. Cork Ireland. AFM tips were purchased from Bruker. All of the regents were used as received without further purification. All of the experimental consumables were used as received.

Preparation of DNA nanostructure. Newly designed DNA structures and sequences were created with the Tiamat software[1]. Other DNA nanostructure templates were prepared according to the published works[2-9]. A set of nanopores with predesigned sizes (11 × 13 nm, 25 × 33 nm, 31 × 44 nm) in a rectangle were achieved by removing specific staples from a rectangle origami. To fold the DNA origami, staple strands were mixed with the respective scaffold strands in a molar ratio of 10:1 in Tris-EDTA-Mg^{2+} buffer. To fold the DNA tile nanostructures, DNA strands were mixed in a specific ratio in Tris-EDTA-Mg^{2+} buffer. The strand mixture was annealed in a PCR thermo cycler (Eppendorf) in the respective protocol. All DNA ratios, buffer and annealing protocols are summarized in Tab. S3. To remove excess staples, an origami solution was washed at least 3 times with the synthetic buffer using an Amicon Ultra-0.5 mL centrifugal filter (MWCO 100 kDa) at a speed of 3000 g for 10 min. The DNA tile nanostructures were directly used without further purification.

DOS protocol. In a typical experiment, 2% (v/v) TMAPS (50% in methanol) and 2% (v/v) TEOS were added slowly to a Tris-EDTA-Mg^{2+} buffer while vigorously stirring. The mixture was stirred for 30 min at 25 °C to ensure sufficient pre-hydrolysis occurred. Then, a certain amount of this gel solution was transferred to an appropriate container (a 2.5 ml centrifuge tube for copper grids, a watch-glass for mica and silicon wafer). Meanwhile, 10 µL of the purified DNA samples were adsorbed onto substrates (either glow-discharged carbon/silicon nitride-film-coated copper grids, silicon wafer or a sheet of freshly cleaved mica) for 3 min. Next, the substrates were rinsed using their respective buffer to remove the excess DNA and then placed faced-down on the gel solution in the container. After this, the gel solutions with substrates were transferred to a thermo mixer (Eppendorf) instrument to react at 300 rpm (25 °C) for 1 hour, and then allowed to react under static conditions at 25 °C for several days. The surface with the DOS complex was washed with ethanol and deionized water to remove the unreacted reagents (DNA, TMAPS and TEOS).

Gel Electrophoresis. For the DNA origami, a 0.5% agarose (BioRad) gel containing 1×GelRed nucleic acid gel stain in 1×TAE-Mg^{2+} buffer (40 mM Tris, 2 mM EDTA, 12.5 mM $MgAc_2$) was run on an electrophoresis system in an ice-water bath and visualized under UV light. For other DNA nanostructure, a 6% polyacrylamide gel in a 1×TAE-Mg^{2+} buffer was run on an electrophoresis system in an ice-water bath. Gels were stained with a 1×GelRed nucleic acid gel stain before imaging.

Preparation of DNA functionalized AuNRs: Binary surfactant mixtures were used to synthesize the gold nanorods according to previous studies[10]. Thiolated ssDNA obtained from Takara Bio Inc. was added to an AuNRs

solution containing 1 × TBE buffer with a molecular ratio of 5,000: 1. 0.01% (w/v) SDS was added to avoid binding between AuNRs and tube wall. After incubating at 25 °C for 4 hours, the solution was brought to 0.5 M NaCl over 4 h. Then, the solution was transferred to a thermo mixer (Eppendorf) instrument to react at 300 rpm (25°C) for 12 h. After that, the AuNRs-DNA conjugates were collected by centrifugation and washed with 1 × TBE buffer three times to remove excess ssDNA.

Immobilization of AuNRs on DNA origami:
The ssDNA-modified AuNRs were mixed with purified DNA origami with a 5: 1 molecular ratio. The final Mg^{2+} concentration was raised to 12 mM by adding a 100 mM $MgCl_2$ solution. The mixture of ssDNA-modified AuNRs and DNA origami was annealed from 45 °C to 15 °C at a rate of 10 min/°C.

FTIR and Raman scattering. The chemical bond information of the sample was revealed by FTIR along with Raman scattering. After 1 d, 2 d, and 5 d of silicification, the DOS triangle precipitate was washed with H_2O/EtOH, and then cryodesiccated. The sample powders were weighed at 1.2 mg, 1.7 mg and 2.7 mg, corresponding to the 1 d, 2 d, and 5 d products, respectively.

Raman scattering measurements were performed on a HR800 Raman microscope instrument (HORIBA, Jobin Yvon, France) using the standard 785 nm HeNe 20 mW laser with a laser spot size of 500 nm. All of the Raman scattering spectras were obtained using the same parameters (objective: 60× NA 0.7, acquisition time: ~ 10 s, hole: ~ 300, slit: ~ 200, grating: ~ 600 g/mm). The DOS triangle sample and the standard SiO_2 sample were prepared by dispersing them into EtOH at a concentration of 1 mg/100 μL. Then, suspensions were dropped onto the gold substrate. After drying at room temperature, the Raman scattering signals of the samples were collected. LabSpec 5 software was used for Raman data acquisition and data analysis.

The IR spectra measurements of the DNA solution were performed on a Fourier transform infrared spectrometer (Perkin-Elmer LR 64912C). The DNA triangle origami sample without silicification was measured in solution. H_2O signal was eliminated by using a dual optical path detection system.

Bruker Optics TENSOR 27 FT-IR Spectrometer with a horizontal multi-rebound attenuated total reflection (ATR) was used to characterize the samples in the wavenumber range of 4000-400 cm^{-1}. The DOS samples and SiO_2 standard sample were prepared with highly pure potassium bromide tableting. Spectra were recorded using the average of 32 scans and a 4 cm^{-1} resolution.

TEM characterization. For DNA imaging, 10 μL of purified DNA samples were adsorbed onto glow discharged, carbon-film-coated copper grids for 3 min. The sample drop was wicked from the copper grids with a filter paper (making sure the copper grids were not dried completely) and then the sample were stained for 40 seconds using a 0.75% aqueous uranyl formate solution. After this, the excess solution was removed with a filter paper and the copper grids were allowed to dry at 25 °C. For DOS imaging, the washed copper grids with the DOS complexes were dried at 25°C. In addition, the calcined DOS samples were loaded onto silicon nitride-film-coated copper grids. Imaging was performed using a FEI Tecnai G2 F20 S-TWIN operated at 200 kV.

SEM and STEM characterization. SEM images, STEM images and EDX mapping data were obtained with a FEI MAGELLAN 400 STEM that was equipped with an Oxford X-Max^n EDS detector. For SEM characterization, all DOS samples were loaded directly onto copper grids or silicon wafers without further coatings. To reduce the electron damage, samples were imaged under low voltage ranging from 350 V to 10.0 kV. For STEM

characterization, parallel samples on copper grids were characterized by TEM.

AFM characterization. All AFM images were obtained using a Multimode Nanoscope VIII instrument (Bruker). For imaging DNA origami/nanostructures in fluid, 5 µL of purified samples were deposited onto a freshly cleaved mica and left to adsorb for 3 min. Their respective synthetic buffer was added to the mica and the sample was scanned with “Peak Force QNM in fluid” mode using Scanasyst-Fluid+ tips (Bruker). The applied force was precisely tuned to acquire high resolution images by changing the Peak Force Setpoint. To promote a stronger bond between the DNA samples (6-helix bundle, tetrahedron, honeycomb, DNA diatom) and the mica surface, 10 mM $NiCl_2$ was used in the imaging buffer. For DNA imaging in air, the sample drop was washed off with 100 µL of deionized water after absorption and dried with compressed air. The sample was scanned in “Scanasyst in air” mode with RTESPAW-MPP-11120-W, Veeco.

For the DOS sample, the washed mica with the DOS complex was immobilized on an iron sheet and then imaged with “Peak Force QNM in fluid” mode. Scanasyst-Fluid+ tips with a spring constant (K) of 0.7 N/m were used to measure the *E*-modulus of the DNA and DOS samples. The modulus ranged from several MPa to hundreds of MPa. The tip radius (R), spring constant (K) and deflection sensitivity were determined using standard sapphire samples (Bruker) and calculated using Veeco software. The average tip radius was found to be approximately 2 nm[11]. For damage resistance and modulus measurement, the forces ranging from 150 pN to 3,000 pN were used to scan samples in the same area in order to obtain enough force curves to exclude the substrate effect on such thin samples (~ 2 nm to ~ 7 nm thickness). For mechanical measurements of the tetrahedron DOS complex, cycling forces switching from 1.0 nN to 3.0 nN were used until the sample was destroyed.

Nanomechanical data processing. We collected data from an AFM indentation experiment on a sample on a rigid substrate with Scanasyst-Fluid+ tips as shown in Supplementary Fig. 58a. The collected Force-Separation Curve is from a ramping process, whereby the scanner’s vertical position was typically plotted against the separation along the retraction (Supplementary Fig. 58b). However, due to the thinness of the sample (several nanometers), the nanomechanical properties could not be properly handled with the classical fitting method. Thus, we introduced the following MSEC method to solve this problem.

The z-direction separation is mainly contributed by cantilever deflection and sample indentation, in which, only sample indentation represents an inherent mechanical property of the sample for *E*-modulus calculations as described by the following equation:

$$\Delta z = \Delta d + \delta \quad (1)$$

Δz *z*-direction separation

Δd cantilever deflection

δ sample indentation

Where *E*-modulus can be deducted from the sample indentation (δ) and force (F). Normally, when the sample is thick enough, the cantilever deflection is far smaller than the sample indentation ($\Delta d << \delta$) so its influence on the *E*-modulus value can be ignored ($\Delta z = \Delta d + \delta \approx \delta$). In our case, however, the sample is about 5 nm thick ($t \approx 5$ nm) and the cantilever deflection is of the same order of magnitude as the sample indentation[12]. If the cantilever deflection is still considered as part of the indentation, the sample indentation would be considerable higher than the real value, which would lead to fake results that the *E*-modulus increases together with the indentation force (Supplementary Fig. 58c).

In order to exclude the cantilever deflection from the separation, we use the following equation:

$$\delta_f(F) = \Delta z_f(F) - \Delta z_s(F) \quad (2)$$

$\Delta z_f(F)$ Force-Separation curve of tip-sample

$\Delta z_s(F)$ Force-Separation curve of tip-substrate

$\delta_f(F)$ Force-Indentation curve of tip-sample

From Eq. 1, we can get

$$\Delta z_f(F) = \Delta d(F) + \delta_f(F) \quad (3)$$

Because the mica substrate is much stiffer than the DNA-Diatom, as shown in Tab. S7, the cantilever deflection contributes mainly to the tip-substrate separation ($\Delta z_s(F) \approx \Delta d(F)$). Therefore, we subtracted the tip-substrate curve from the tip-sample curve, to exclude the deviation brought about by the cantilever deflection, to finally obtain the tip-sample Force-Indentation curve (Supplementary Fig. 59)[13].

In order to find the probe adhesive force, we used the retraction curve. For simplification, the Force-Separation curve is already included the adhesive force. We can then divide the sample Force-Indentation curve into three steps, as shown in Supplementary Fig. 59.

The 1st step is when the tip just comes into contact with the sample surface. During this step, the tiny deformation of the sample brings resistance to the tip. The indentation force starts to slowly increase, and prevents the tip from going down.

After that, in the 2nd elastic deformation step, the tip reaches equilibrium. During this step, the resistance force on tip completely accounts for the sample elastic deformation, and this relationship with the indentation can be described by the Derjaguin-Muller-Toporov (DMT) model[14], which is the following equations:

$$F(\delta) = F_i(\delta) - F_{ad} = \frac{4}{3}E^*\sqrt{R^*}\delta^{\frac{3}{2}} \quad (4)$$

Where:

$$\frac{1}{E^*} = \frac{1-v_t^2}{E_t} + \frac{1-v_f^2}{E_f} \quad (5)$$

$$\frac{1}{R^*} = \frac{1}{R_t} + \frac{1}{R_f} \quad (6)$$

F_i indentation force

F_{ad} adhesive force

δ sample indentation

E_t *E*-modulus of tip

E_f *E*-modulus of sample

v_t Poisson's ratio of tip

v_f Poisson's ratio of sample

R_t radius of tip

R_f radius of sample, ∞

The DMT model is an alternative model for adhesive contact, which assumes that the contact profile remains the same as in Hertzian contact[15] but with additional attractive interactions outside of the area of contact. However, this model will become increasingly inaccurate when applied to thin samples, as the ratio of sample indentation to sample thickness increases, because of the increasing proportion of the elasticity of the substrate material underlying the sample. The influence of the substrate can be taken into account by replacing Eq. 5 with the following function[16-18]:

$$\frac{1}{E^*} = \frac{1-v_t^2}{E_t} + \frac{1-v_f^2}{(1-e^{-\alpha t/\delta})E_f} + \frac{1-v_s^2}{e^{-\alpha t/\delta}E_s} \quad (7)$$

E_s E-modulus of substrate

v_s Poisson's ratio of substrate

t sample thickness

α constant, related to the tip shape and range of sample indentation/ thickness

Eq. 3 and Eq. 5 have the same physical meaning, the only difference is that the former equation applies to the situation when t/δ approaches infinity as described by the following equation:

$$\lim_{\frac{t}{\delta}\to\infty} \frac{1}{E^*} = \lim_{\frac{t}{\delta}\to\infty} \left(\frac{1-v_t^2}{E_t} + \frac{1-v_f^2}{\left(1-e^{-\frac{\alpha t}{\delta}}\right)E_f} + \frac{1-v_s^2}{e^{-\frac{\alpha t}{\delta}}E_s} \right) = \frac{1-v_t^2}{E_t} + \frac{1-v_f^2}{E_f} \quad (8)$$

Finally, in the 3rd step, inelastic deformation occurs and the DMT model no longer reliably describes this step.

The generality of the thin films in our MSEC method was further verified by COMSOL simulation using 5.0 nm thick polypropylene (PE) nanofilm with a gradually increasing *E*-modulus. The (PE) nanofilm were used as standard materials (from 100 MPa to 900 MPa, at increments of 100 MPa, Supplementary Fig. 60). A cone with a hemispherical bottom representing the parameters of the Scanasyst-Fluid+ AFM tip was constructed. PE nanofilm was placed onto a 5.0 nm thick mica surface.

Setup of COMSOL software: Solid mechanics module was utilized. The tip, PE and mica were set as linear elastic materials, in which mica was the fixed constraint.

Data collecting:

(1) Sample simulation. A prescribed displacement (sample separation, Δz) was given by the tip, which was pointed to the minus direction of z axis. Stationary study was performed. The balanced status was obtained as illustrated in Supplementary Fig. 60. The pressure was deducted from surface integral of the contact area between tip and PE. For a certain sample, the indentation process was simulated by changing the value of Δz. $\Delta z_f(F)$ in equation 2 was obtained. (2) Substrate simulation. All the steps were the same as (1), except PE was removed. The tip directly contacted with mica substrate, and $\Delta z_s(F)$ in equation 2 was obtained.

Data analyzing followed the prescribed MSEC and DMT methods.

MD simulation. Because simulating an entire DNA origami is time consuming (due to its giant molecular size), we first used a full atomic MD simulation to investigate the molecule behavior of TMAPS, TEOS and 12 bp dsDNA strands, followed by a larger 348 bp DNA origami fragment, and then finally using a coarse grain MD simulation to investigate the condensation behavior of the DOS system.

A total of five systems was used to carry out the full atomic MD simulation. These MD simulations were carried out with the software Amber 16. The following parameters were used in our simulations: ff14SB force fields with parambsc0 corrections and Mg^{2+} parameters of Li/Merz[19-21]. The details of the atomic systems are given in Supplementary Tab. S1. The total chare of T_{32} molecular is 1.2 times that of the DNA, while the concentration of the Mg^{2+} ions was set to 12.5 mM, which represented the typical cation concentration for DNA origami folding. Cl^- ions were added to neutralize the charge of the systems. The electronic parameters of T_{32} were generated by software antechamber with charge method AM1-BCC. Parameters of bonds, angles were obtained from: http://www.chem.hope.edu/~discus/muccc/muccc2/MUCCC2-Schorb/. The dihedral parameters of sp3 carbon were copied for silicon. The temperatures of all of the systems were first minimized and then heated to 300K. Then

MD production runs were carried out with an integration time step of 2 fs. Particle mesh Ewald (PME) technique was used to treat the long-range interaction with a 10 Å cutoff for the short-range nonbonded interactions[22]. SHAKE algorithm was used to increase the integration time step. A Berendsen weak coupling thermostat was applied to maintain the temperature constant at 300 K. In systems 1-4, a 5 ns npt MD simulation was performed. In system 5, a 20 ns npt MD simulation was performed. The results are shown in Supplementary Fig. 5.

We used a martini coarse grain force field to simulate the interactions between the DNA origami and the T_{32} molecules. To turn the entire atomic structure into a coarse grain structure, the NC_4, C-C-Si-O-C, O-C, O-Si-O, O-C-C was set as beads Q0, C5, N0, C5, N0. The parameters for the bonds and angles were decided by using the statistical data that was created from the full atomic structure. The detailed building strategy can be found on the martini coarse grain website: http://cgmartini.nl/index.php/tutorials-general-introduction-gmx5/parametrzining-new-molecule-gmx5.

The full atomic DNA origami was initially built with a Cando server. Then, the improper tension of the structure was released by a full atomic MD simulation that was carried out on the Amber 16 software. After 2 ns amber MD simulations, the structure was translated into a coarse grain model with a martinize_v2.1P-dna.py python script, which was provided by the martini coarse grain web site. The “all-soft” DNA type was selected in order to create the initial structure.

Gromacs 2016-3 was used to simulate the CG system[23]. The whole simulation system was constructed with six parts: one DNA origami, 300 T_{32} molecules, 100 hydrated Mg^{2+} beads, 346 hydrated Cl^- beads, 105890 polarizable water[24] and 21600 hydrophobic C1 beads. The 21600 C1 beads were organized in a plate form with face-centered cubic packing and frozen to its original place to simulate a monocrystalline silicon plane. The simulation temperature and pressure was set to 310 K and 1 atm using Velocity rescale thermostat and Berendsen barostat[25,26]. Long-range electrostatics were included using PME, the relative permittivity was set to $\varepsilon_r = 2.5$. A real-space cut-off of 1.2 nm, and a 0.12 nm Fourier grid spacing were used for PME. After the energy minimization, the whole system was equilibrated for 50 ns with dt = 0.002 ps, then dt was increased to 0.01 ps for another 100 ns MD simulation, finally the dt was increased to 0.02 ps for the last 200 ns MD simulation.

Additional Discussion

1. Detailed DOS strategy

Our study for the first time created a precise silicification of complex structures at the nanoscale level and with high programmability. We note that previously reported silica structures were either at the micrometer scale or without well-defined features[27]. The use of well-defined DNA origami structures leads to a completely different charge distribution for DNA-TEOS interactions, given that the stiffness of DNA origami exceeds that of natural ds/ssDNA by several orders of magnitude[28,29]. The even distribution of negative charges on the DNA origami provides spatially organized nucleation sites for subsequent silicification, which is absent in more flexible ds/ssDNA. The introduction of the pre-hydrolyzing clustering process in our DOS strategy facilitates the deposition of amorphous silica on complex DNA nanostructures by generating prehydrolyzing clusters that compete with cations in solution for DNA binding. This mechanism, as substantiated by both MD simulation and experimental data (Fig. 1b and 1c, Supplementary Fig. 4-13), is the key to the successful formation of complex DOS structures. In fact, we find it difficult to directly apply previously reported methods for use with the DNA origami nanostructure system. As a negative control, if we simply use previous methods, we cannot form a precise silica layer on any DNA nanostructure (Supplementary Fig. 4 and 9). It is important to note that the reasons for the failures of the previous method, as well as the success of our current method, come from two factors. First, maintaining the folding of DNA strands in DNA nanostructures needs a much stronger cation concentration[2,30,31], which prevents cationic silanes from attaching onto the backbone of dsDNA strands, which further jeopardizes subsequent mineralization. Therefore, the free nucleation of TEOS molecules will happen in the solution (as indicated in Fig. 1c), inducing the DNA template-independent mineralization to occur. Second, only pre-folded DNA nanostructures could provide sufficient surface areas and enough negative charge density to recruit pre-hydrolyzing clusters prior to their self-aggregation with free TEOS in the bulk solution[32,33].

2. Surface roughness of DOS

The observed smoothness of the mineralized structures mainly arises from the following factors. Homogeneously distributed negative charges on the surface of the DNA nanostructures (Supplementary Fig. 10) that suggests that the pre-folded DNA origami nanostructures provide a well-defined surface area with evenly distributed negative charges that are used to recruit pre-hydrolyzing clusters prior to the occurrence of self-aggregation that may be due to the free TEOS in the bulk solution. Optimized experimental reaction conditions, including a low concentration of TEOS molecules and appropriate mineralization time. The Ra values for 2D DOS structures vary in the range from ~ 0.4 nm to ~ 0.7 nm, which indicates that the surface roughness corresponds to a one- or two-layer difference in the silica tetrahedron since the bond length of Si - O is 166 pm.

The DOS cube had rougher surfaces than the tetrahedron with the same DNA bundle diameters. We believe the reason lies in the different mechanical properties of the DNA origamis. Given that the stiffness of a given object increases remarkably along with its effective radius, but decreases inversely proportional to its length[28,29], the structural features of different DNA origami resulted in different mechanical properties and subsequently different surface roughness. In particular, the cube framework is an unstable polygon that can be easily deformed/affected by an external force, such as a stirring force during the mineralization reaction. Hence, a small distortion of the DNA nanostructures is unavoidable and often comes from the inherent geometric features of the target structures. This result further substantiates that the stiff structures of the DNA origami facilitate the overall smoothness as observed in our work.

3. Detailed DOS information

Compared to the DNA masked lithography or the chemical vapor deposition (CVD) method, our method showed a great improvement for the morphology preservation ability for both 2D and 3D structures[34,35]. For these previously reported methods, the accuracy of 2D patterning is heavily affected by the uncontrollable shrinkage of DNA origami when they are dried in air. For 3D DNA constructions, the fragile DNA molecules always collapse or become distorted when they are placed on surfaces, even with the help of a polymer coating[4,36-38]. On the contrary, our method that uses a solution reaction preserved the intrinsic structure of both 2D and 3D DNA frameworks with minimal deformation. TEM characterization confirmed the detailed configurations of the free-standing cubic and tetrahedron DOS, as viewed from different directions by tilting the sample holder (see Supplementary Videos 1-3). Their TEM images revealed that, while on a substrate, DOS nanostructures have a quite different behavior than their original 3D DNA templates, which were always pressed flat, distorted, and laid down on the carbon film surface (Fig. 3a, Supplementary Fig. 43 and 44). These data indicate that our silicification process is mild enough to preserve the configurations of prescribed DNA frameworks well.

The silica growth kinetics was illustrated by statistically analyzing the changes in the edge thickness of one of the honeycomb structures with increasing time periods (Supplementary Fig. 45-48). It showed that the silicate interaction almost reached equilibrium after 5 days of growth. The final structures had an average ~ 9.0 nm thick edges, indicating that there was a ~ 2.0 nm thick silica layer on each side, which is consistent with the ~ 2.0 nm height change profiles obtained by AFM characterization (Supplementary Fig. 49). The tunability of the silica shell thickness was further discussed in Tunability of shell thickness and Supplementary Fig. 50.

The shape resolution limit of our DOS methods is currently restricted to a DOS tetrahedron with a side length of 42 bp (~ 16 nm). Although it is clearly visible under TEM imaging, the resolution is not sufficient to discern concrete structural features (Supplementary Fig. 51). The longest bundle-shaped DOS that was successfully created is ~ 1.0 μm in length (Supplementary Fig. 52). These results demonstrate that our system is able to grow DOS with a wide range of lengths from a nano to micro, or even macro scale.

4. Tunability of shell thickness

By taking the silicification of the honeycomb structure as an example, we demonstrated that our method could be tuned in the range of 2-4 nm. However, further silicification results in thicker silica shells that cannot maintain the fine geometric features of the DNA origami structures. Theoretically, when trying to replicate the shape of DNA origami, the coating thickness of the DOS is restricted by the different geometric parameters of the DNA origami nanostructures. Complete globoid structures, such as ellipsoid ones, could be coated by a thicker silica layer without losing their structural features by increasing mineralization time or by adding TEOS molecules later in the process. This is similar to what occurred in the listed reference, which used gold NPs as growing cores. Incomplete globoid and other angular structures, such as triangles, squares, crosses, toroids, hemispheres, tetrahedrons, honeycombs and diatom-mimicking structures, lose their geometric features as the thickness of their silica shells increase, mainly for two reasons: 1). For those with pores, inner curved areas, and framework structures, the over growth of the silica will eventually fill in the internal space. 2). For those with angles and corners, the chamfering degree will increase gradually as each new coated silica layer forms, which will eventually result in a curved structure. In addition, we have utilized an isoperimetric inequality function to simulate the possible growth trends of a silica shell on a 2D planar square and on cross shapes to better understand the growth process (Supplementary Fig. 50).

Given the above considerations, we have selected the 2 nm coating experimental conditions as our standard

protocol to obtain DOS structures with improved mechanical properties without sacrificing the copy shape accuracy.

5. Yield

The yield of the silicification process was defined as the ratio between the number of intact DOS nanostructures and the total number of resulting monomers in the TEM images. Additionally, the reported yields of 2D DNA frameworks (triangle, rectangle and cross), 3D DNA frameworks (tetrahedron, cube), and curved DNA nanostructures (hemisphere, toroid and ellipsoid) were ~ 90%, 20 ~ 45%, and 80 ~ 96%, respectively[2-4,7]. The DOS strategy performed well on all DNA nanostructures, and the yield of well-formed DNA-silica included one third to more than one half of the total monomers. The aggregation of the DNA nanostructures were mainly attributed to their own structural features and base stacking forces. Therefore, the bottleneck for the total yield could be attributed to how rigid and dispersive the DNA frameworks were, e.g. triangle versus square, tetrahedron versus cube.

Yield for different shaped DOS nanostructures

Yield refer to the various DOS nanostructures in Fig. 3b and was calculated as the ratio between well-formed DOS nanoparticles to the total number of DOS observed. Only discrete monomers were taken into consideration, see Supplementary Fig. 53–56 for details.

Shape	yield
Triangle	53%
Rectangle	40%
Cross	38%
Tetrahedron	65%
Cube	33%
Hemisphere	61%
Toroid	66%
Ellipsoid	58%
Diatom	40%

6. 2D nanomechanical properties

One of the most important biological functions of diatom cell walls in nature is purely mechanical, simply for the protection of the cell. Our DOS nanostructures have been examined and they exhibited significantly enhanced mechanical properties as compared with their DNA origami templates. Taking a triangular shaped DOS as an example, the *E*-modulus data was derived from the force-distance curves of AFM data (Supplementary Fig. 57). The averaged *E*-modulus of pure DNA origami is about 100 MPa (Fig. 4a), which agrees with previous studies on the radial compression elasticity of single DNA molecules[39]. We combined a substrate effect subtraction and a Derjaguin−Muller−Toporov (DMT) model refinement together, which resulted in a membrane substrate effect correction (MSEC), to obtain reliable mechanical statistics (Fig. 4b, see details in methods and Supplementary Fig. 58-60, Tab. S7). For DOS triangles with 1 and 5 days growth time, the typical *E*-modulus increased dramatically to 1.0 and 1.2 GPa, respectively. It should be noted that there were two sets of *E*-modulus distributions for both 1 and 5 days DOS samples, which represented naked DNA and DNA-silica, respectively (Fig. 4a). A possible reason for this phenomenon comes from the partial silica deposition occurring on the DNA plane surface. We indeed observed irregular pores on the calcined sample after adding calcine to the DOS sample under 600 °C. DNA frameworks were burnt down (Supplementary Fig. 61).

Based on the *E*-modulus data, it was expected that the compression strength of the DOS nanostructures would be greatly enhanced. We applied increasing AFM tip forces to test the mechanical property of both the pure DNA origami and the triangular shaped DOS. The derived *E*-modulus agreed well with the AFM data for the sample integrities under different setoff forces. The pure DNA origami structures were heavily damaged under 1,600 pN. With larger forces up to 3,000 pN, the height signal was not stable and thus could not be used in the statistics. On the contrary, the DOS with 5 days of growth was almost intact even under 3,000 pN. The DOS with 1 day of growth was gradually destroyed as the force increased from 150 pN to 3,000 pN. The trends of normalized integrity were summarized in Supplementary Fig. 62-64.

The stability of the DNA nanostructures, both chemical and physical, plays an important role on its applications[37,38,40,41]. Previous studies showed that the chemical dam age from DNase, body fluids, and low salt environments can be prevented by using polymers and peptide modifications[37,38,42]. Also, the geometric information of DNA nanostructures can be easily lost during their interaction with various objects, especially after depositing onto hard surfaces, e.g. mica, silicon. Our DOS strategy provides a useful way to rigidify DNA structures for diverse transformative applications in nanofabrication.

7. Substrate-based DOS reaction

The amorphous silica shells prefer to aggregate by inter-particle dehydration reactions to form Si-O-Si bonds, rather than to form well-dispersed particles. Theoretically, it should be possible to separate these aggregated nanostructures with appropriate chemical modifications or by controlling the reaction rates. Nevertheless, it will take much effort to develop a robust solution-based mineralization method for DNA origami nanostructures. Indeed, substrate-based reactions will result in an incomplete coating on surfaces that are in contact with the substrate. We have already taken into consideration this incomplete coating in our mechanical calculations. For the planar structures, they will lose the contacting surface completely; for 3D frames and curved structures, they will also lose the contacting area depending on the angle of placement. However, the substrate-based DOS reaction will not restrict the potential application of the DOS structures. Currently, we have already pinpointed four different substrate supported mineralization materials (carbon film, silicon nitride-film, mica and silicon wafer), which could potentially have wide applications as we discussed in detail in the Outlook section.

Table. S1 Details of atomic simulation systems

System ID	DNA Structure	Solute	Cation	Anion
1	12 bp DNA[a]	TMAPS	-	-
2	12 bp DNA	TMAPS	Mg^{2+}	Cl^-
3	12 bp DNA	T_2 (dimer TMAPS)	Mg^{2+}	Cl^-
4	12 bp DNA	T_3 (trimer TMAPS)	Mg^{2+}	Cl^-
5	348 bp DNA origami	T_{32} (3 TMAPS+2 TEOS)	Mg^{2+}	Cl^-
6	198 bp DNA origami	T_3	Mg^{2+}	Cl^-
7	198 bp DNA origami	T_4 (tetramer TMAPS)	Mg^{2+}	Cl^-
8	198 bp DNA origami	T_5 (pentamer TMAPS)	Mg^{2+}	Cl^-
9	198 bp DNA origami	T_{32}	Mg^{2+}	Cl^-
10	198 bp DNA origami	T_{43}(4 TMAPS+3 TEOS)	Mg^{2+}	Cl^-
11	198 bp DNA origami	T_{54}(5 TMAPS+4 TEOS)	Mg^{2+}	Cl^-
12	198 bp DNA origami	T_{34}(3 TMAPS+4 TEOS)	Mg^{2+}	Cl^-
13	198 bp DNA origami	T_{36}(3 TMAPS+6 TEOS)	Mg^{2+}	Cl^-
14	198 bp DNA origami	T_{38}(3 TMAPS+8 TEOS)	Mg^{2+}	Cl^-
15	198 bp DNA origami	T_{23}(2 TMAPS+3 TEOS)	Mg^{2+}	Cl^-
16	198 bp DNA origami	T_{11}(1 TMAPS+1 TEOS)	Mg^{2+}	Cl^-

a. The 12 bp DNA is a crystal structure, pdb ID: 1bna

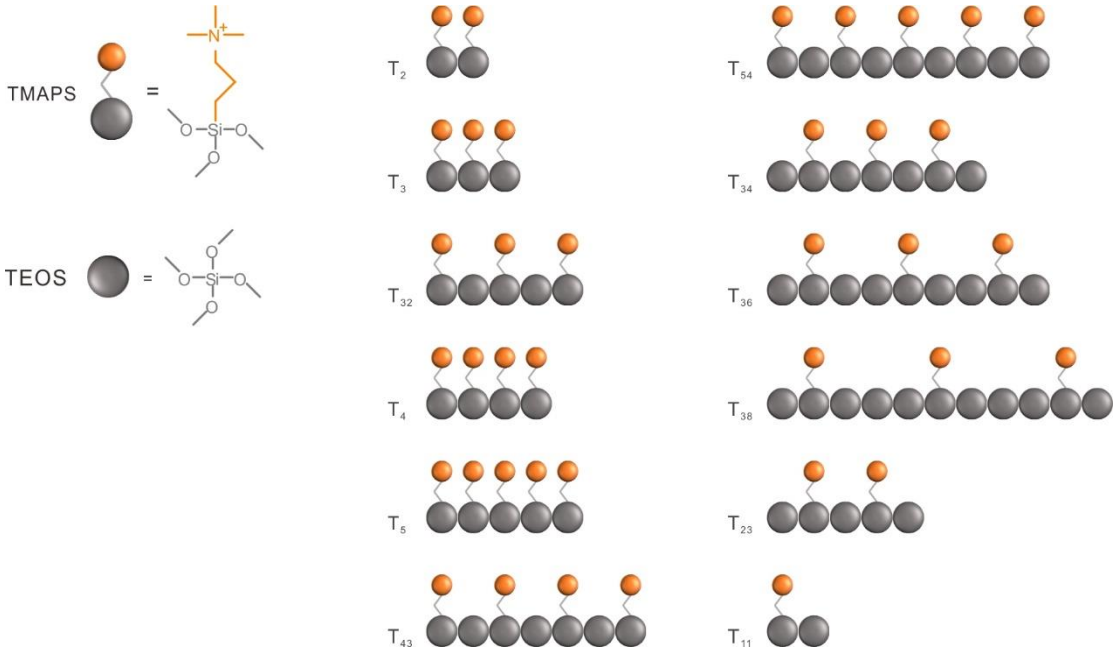

Table S2. Stoichiometric Ratio between TMAPS and TEOS.

TMAPS (v/v) (mM)	0.5% (9 mM)	1.0% (18 mM)	1.5% (27 mM)	2.0% (36 mM)	2.5% (45 mM)	3.0% (54 mM)	4.0% (72 mM)
TEOS (v/v) (mM)	0.5% (23 mM)	1.0% (45 mM)	1.5% (68 mM)	2.0% (90 mM)	2.5% (113 mM)	3.0% (135 mM)	4.0% (180 mM)

Table S3. DNA strand ratios, buffer conditions and annealing protocol for different DNA architectures

DNA architecture	triangle, rectangle, cross	6-helix	hemisphere, toroid, ellipsoid	tetrahedron -100 nm, cube	honeycomb	tetrahedron -15 nm	diatom
Ratios of DNA strands	Staples: scaffold = 10:1	Staples: scaffold = 10:1	Staples: scaffold = 10:1	Staples: scaffold = 10:1	Staples: scaffold = 10:1	L:M:S = 1:3:3	Staples: scaffold 1: scaffold 2 = 20:1:1
Synthetic buffer	40.0 mM Tris, 2.0 mM EDTA, 12.5 mM $MgAc_2$, PH = 8.0	40.0 mM Tris, 2.0 mM EDTA, 12.5 mM $MgAc_2$, PH = 8.0	40.0 mM Tris, 2.0 mM EDTA, 16.0 mM $MgCl_2$, PH = 8.0	40.0 mM Tris, 2.0 mM EDTA, 12.0 mM $MgCl_2$, PH = 8.0	40.0 mM Tris, 2.0 mM EDTA, 12.0 mM $MgCl_2$, PH = 8.0	40.0 mM Tris, 2.0 mM EDTA, 12.5 mM $MgAc_2$, PH = 8.0	40.0 mM Tris, 2.0 mM EDTA, 12.5 mM $MgAc_2$, PH = 8.0
Annealing protocol	2 h	12 h	12 h	48.h	72 h	48 h	12 h

Table S4: Frequencies and related vibrational modes of bands observed from the Raman spectra and standard bands.

Silicification Product (cm^{-1})	Standard (cm^{-1})[45, 46]	Vibrational Mode
466	487	Network defects
422	430	β(Si-O-Si)

* β, bending vibration.

Table S5: Frequencies and related vibrational modes of the bands observed from IR spectra and standard bands.

Silicification Product (cm^{-1})	Standard (cm^{-1})[45]	Vibrational Mode
3,732	3,650	*$Vs(O-H)_{(Si-O-H)}$
3,450	3,420	$Vs(O-H)_{(H_2O)}$
1,115	1,080	Vas(Si-O-Si)
966	960	V(Si-OH)
800	800	Vs(Si-O-Si)/ ring structures of SiO_2 tetrahedral
675	700	Vas(Si-C-C)
476	460	β(Si-O-Si)

* Vs, symmetric stretching vibration; Vas, asymmetric stretching vibration; V, stretching vibration; β, bending vibration.

Table S6. Structural parameters for different DOS shapes

Structural parameters used to describe the morphologies varied from structure to structure. The geometric data were directly measured from TEM images, *N* = 20.

	Theoretical Design (nm)					DOS nanostructures (nm)				
	Side	**Length**	**Width**	**Diameter**	**Height**	**Side**	**Length**	**Width**	**Diameter**	**Height**
Triangle	120.0	-	-	-	2.0	122.9 ± 4.1	-	-	-	4.3 ± 0.2
Rectangle	-	92.0	72.0	-	2.0	-	95.0 ± 1.2	70.0 ± 2.1	-	3.9 ± 0.3
Cross	-	95.0	35.0	-	4.0	-	83.2 ± 2.7	32.9 ± 1.7	-	5.5 ± 0.4
Diatom	55.0	-	-	-	4.0	55.1 ± 1.6	-	-	-	5.8 ± 0.4
6-helix	-	-	-	7.0	-	-	-	-	11.8 ± 1.1	-
Tetrahedron	100.0	-	-	11.0	81.6	106.2 ± 6.2	-	-	13.6 ± 1.0	55.9 ± 7.9
Cube	100.0	-	-	11.0	100.0	100.1 ± 5.2	-	-	15.1 ± 0.7	45.4 ± 4.5
Hemisphere	-	-	-	42.0	-	-	-	-	44.9 ± 1.2	-
Toroid	-	-	-	43.6	-	-	-	-	45.5 ± 2.3	-
Ellipsoid	-	-	-	35.0	-	-	-	-	38.1 ± 3.0	-

The data for the sides, lengths, widths and diameters were collected from TEM images (Fig. S19, and S32-42) that were taken of various DOS nanostructures while using ImageJ software. The height data was collected from AFM images using NanoScope Analysis 1.5 software. The size standard deviations were calculated using the following function:

$$S = \sqrt{\frac{\sum_{i=1}^{n}(X_i - \bar{X})^2}{n-1}}$$

Specifically, the terms of side, length, width and diameter for different structures were illustrated in the following scheme.

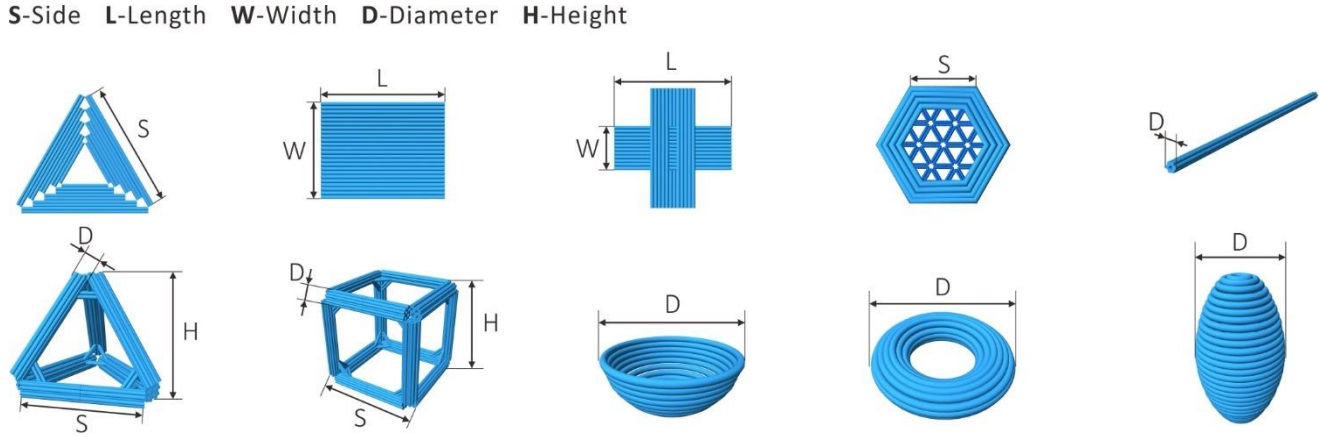

Table S7. Mechanical parameters of utilized materials

Material	Young's Modulus (GPa)	Poisson Ratio
Mica	62.0	0.21
Silicon	72.0	0.25
Amorphous silica[43]	70.0	0.18
DNA[44]	0.15	0.70

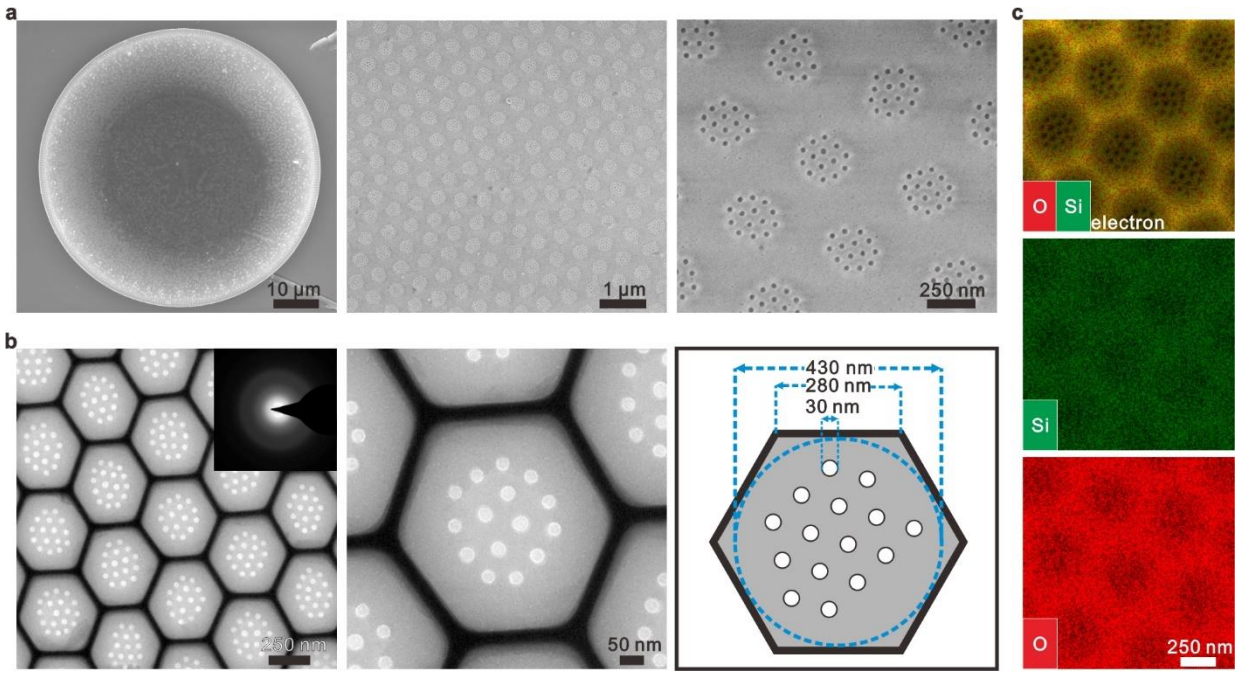

Figure 1 | The hierarchical honeycomb structures in the cell wall of a diatom (*Thalassiosira eccentrica*) shell. a and b. SEM and TEM images of a diatom shell's hierarchical honeycomb structures. The highly ordered honeycomb structures contain two types of pores, larger pores with 430 nm in diameter and smaller pores with 30 nm in diameter. **c.** Energy dispersive spectrometer (EDS) mapping confirmed the micro-area chemical composition of the corresponding sample. From top row to bottom row: EDS mapping overlapped with SEM image, Si and O mapping represented silica.

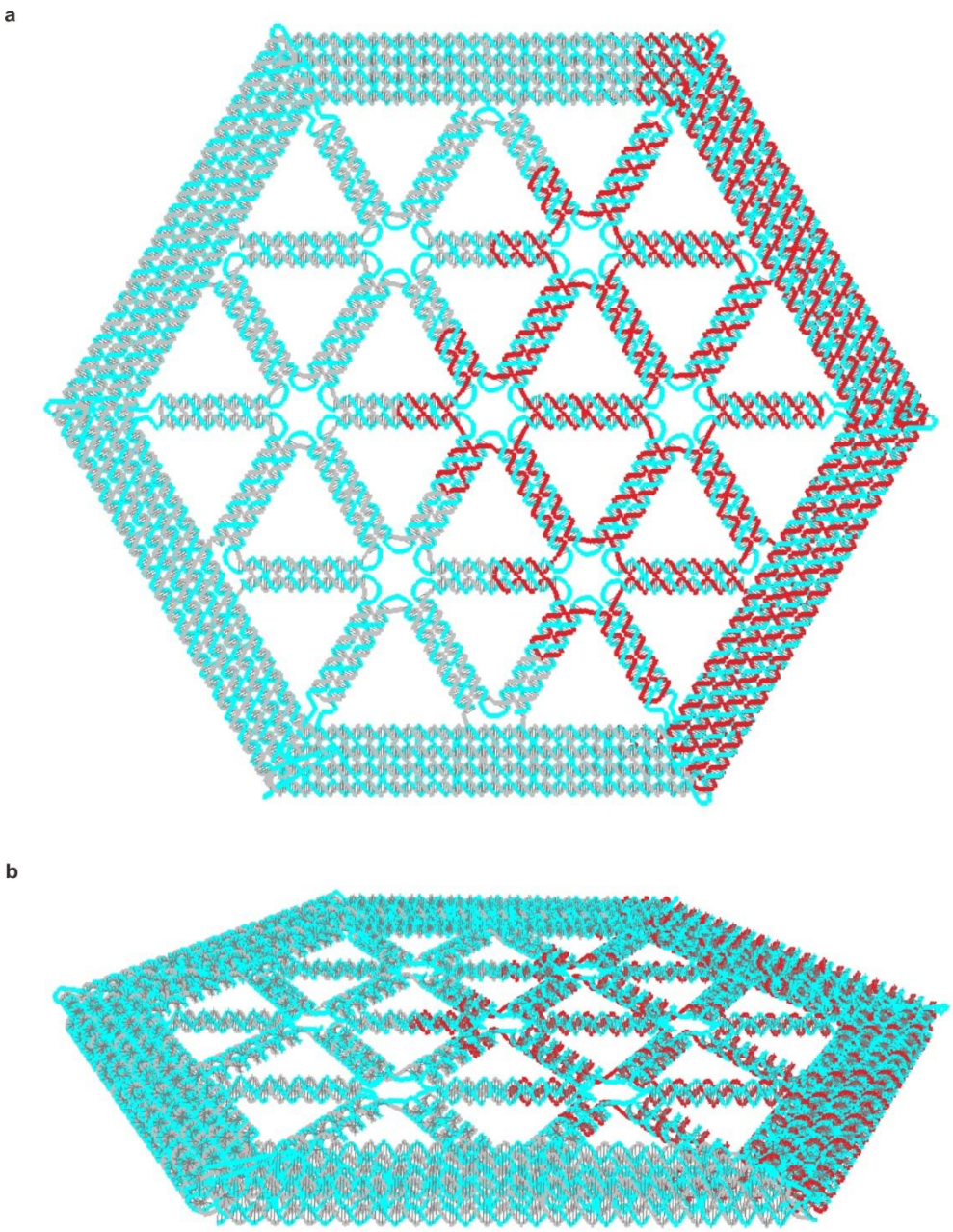

Figure 2 | Schematic diagram of the hierarchical pore structure. Scaffold strand 1 (M13mp18, 7,249 nt): gray. Scaffold strand 2 (phiX174 DNA, 5,386 nt): red. Staple strands: light blue.

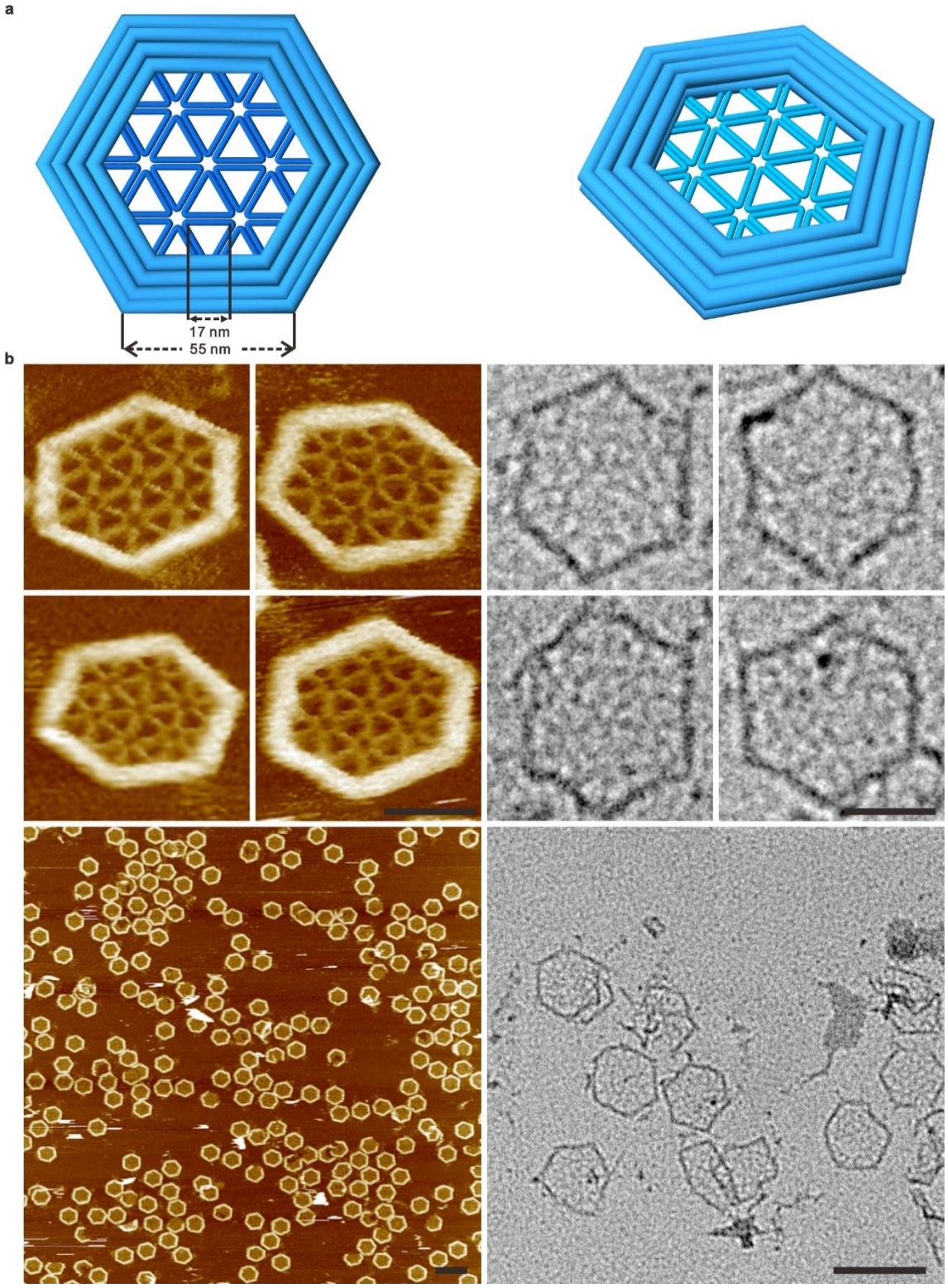

Figure 3 | Structural information and characterization of the Diatom mimicking DNA framework. a. The Diatom mimicking DNA framework was assembled with two scaffold strands, which had an average pore diameter of 82.4 nm, 9.8 nm, 5.4 nm, which was measured from the outside to the inside. **b.** Left column, AFM images. Right column, TEM images of negatively stained samples. Scale bars, zoomed in, 50 nm, and zoomed out, 200 nm.

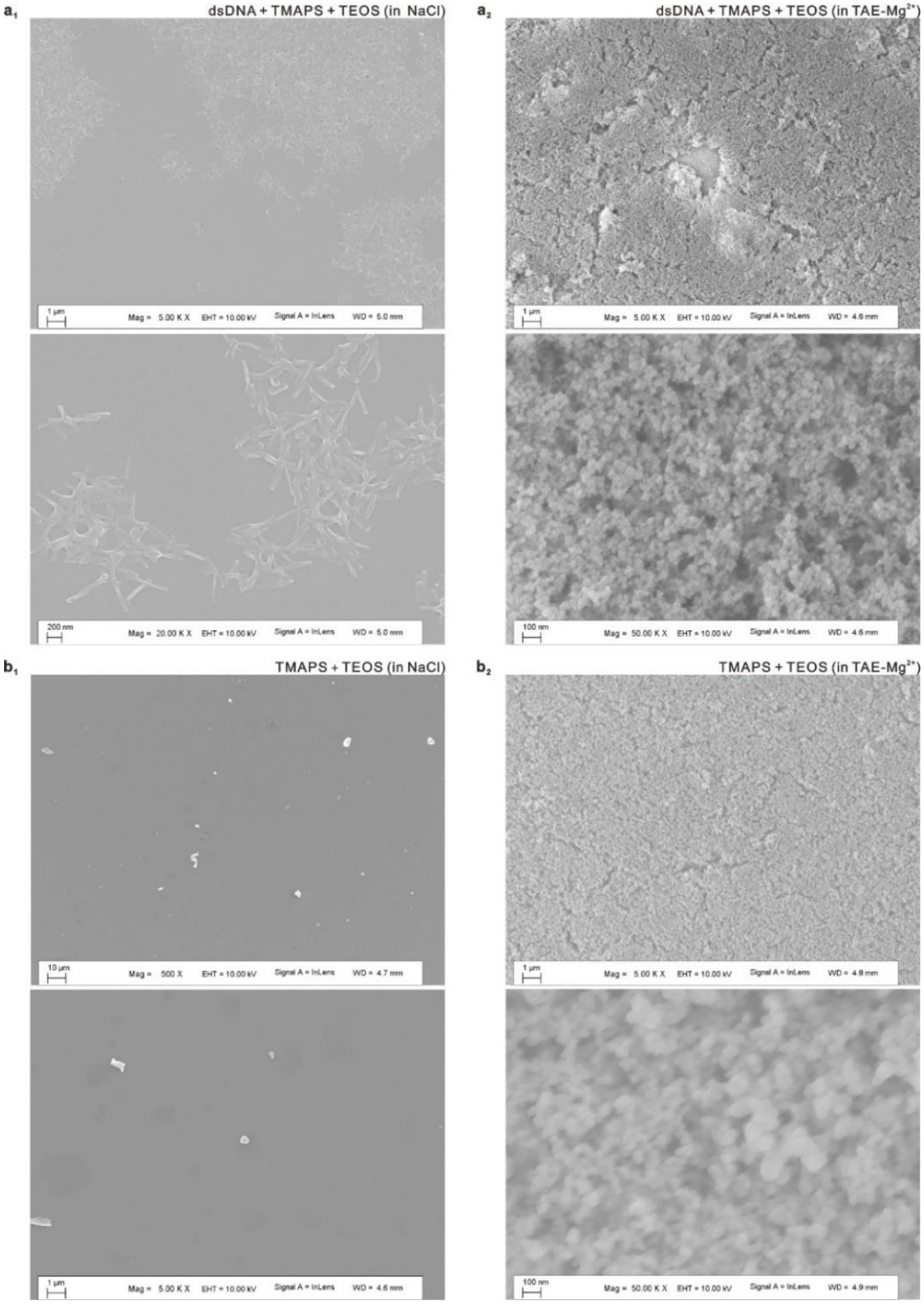

Figure 4 | Experimental verification of the DOS strategy on dsDNA (salmon testes, Sigma) system. a1. The molar ratio of dsDNA : Na^+ : TMAPS : TEOS : H_2O = 1 : 1 : 1.27 : 15 : 18,333, pH = 8.0 (Protocol copied from Chem. Comm. 2009, ref 13), and SEM results agreed with previous reports. **a2.** The molar ratio of dsDNA : Na^+ : TMAPS : TEOS : H_2O : Mg^{2+}= 1 : 1 : 1.27 : 15 : 18,333 : 4.2, in TAE-Mg^{2+} buffer (20 mM Tris, 2 mM EDTA, 12.5 mM Magnesium acetate), pH = 8.0. The other reaction conditions were the same and the structures were mineralized for 1 day. **b1** and **b2**, the dsDNA was removed from the solution in **a1** and **a2**. These results proved that for the dsDNA system, the co-structure directing agent hypothesis could not work in a high ion concentration buffer, such as TAE-Mg^{2+}, that is necessary for the folding of the DNA nanostructures.

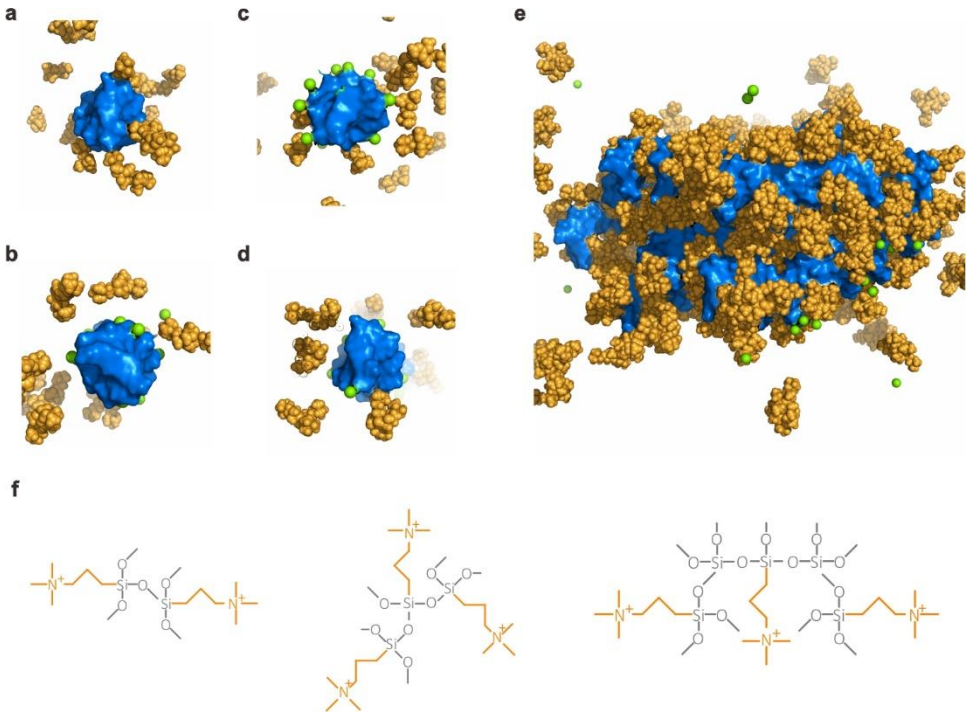

Figure 5 | Atomic MD simulation for the pre-hydrolyzing cluster mechanism. We investigated the interaction between the DNA and the TMAPS with five systems. **a.** Only the DNA and the TMAPS was studied in the first system. The TMAPS could condense onto the DNA surface in this system. **b.** In the second system, when we added Mg^{2+} ions with a concentration of 12.5 mM, the TMAPS was still suspended in the solvent. The interaction between the Mg^{2+} hydrate and the DNA is much stronger than the interaction between the mono TMAPS and the DNA. The possibility of the mono TMAPS condensing onto the DNA was low. To further investigate which kind of multimer can condense onto the DNA, we designed three kinds of multimers: T_2, T_3, and T_{32}. T_2 is a dimer, T_3 is a trimer, and T_{32} is a molecule that was hydrolyzed with three different TMAPS plus two TEOS molecules. (**Fig. S4f**). **c.** Although the total charge of the T_2 is equal to the charge of the Mg^{2+} hydrate, it still cannot condense onto the DNA. **d.** The T_3 system has one more charge than the Mg^{2+} hydrate. However, no condensation phenomenon occurred in this system. The lack of a condensation phenomenon may be attributed to the intramolecular tension, where the T_3 molecule was unable to bring two positive charges into adjacent positions, which ultimately weakened the interaction between the dsDNA and the T_3. **e.** When we added TEOS linkers between the TMAPS (T_{32}), a flexibility was given to the structure and allowed for the positive charge to be distributed into adjacent positions. This greatly increased the interactions between the DNA origami and the T_{32}. Therefore, the T_{32} molecules were able to condense onto the DNA origami, while some of the Mg^{2+} hydrate became detached and diffused into the solvent.

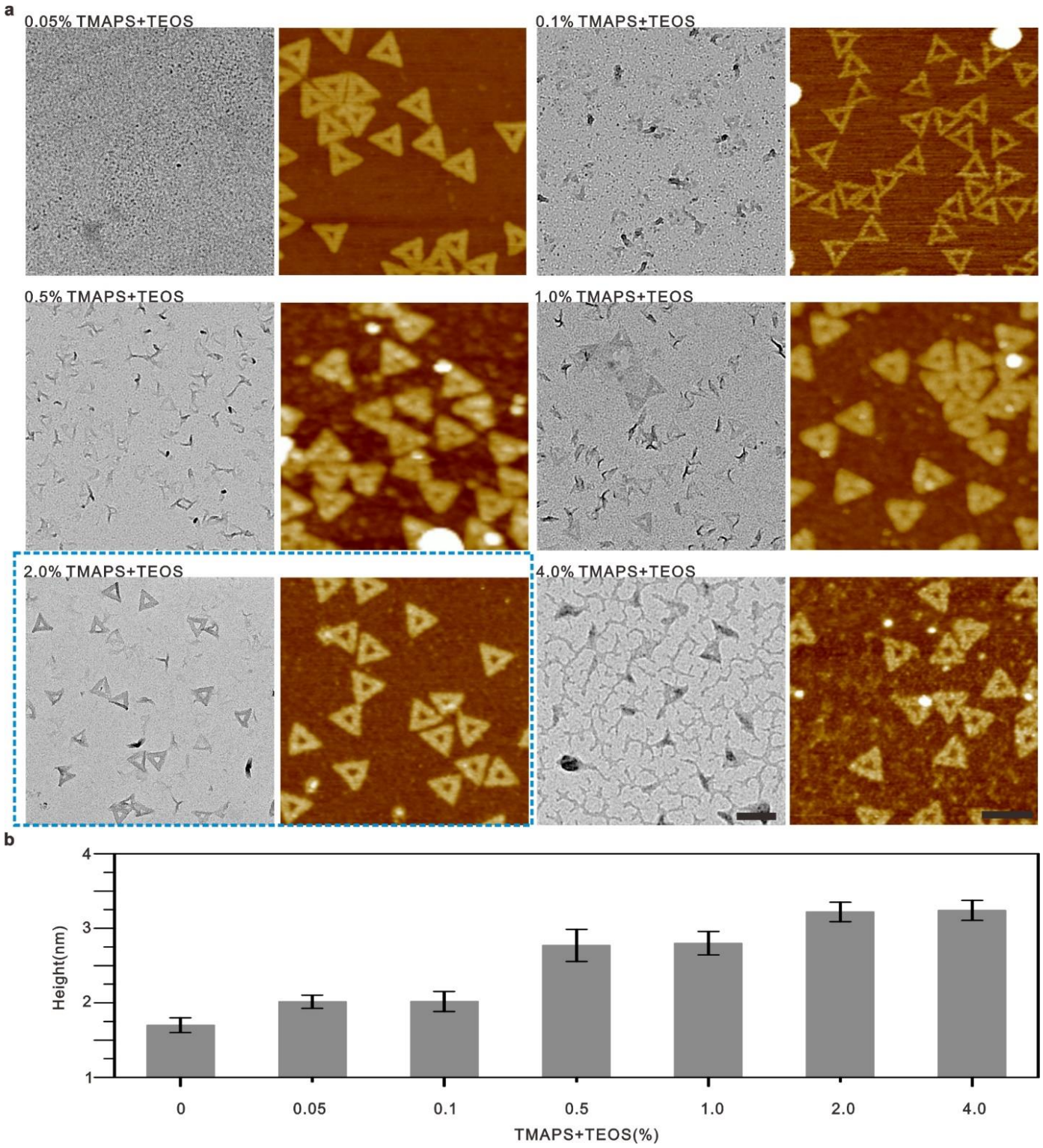

Figure 6 | The influence of TMAPS+TEOS concentrations (v/v) on DOS triangle. a. TEM and AFM images of silicification reaction results using different TMAPS+TEOS concentrations. **b**. Height statistics of triangle DOS structures (N = 20). TMAPS: TEOS = 1:1 (v/v) = 2:5 (mol/mol), reaction time was 24 h. We found that 2.0% TMAPS+TEOS was the best concentration from the TEM images and height changes. 4.0% TMAPS+TEOS produced impurities on the surfaces when silica was grown on the DNA. Scale bars, 200 nm.

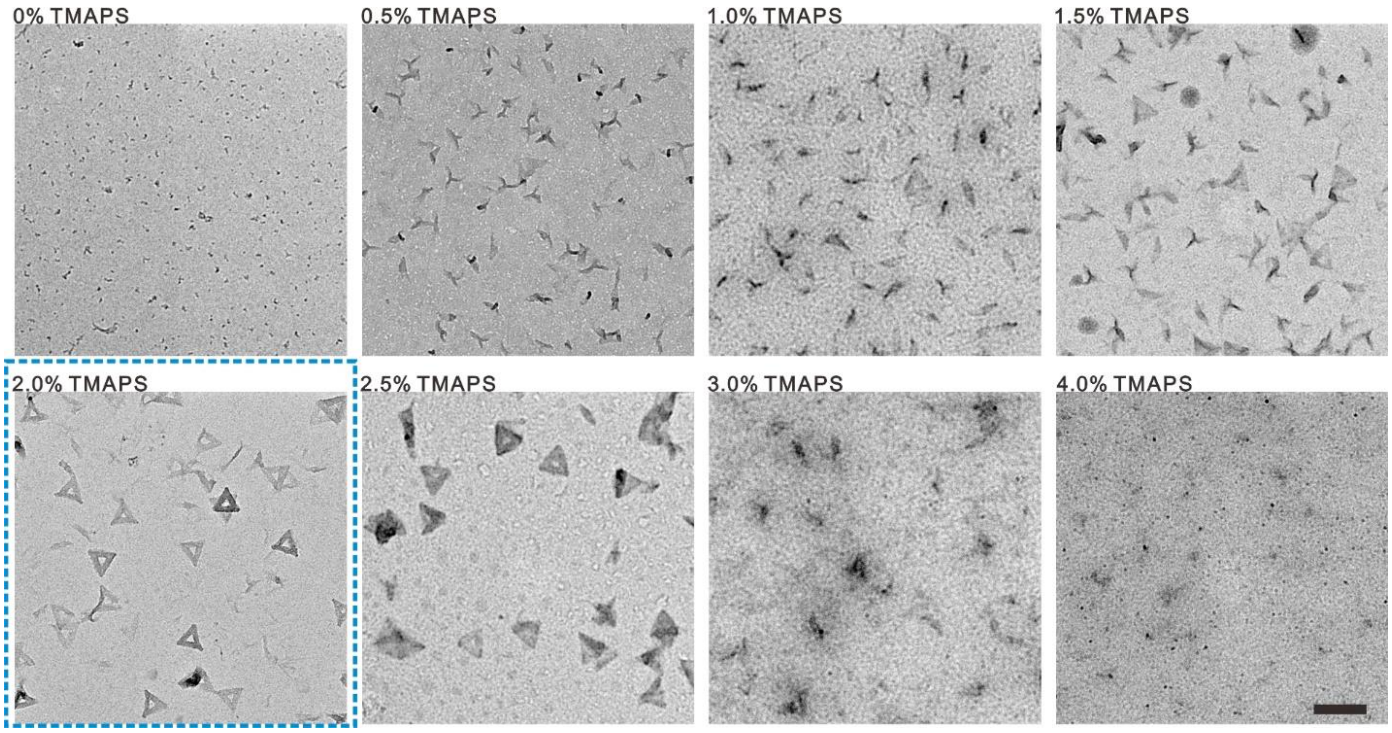

Figure 7 | The influence of TMAPS concentrations and ratios between TMAPS and TEOS (TEOS was 2.0%) on DOS triangle. Reaction time was 24 h. Lower than 2.0% or higher than 2.5% TMAPS induced incomplete reactions. The reason for the former situation was that the lower concentration could not compete with the Mg^{2+}, which then induced an incomplete reaction between the TMAPS and DNA. The reason for the latter situation arose possibly because of excess free TMAPS provided free nucleation sites in the solution. Scale bars, 200 nm.

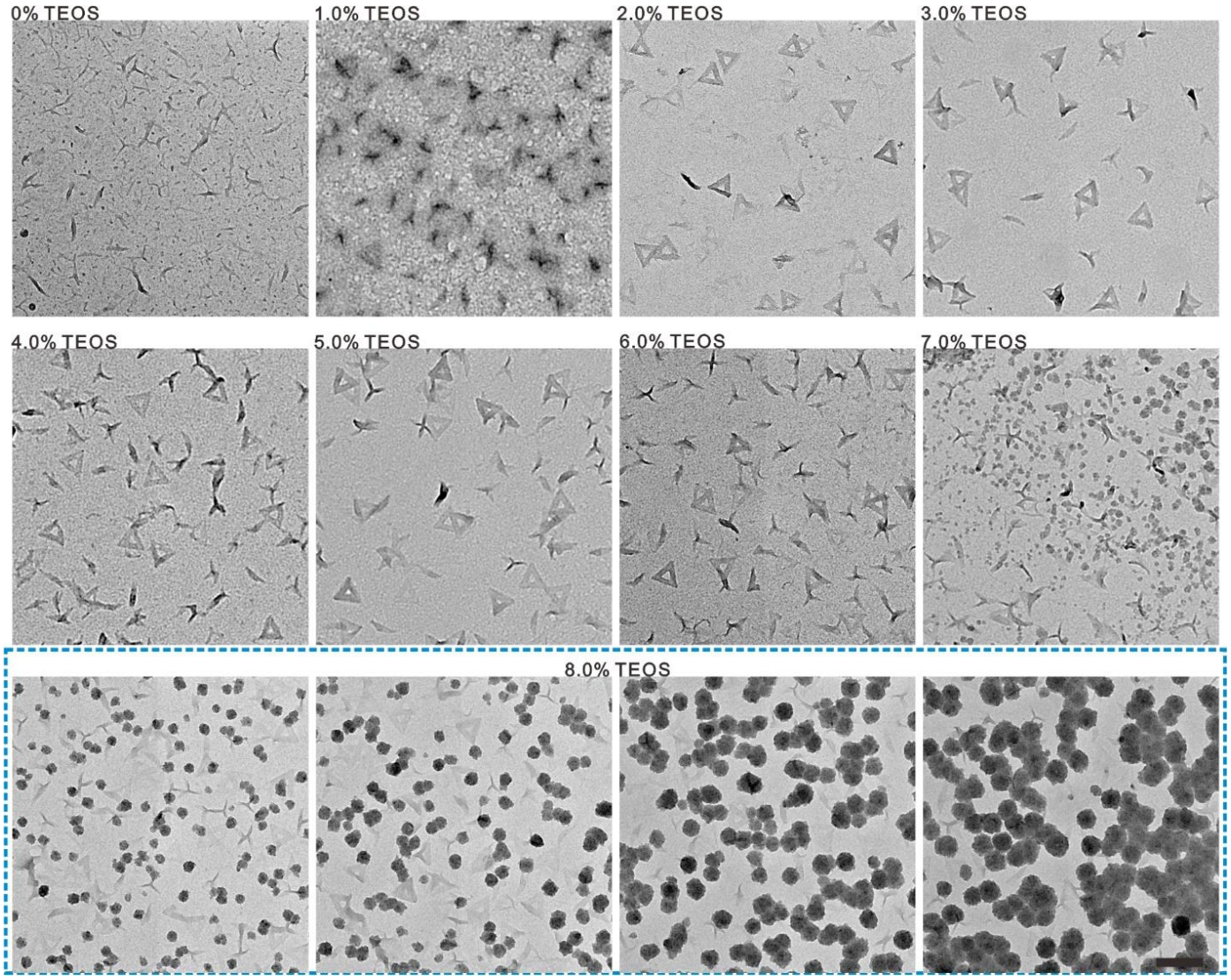

Figure 8 | The influence of TEOS concentrations (TMAPS was 2.0%) on DOS triangle. Reaction time was 24 h. As the concentration of the TEOS increased, the DOS was more and more obvious before a 2.0% TEOS concentration was achieved. Then, the DOS did not change much between a 2.0% and 6.0% concentration of TEOS. Different sized spherical silica (no more than 100 nm) were produced after a 7.0% TEOS concentration due to self-aggregation of the TMAPS molecules and the heterogeneous silicification. Scale bars, 200 nm.

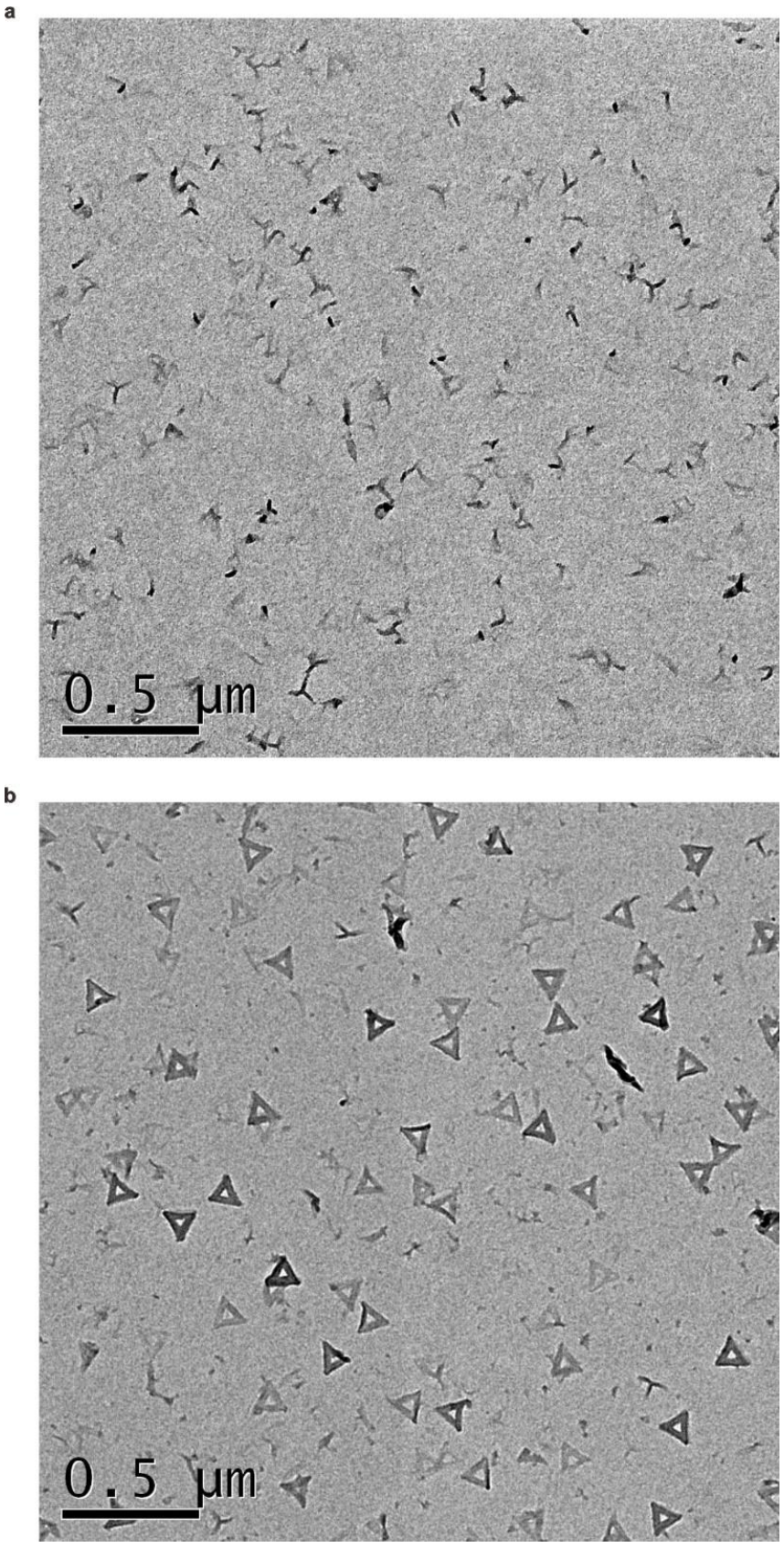

Figure 9 | Experimental verification of the DOS strategy on a DNA origami system. TEM images for the silicification of the triangular DNA origami after 1 day without (**a**) or with (**b**) the prehydrolyzing process. The composition and concentration of all of the chemicals were adopted from the optimized conditions of our current work. Group **a** simply copied the co-structure directing agent procedure described in **ref. 22**, while group **b** followed our DOS strategy. These results proved that for a DNA origami system, the co-structure directing agent hypothesis could not work.

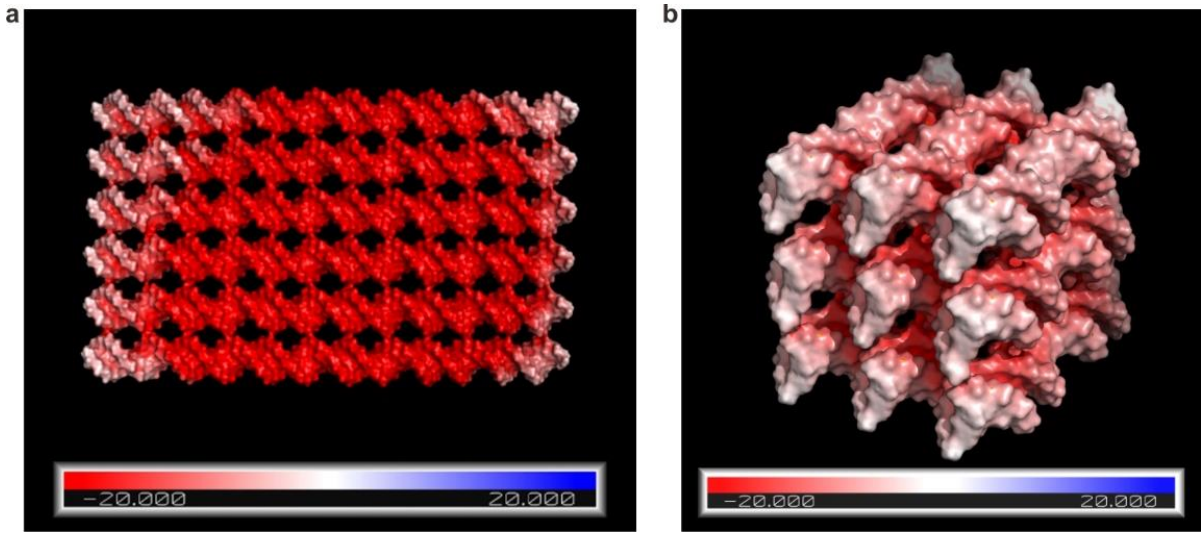

Figure 10 | The Adaptive Poisson-Boltzmann Solver (APBS) mapping of the electrostatics on the DNA origami model we used for MD simulation. The simulation result revealed a uniformly negatively charged surface for both 2D and 3D (**a** and **b**) DNA origami fragments.

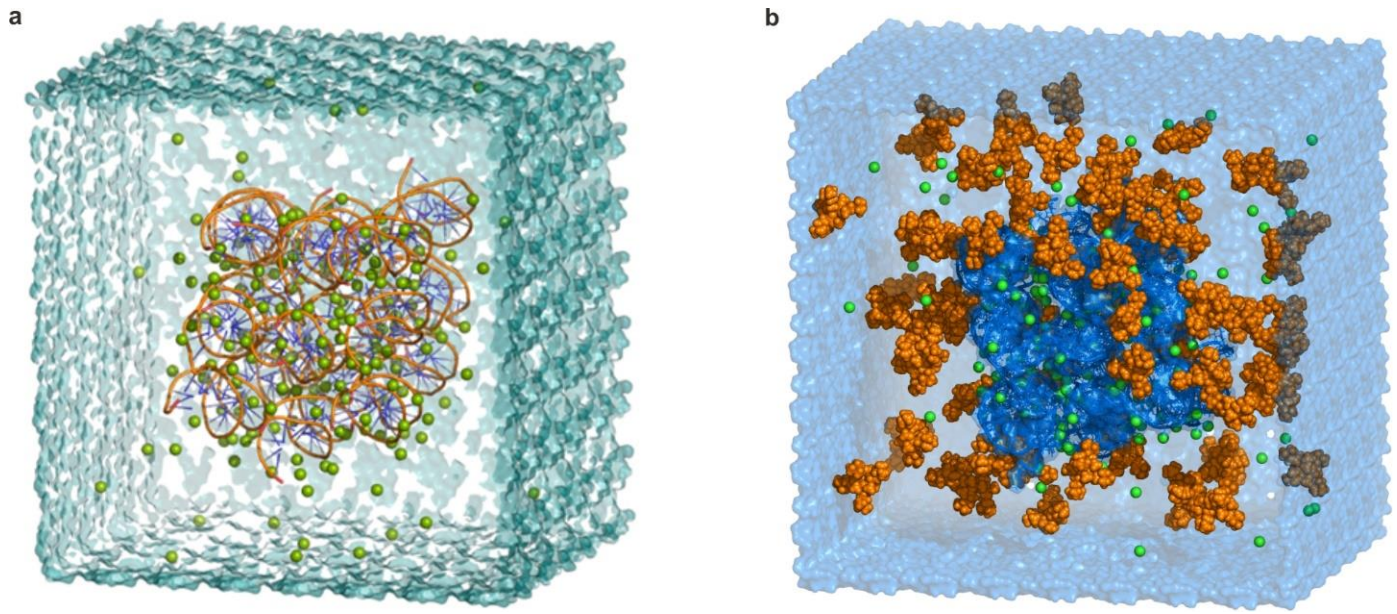

Figure 11 | Set up of coarse grained DOS MD simulation. a. A 50 ns MD simulation was performed on the DNA origami 9 helix bundle (9B) with 190 Mg^{2+} as counter ions that created a pre-equilibrated 9B and Mg^{2+} system. Then 11 different T_{ab} clusters with a total of 300 positive charges (The number of TMPAS, TEOS and Mg^{2+} were approximations as best we can make out regarding what is going on in the optimized experimental condition) were inserted into the pre-equilibrated system to build 11 DOS simulation systems respectively. First, all 11 systems were minimized with 2,000 steps during the steepest descent and 2,000 steps during the conjugate gradient minimization. Then the systems were heated to 300 K and a 5 ns NPT equilibration was performed. Finally, 50 ns NVT production MD simulations were performed to evaluate the tendency of 11 T_{ab} clusters to condense together. **b.** Take the T_4 cluster for example. After a 55 ns MD simulation, we checked the central section of the 9B. We found that the ligands were condensed on the surface of the 9B and between the outer helix of the 9B. In the center of the 9B, we found hydrated Mg^{2+} ions that were bound to 9B so tightly, that T_{ab} clusters were not able to move in. This phenomenon supported the experimental results that the coating of silica only happens on DNA origami surface. Note that the reported gap between two adjacent dsDNA is about 5 ~ 10 Å in DNA origami structures, and T_{ab} clusters with a theoretical diameter of ~ 30 Å could barely insert into the spaces between two dsDNA helices, resulting in a continuous organic DNA core wrapped in an amorphous silica shell (Fig. 1b)[2-6]. This also contributes to the ability of our method to preserve the structural information of the DNA nanostructure templates with minimal shape changing.

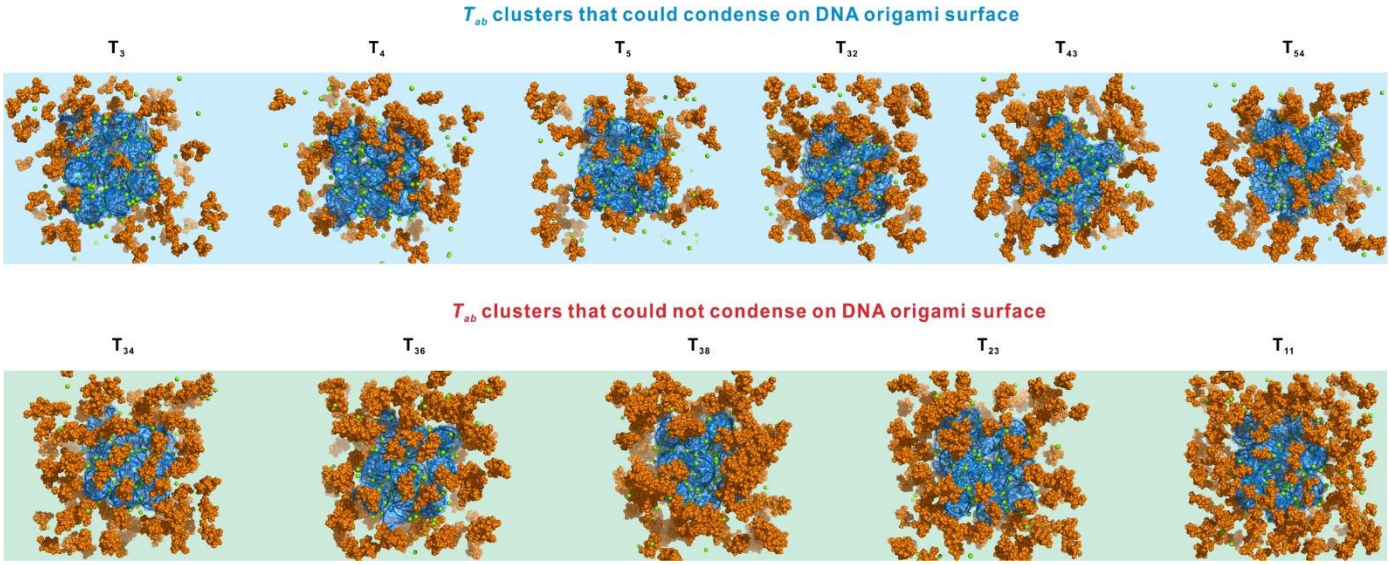

Figure 12 | Visual inspection of the DOS T_{ab} cluster systems. At first glance, these two sets of T_{ab} cluster systems reveal that for the DNA nanostructures did not induce attachments (Lower row), the T_{ab} clusters tended to diffuse into the bulk solution. Furthermore, we counted the number of N^+ atoms within an 8 Å range of the DNA origami fragment. As shown in Fig. 1c, the red dashed line showed the average number of N^+ atom that did not affect the 9B (N^+ atom density of the whole system multiplied by the space volume of 8 Å around the 9B sides). In systems with histogram above red dash line, the ligands condensed on 9B by replacing part of hydrate Mg^{2+} ions. In system with histogram below red dash line, the ligands cannot replace adequate hydrate Mg^{2+} ions to condense on 9B sides.

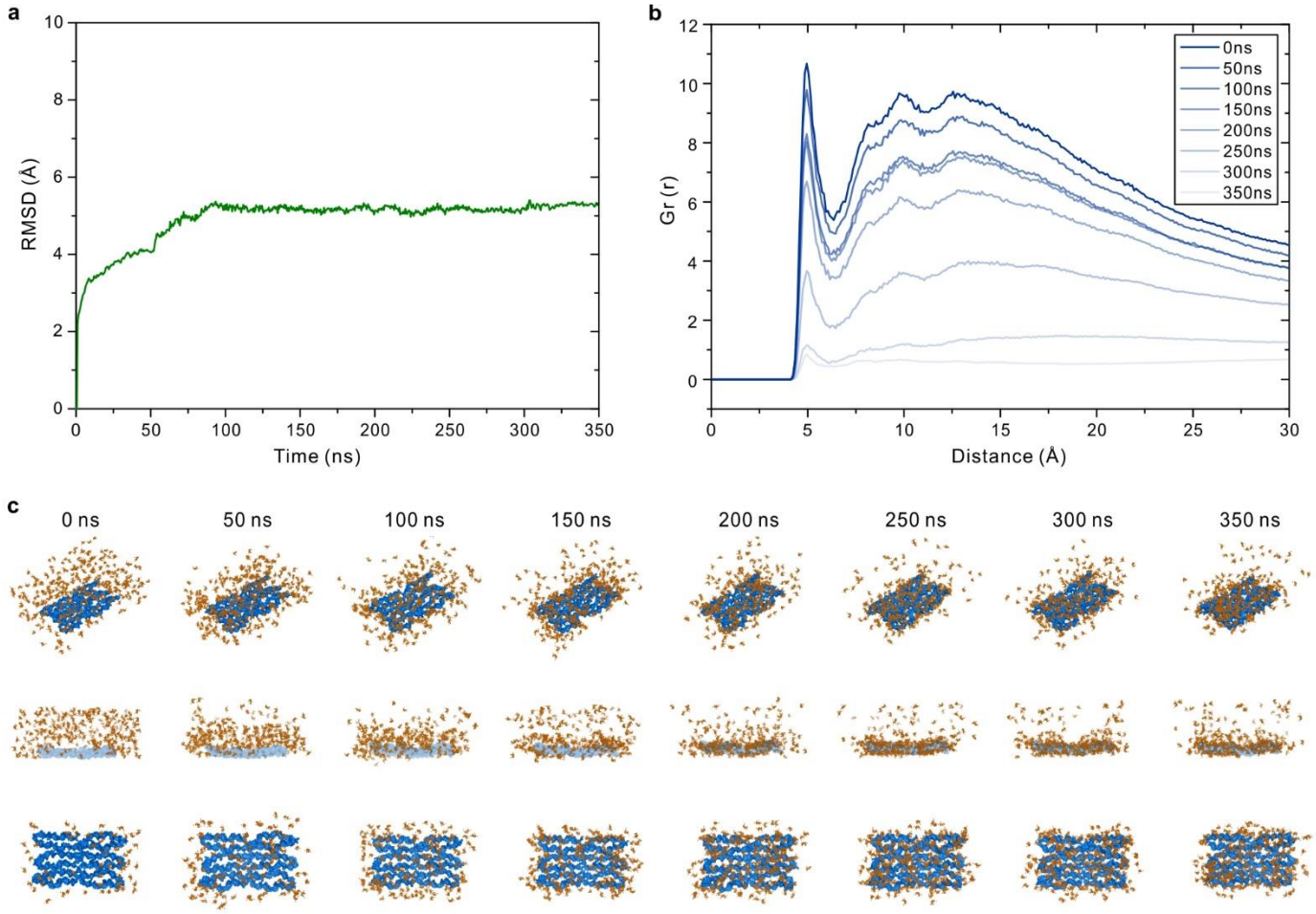

Figure 13 | Coarse grained MD simulation for the condensation process of DOS. A 350 ns MD simulation was performed to investigate the condensation of T_{32} clusters onto a 348 bp single layer DNA origami. **a.** The root mean square deviation (RMSD) result revealed that the DNA origami was not quite stable when the T_{32} molecules were mainly free in the solvent at beginning of the experiment. However, after 100 ns, the T_{32} clusters began to accumulate on the origami and the concentration of the T_{32} clusters near the DNA origami was four times greater than the average of the whole simulation system. As the system became stable, the RMSD reached a balance. **b.** The final concentration at 350 ns, of the T_{32} clusters near the DNA origami, was about 10 times greater than the average of the whole system. **c.** Snap shots of the system from different viewing angles. Note that from the side and top views, the T_{32} clusters were infrequently inserted into the gap regions of the DNA helixes.

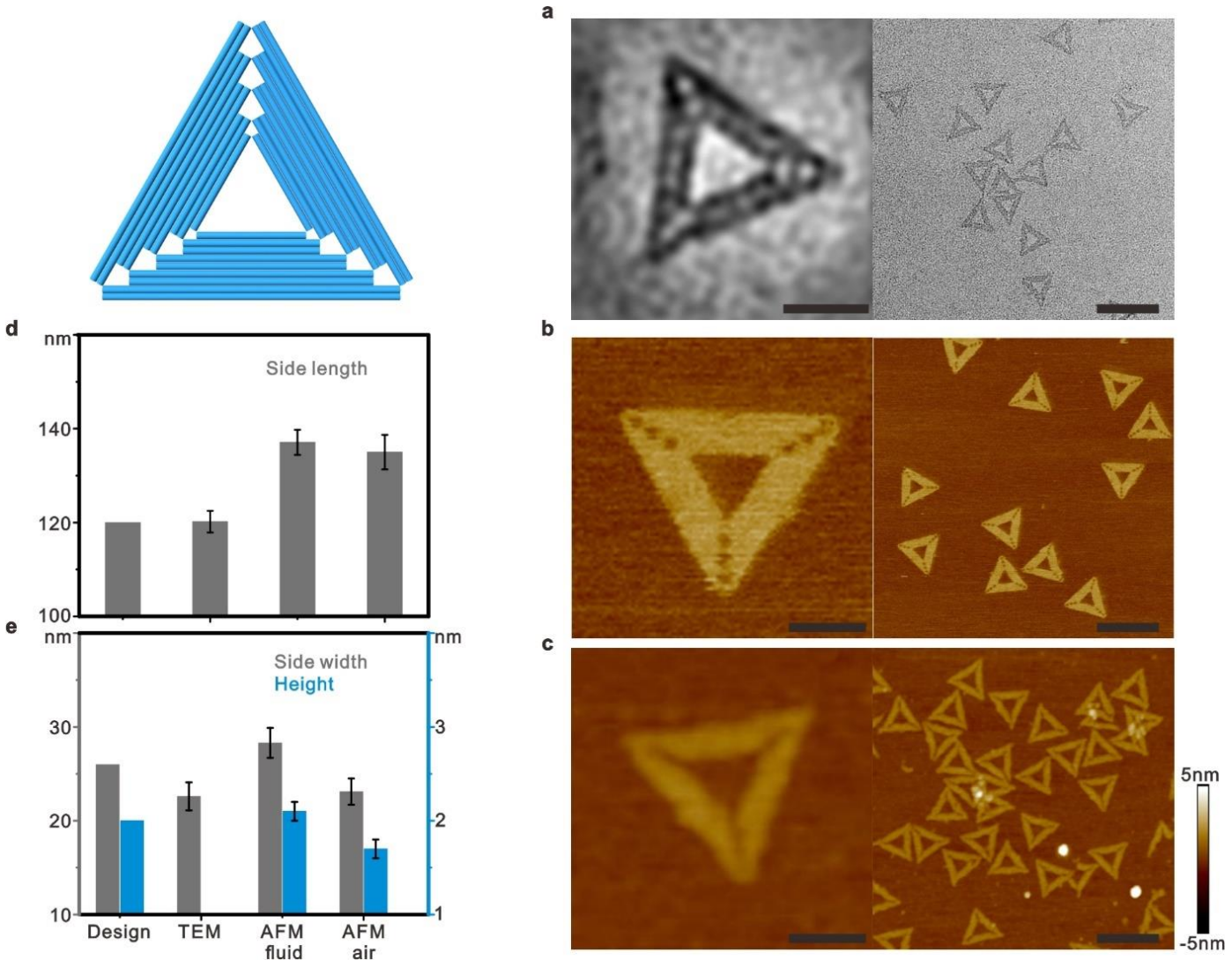

Figure 14 | Geometric characterization of triangle DNA origami. a. TEM images of negatively stained samples. **b.** AFM images acquired by Peakforce-in-fluid mode. **c.** AFM images acquired by Peakforce-in-air mode. **d and e.** Considering the broadening effect of the AFM, it is more appropriate to measure the geometric information on the x-y plane with TEM. In comparison to the designed geometries (26.0 nm edge width calculated with a 1.0 nm interhelical domain gap and a 2.0 nm double helix DNA) [2], the DNA sample showed a 3.4 nm shrinkage under TEM. A similar result from AFM in air mode may have come from the combination of the broadening effect and a dehydration-induced shrinkage. Scale bars, zoomed in, 50 nm, and zoomed out, 200 nm.

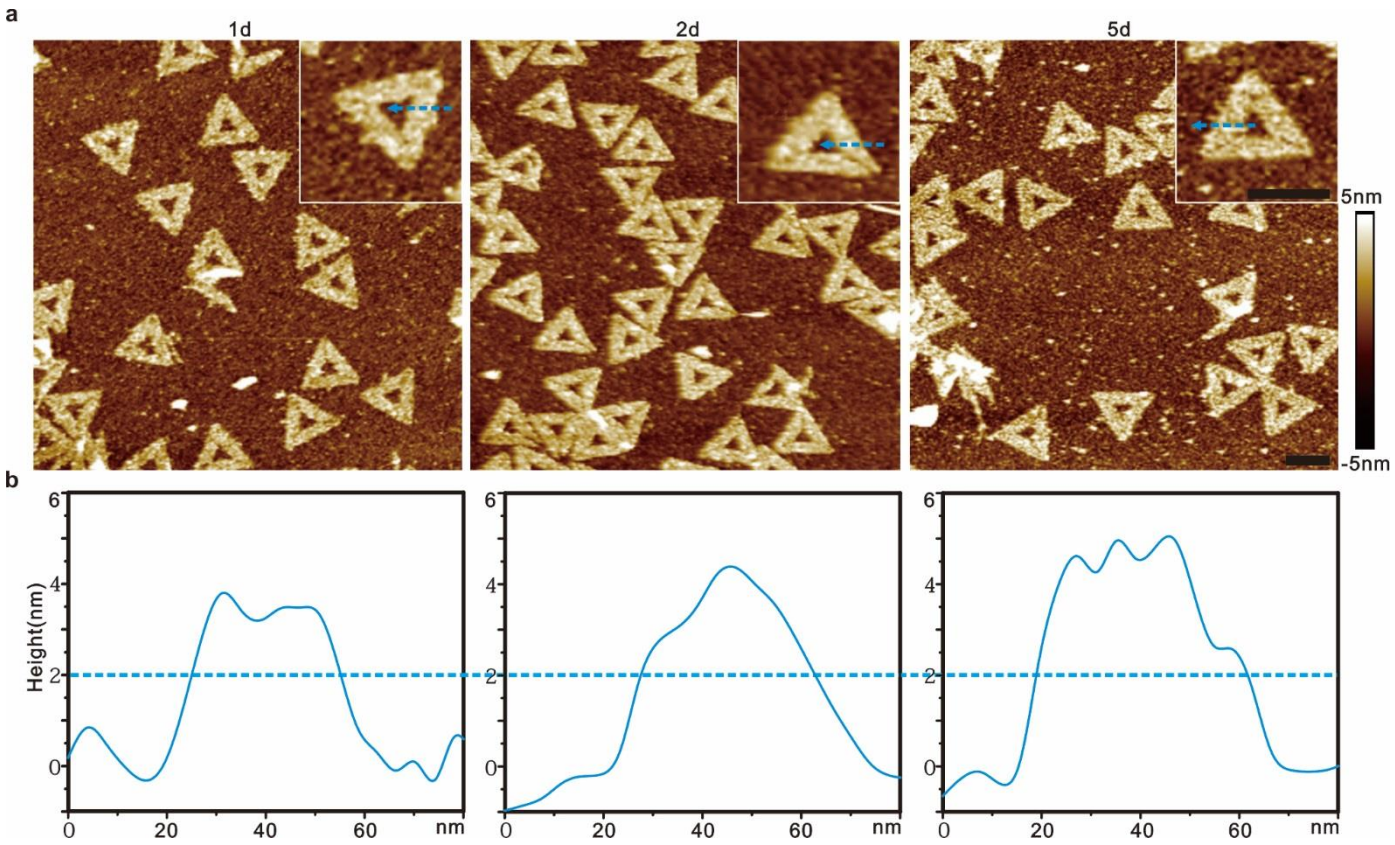

Figure 15 | AFM images of DOS triangle and corresponding height diagrams at different silicification periods, a and **b.** The blue line represents the height of the triangle DNA origami. The corresponding statistical data were shown in Fig. 2a. Scale bars, 100 nm.

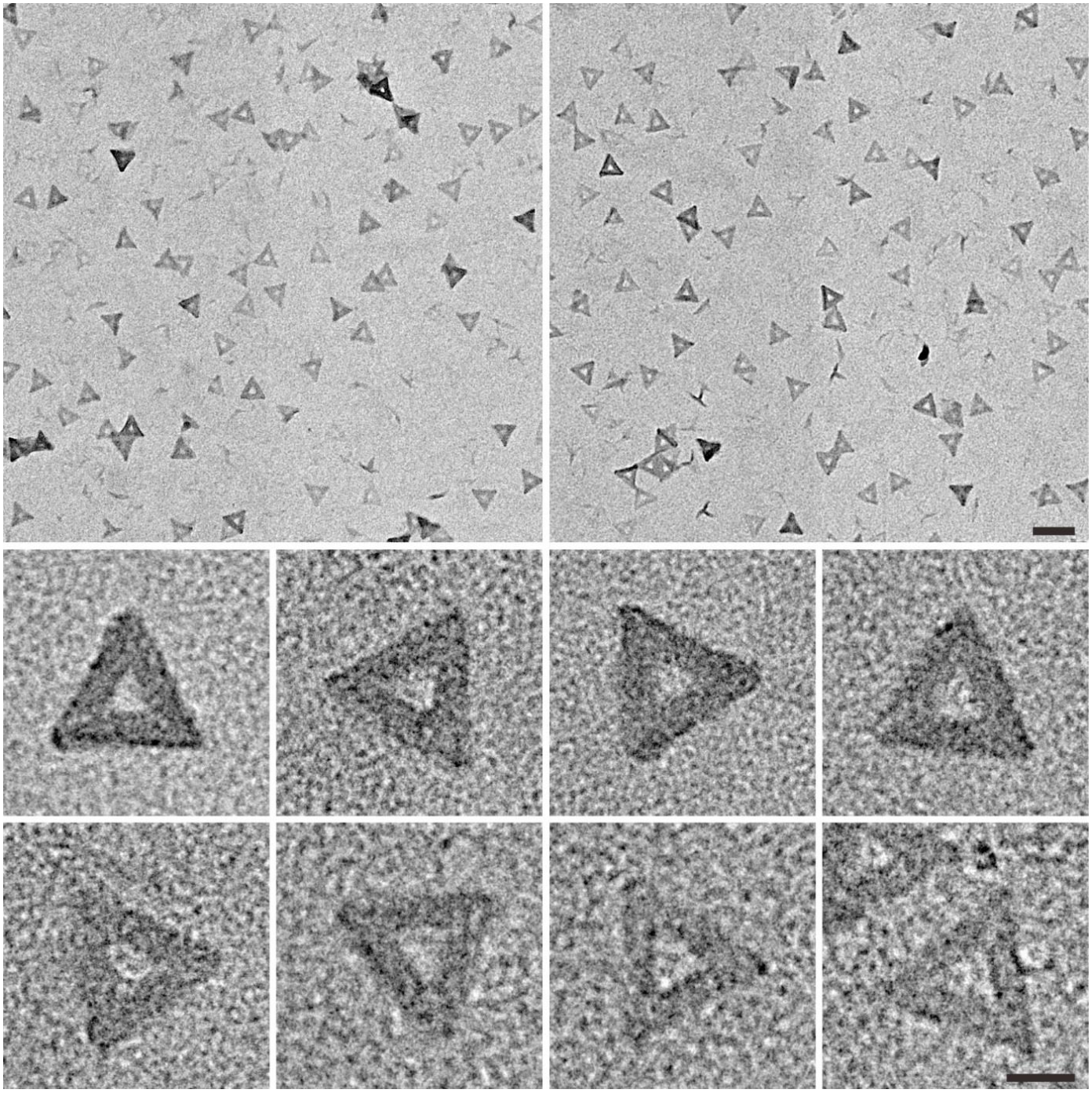

Figure 16 | TEM images, zoomed out/in of DOS triangle that was reacted for 1 day. Scale bars, zoomed in, 50 nm, and zoomed out, 200 nm.

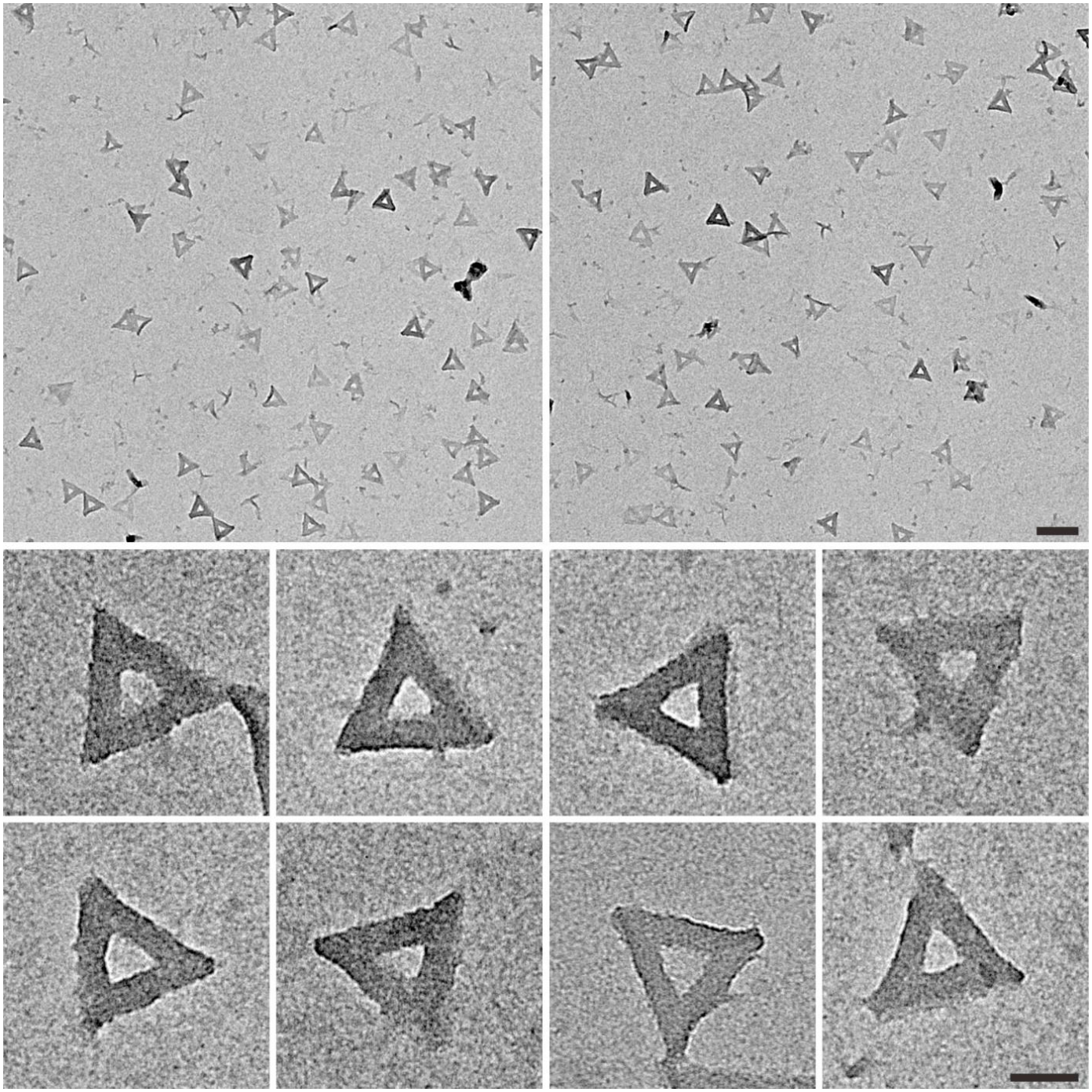

Figure 17 | TEM images, zoomed out/in of DOS triangle that was reacted for 2 days. Scale bars, zoomed in, 50 nm, and zoomed out, 200 nm.

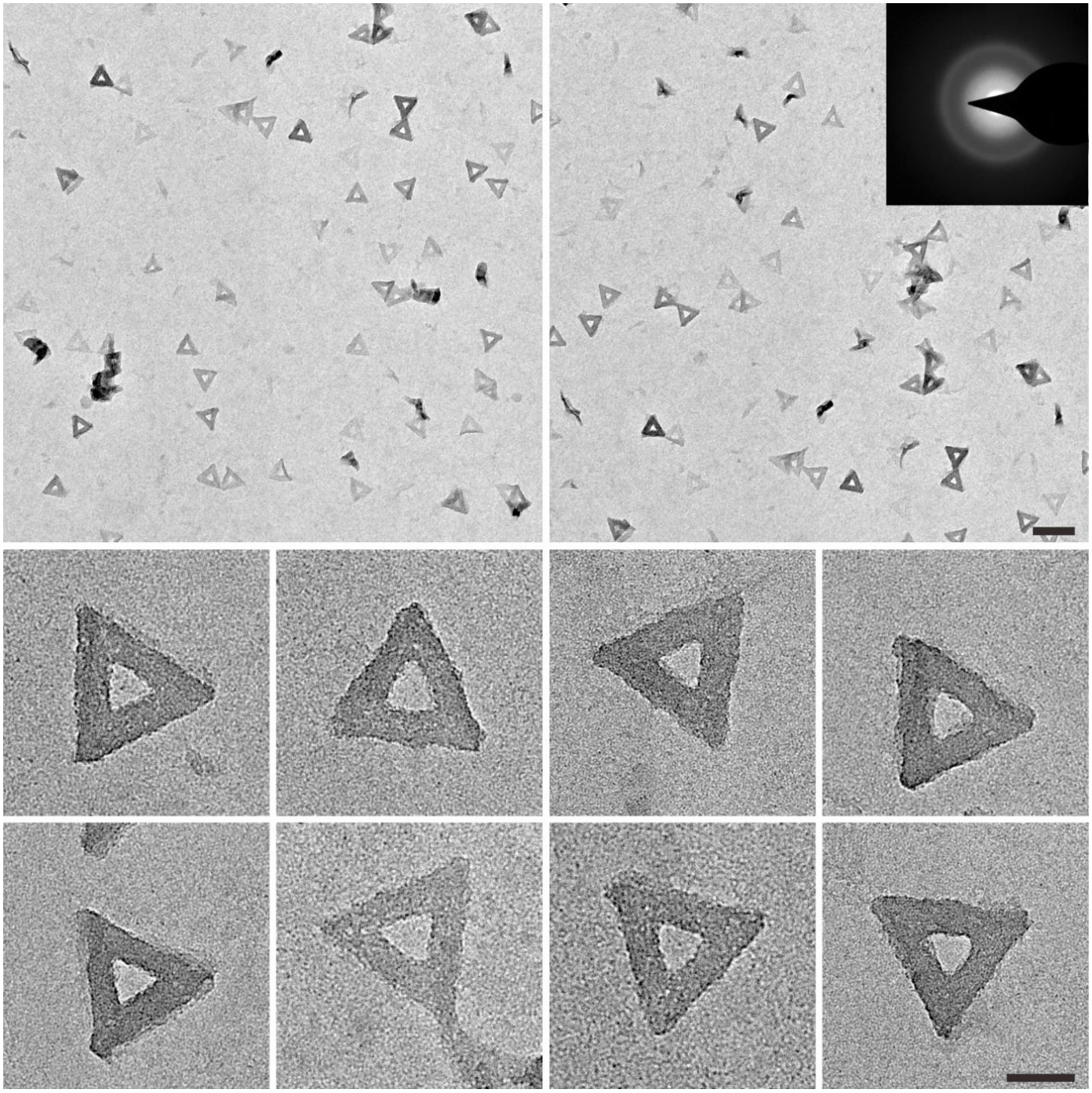

Figure 18 | TEM images, zoomed out/in of DOS triangle that was reacted for 5 days. Selected area electron scattering (SAED) revealed the amorphous features of the silica in the DOS structure. Scale bars, zoomed in, 50 nm, and zoomed out, 200 nm.

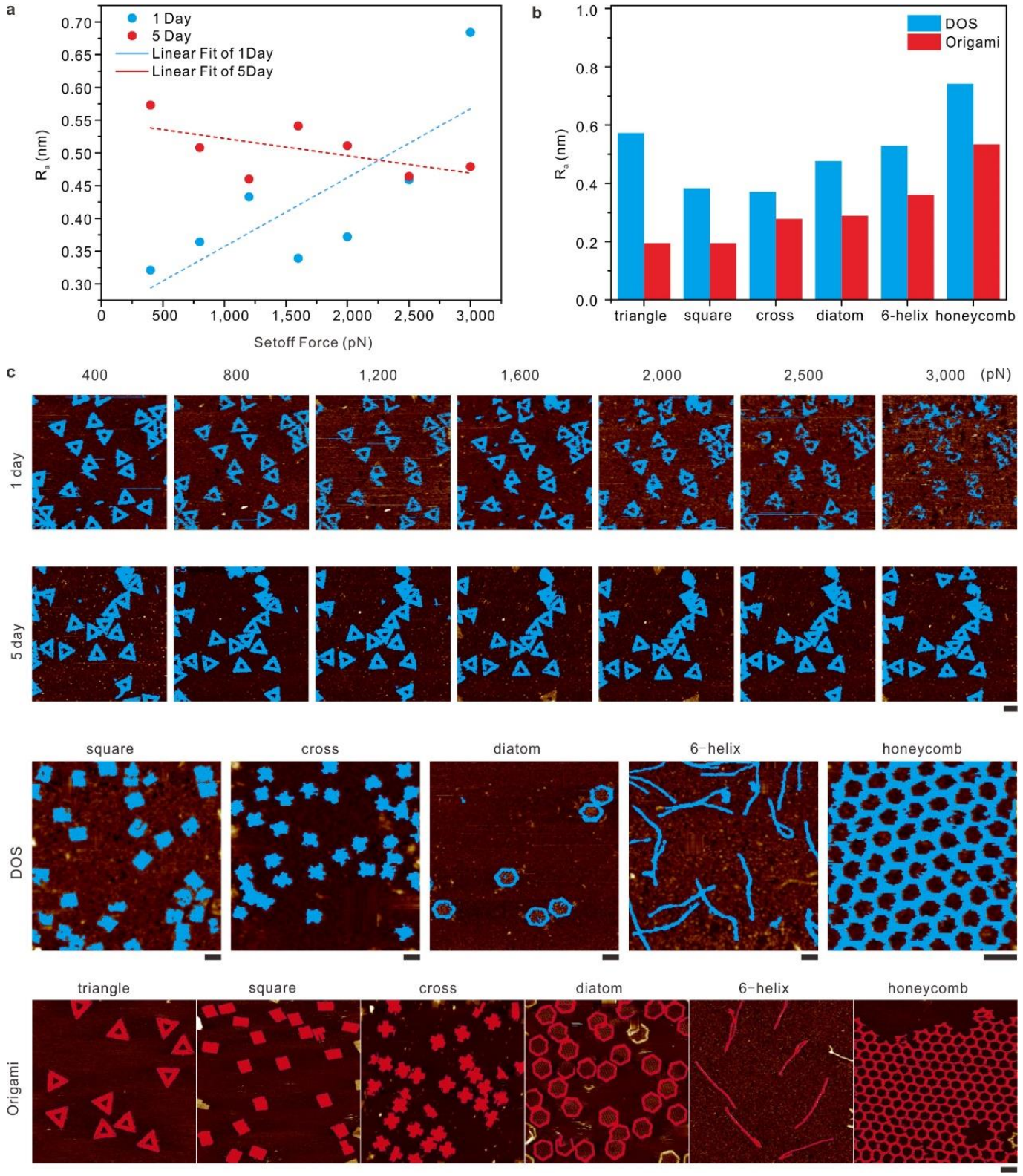

Figure 19 | Surface roughness (As evaluated by the arithmetic average of the absolute values, R_a) of typical 2D DOS structures. a. A graph of the time and setoff force dependent R_a value of a DOS triangle. For the 1 Day sample, the R_a values were positively correlated to the setoff forces, because the DOS triangle was partially damaged under higher forces. For the 5 Day sample, the R_a values were negatively correlated to the setoff forces. The R_a value varied from ~ 0.3 nm to ~ 0.7 nm. **b.** The R_a values of typical 2D DOS structures were collected at 200 ~ 400 pN. Because the images were not taken with a single tip, the data sets showed semi-quantitative results. The R_a values varied in the range from ~ 0.4 nm to ~ 0.7 nm, which indicated that the roughness corresponded with the one- or two-layer difference in the silica tetrahedron since the bond length of Si - O is 166 pm. **c.** Corresponding selected data area for roughness statistics. Scale bars, 100 nm.

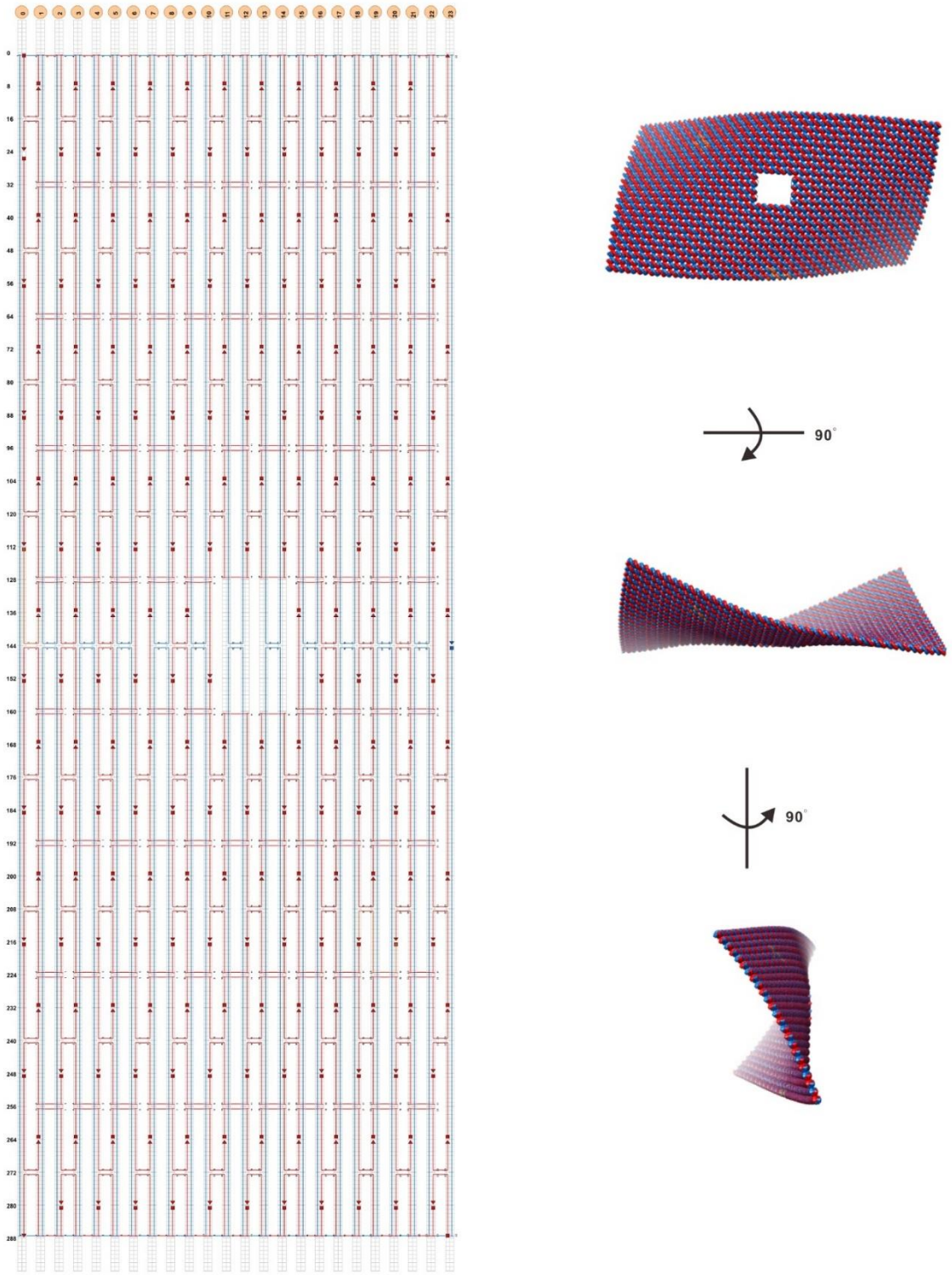

Figure 20 | Figure S16. Strand diagrams and predicted shapes of a theoretical rectangular structure with a 13 nm × 11 nm nanopore.

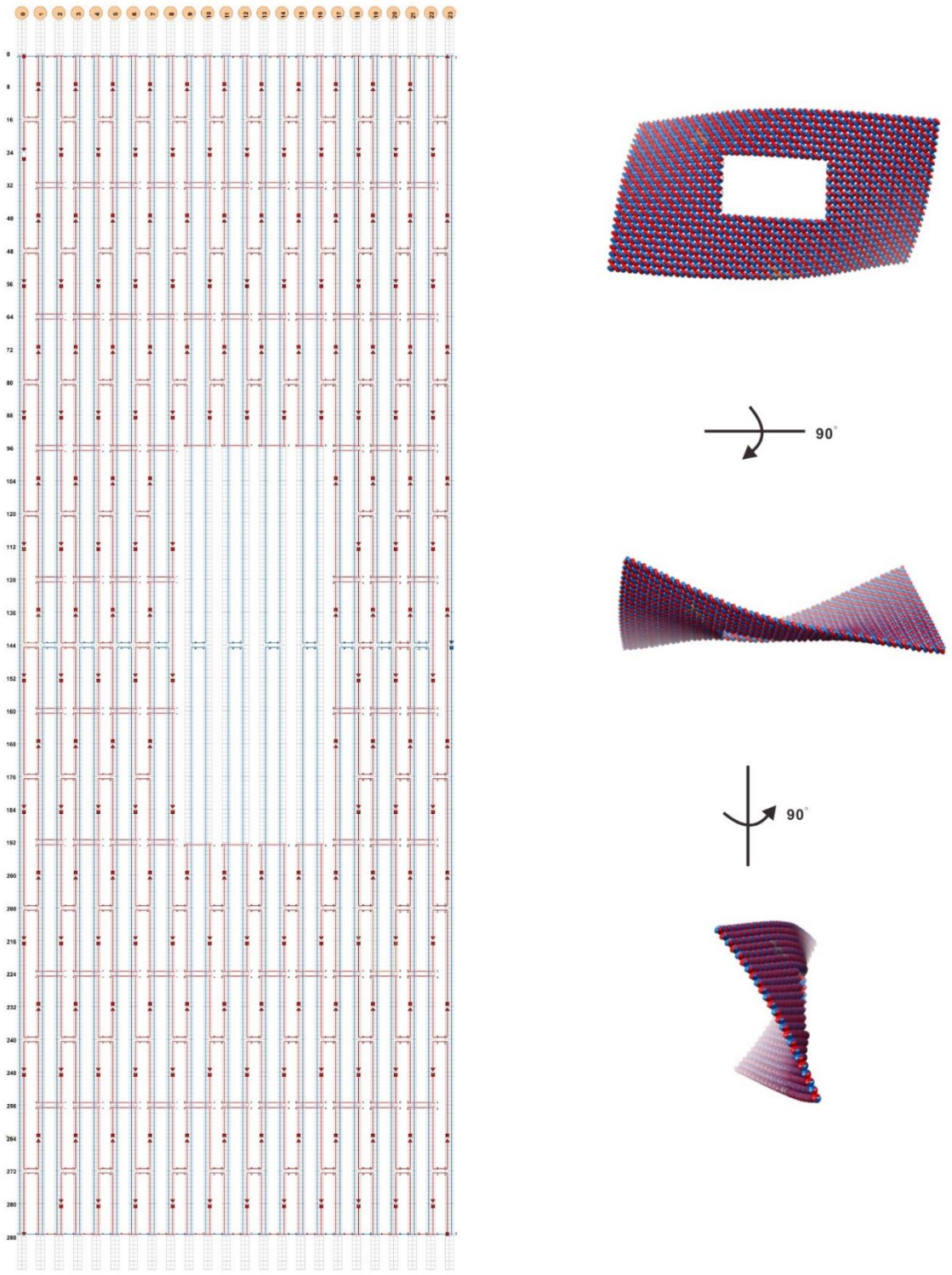

Figure 21 | Figure S17. Strand diagrams and predicted shapes of a theoretical rectangular structure with a 33 nm × 25 nm nanopore.

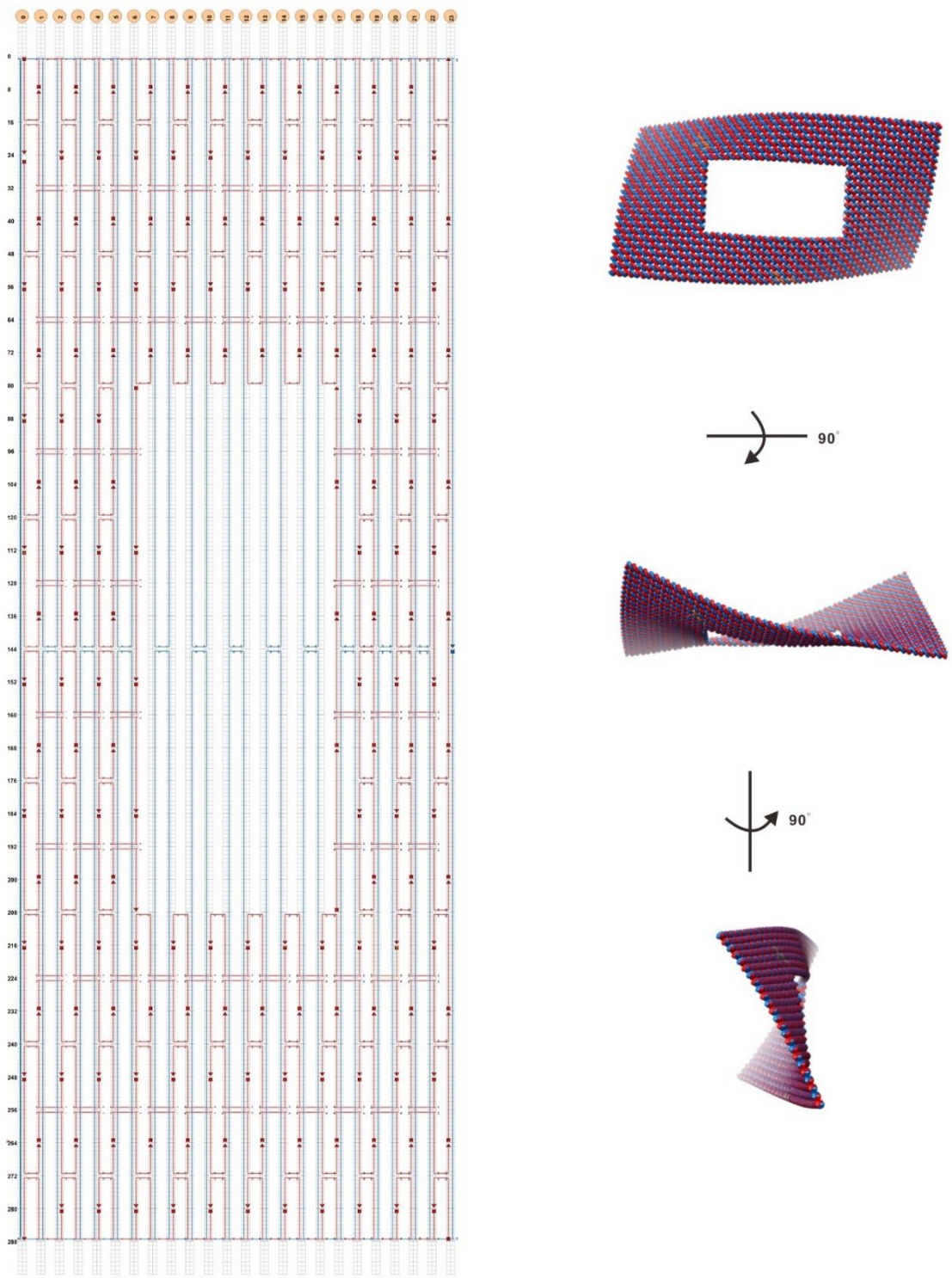

Figure 22 | Figure S18. Strand diagrams and predicted shapes of a theoretical rectangular structure with a 44 nm × 31 nm nanopore.

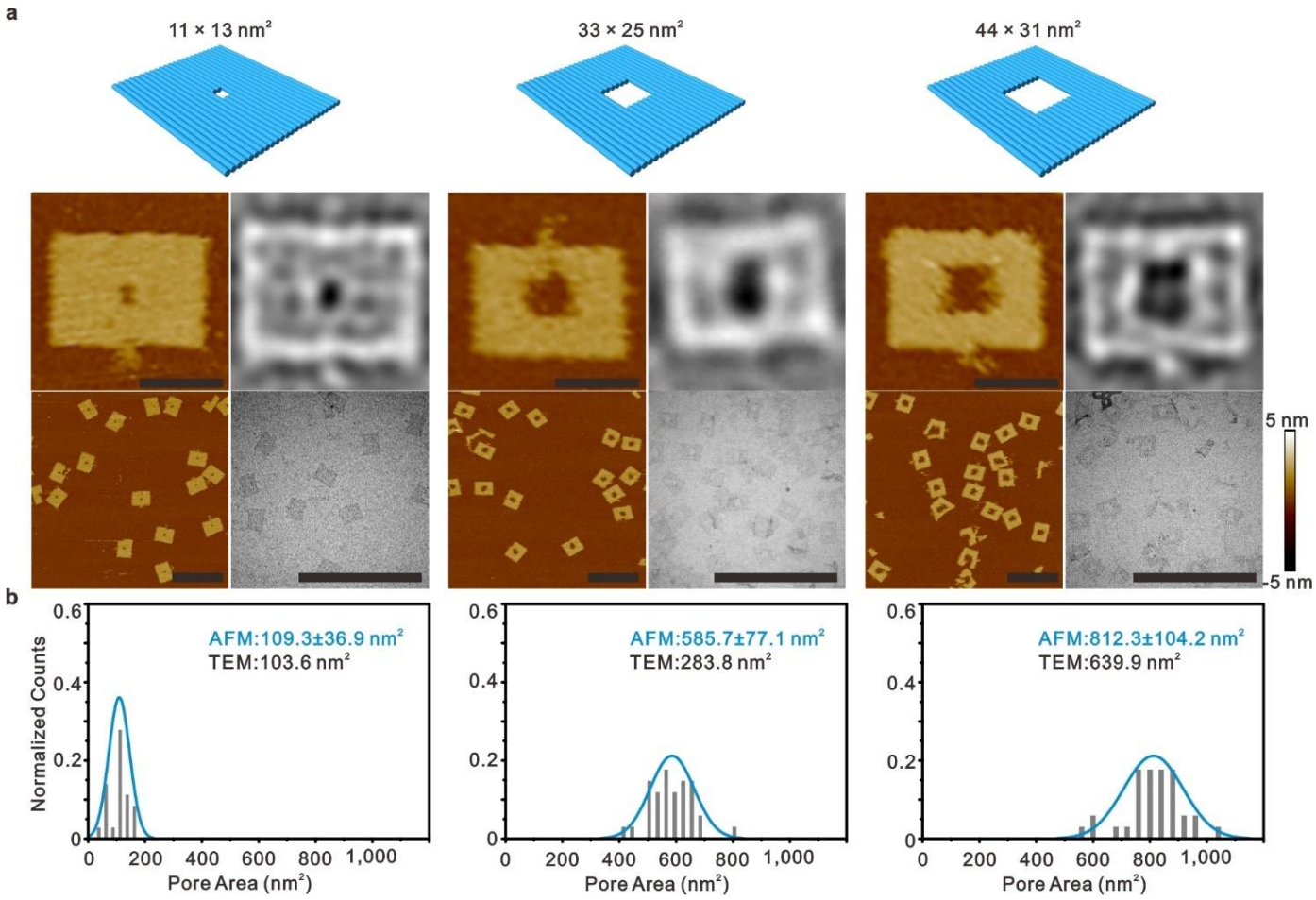

Figure 23 | AFM and TEM images of DNA nanopore frameworks and statistics of their size distribution. **a.** Three DNA nanopores that had different designs: 11 × 13 nm^2, 33 × 25 nm^2, 44 × 31 nm^2, which indicate the number of staple strands removed from the rectangle origami. The theoretical sizes were hard to determine because of the flexibility of the scaffold strand in the hole of the DNA. Using statistical methods, the nanopore areas in the AFM images were determined to be higher than that of the nanopore areas in the TEM images. This phenomenon may be attributed to the free scaffold in the pore and the DNA origami TEM sample suffer from shrinkage during the drying of the negatively stain. Scale bars, zoomed in, 50 nm, and zoomed out, 250 nm.

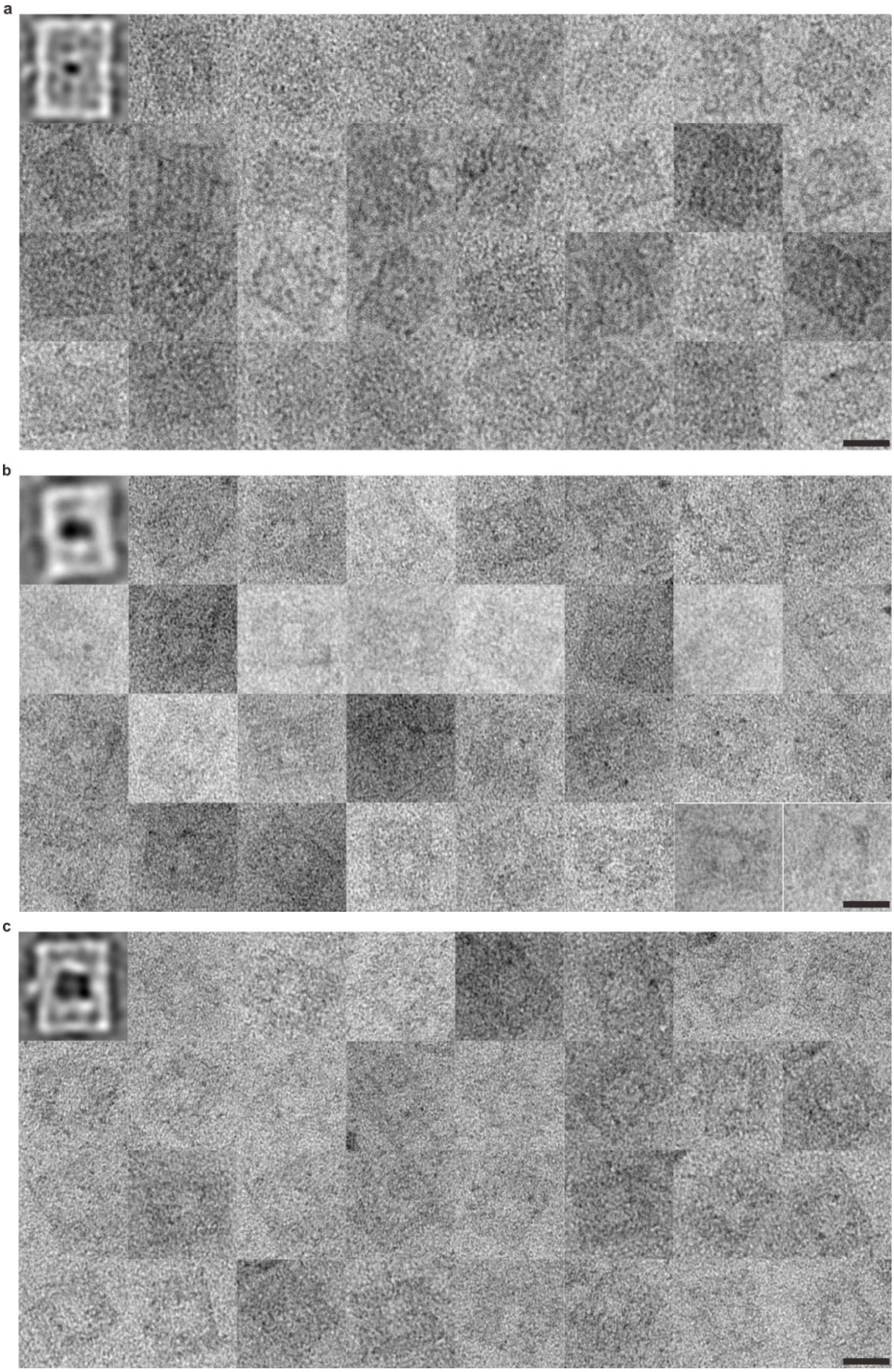

Figure 24 | Exemplary particle libraries of negatively stained DNA origami nanopores. a. b and c. Three different sized DNA origami nanopores. Top left insertions are class averaged TEM images that were obtained by using an EMAN2 software package, ver. 2.2. Scale bars, 50 nm.

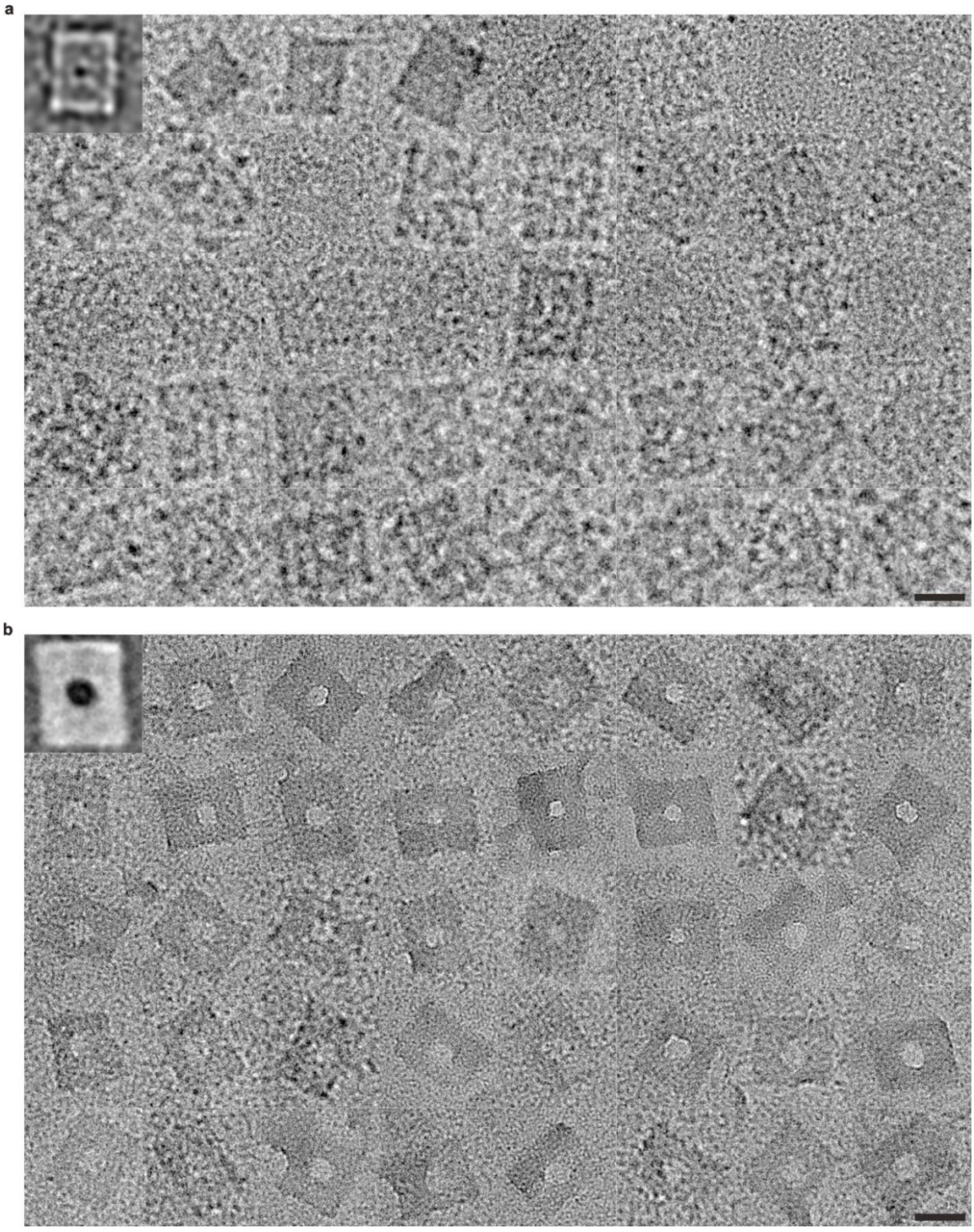
a
b

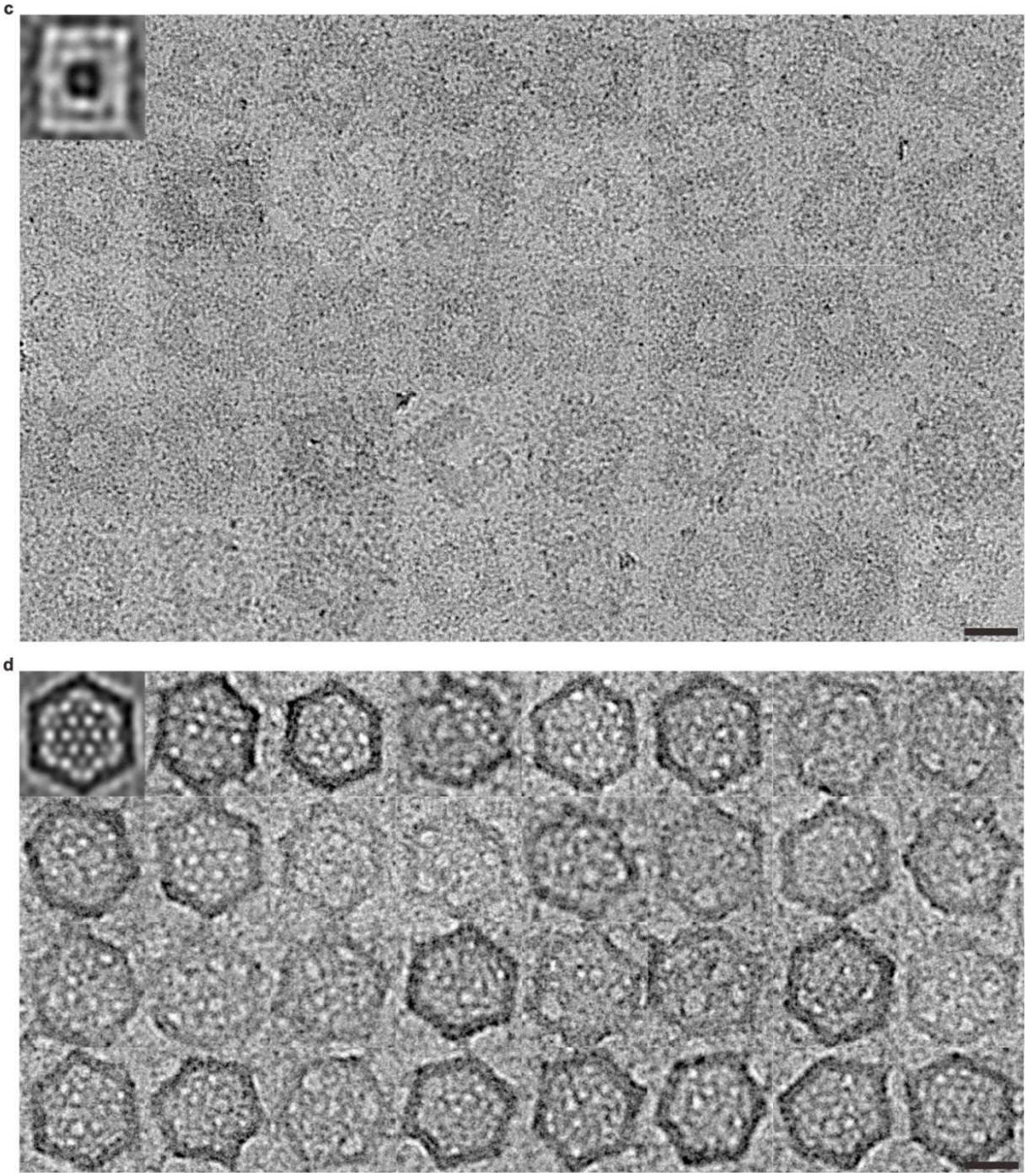

Figure 25 | Exemplary particle libraries of DOS nanopores. a, b and c. Three different sized DOS silica nanopores. Top left insertion, class averaged TEM images that were obtained by using an EMAN2 software package, ver. 2.2. **d.** DOS-diatom. Scale bar, 50 nm.

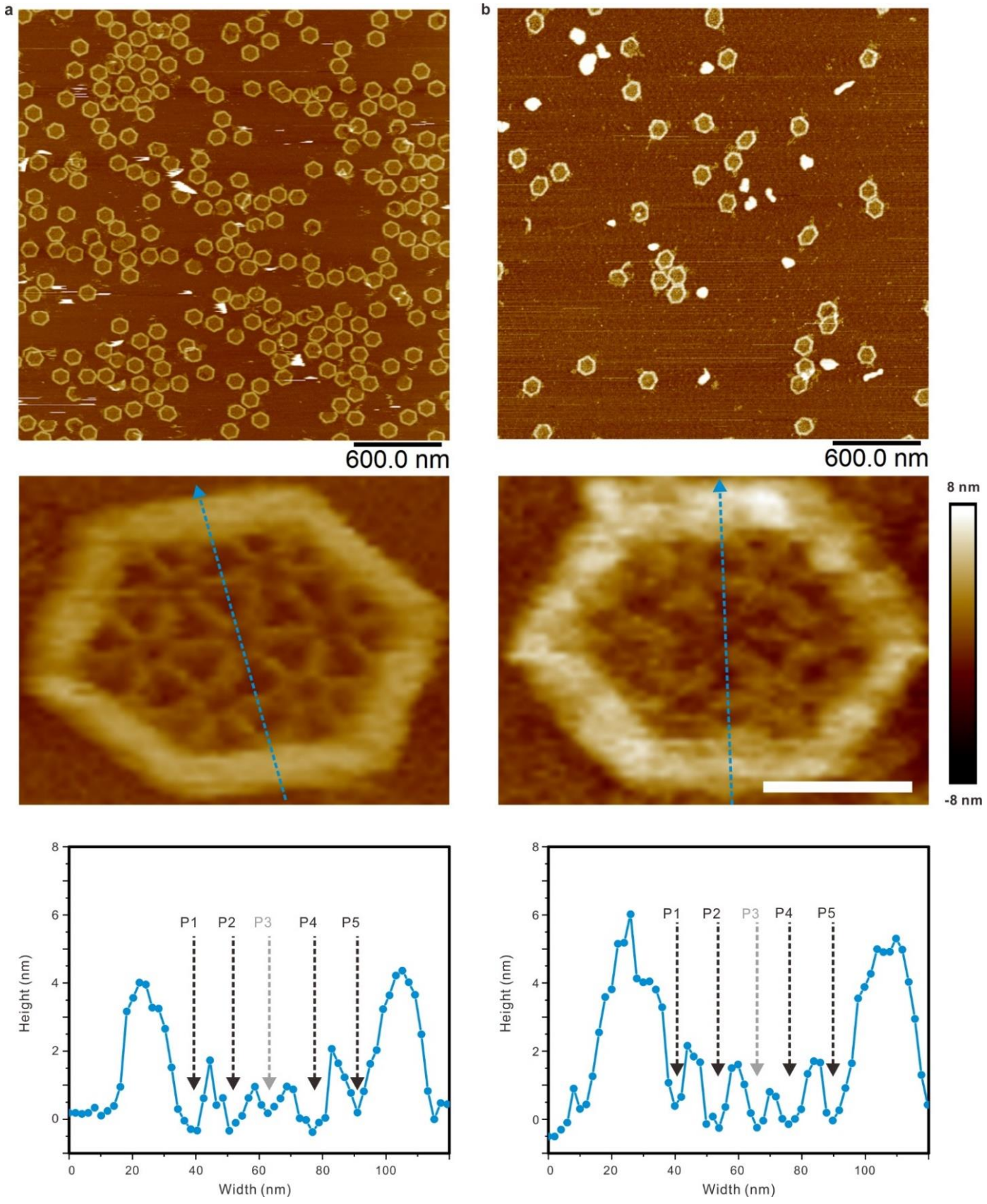

Figure 26 | AFM images of DNA-diatom before and after silicification. a. Pure DNA-origami. **b.** DOS-Diatoms mineralized for 2 days. The overall image of the DOS-Diatoms showed well-replicated geometries of the original DNA origami structures. The AFM height section profile revealed the well-formed nanopores along the scan line. Despite that, visualization of every single pore within the diatom-mimicking structure remained difficult due to the resolution limitation of our current AFM imaging technique.

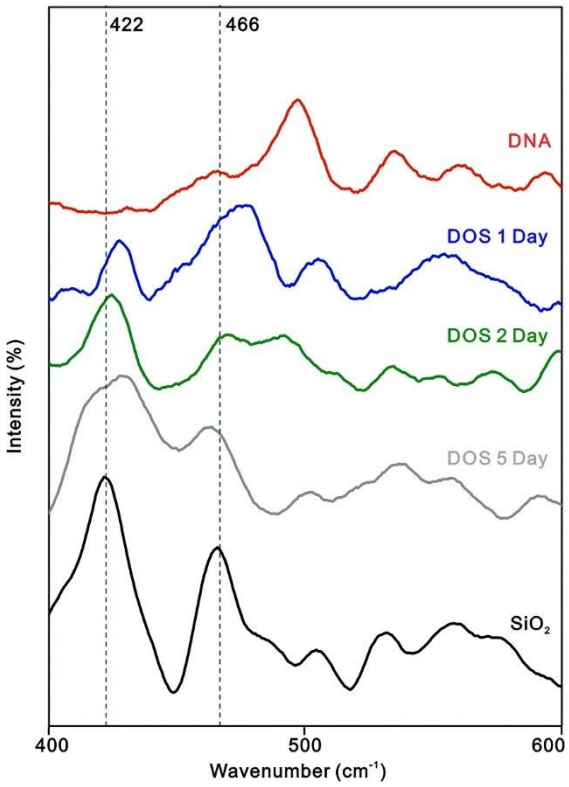

Figure 27 | Raman spectra of SiO_2, DNA, and DOS reacted for 1, 2 and 5 days, respectively. The bands at 422 cm^{-1} are associated with a Si-O-Si network bond bending vibration. The bands located at 466 cm^{-1} were associated with Si-O-Si network defects. Both of these two bands were observed during the silicification process because the intensity spiked at these two wavenumbers. The other bands of silicification that were produced between 500 cm^{-1} and 600 cm^{-1} were associated with the DNA base. The bands observed were associated with the standard bands in Table 1[45,46].

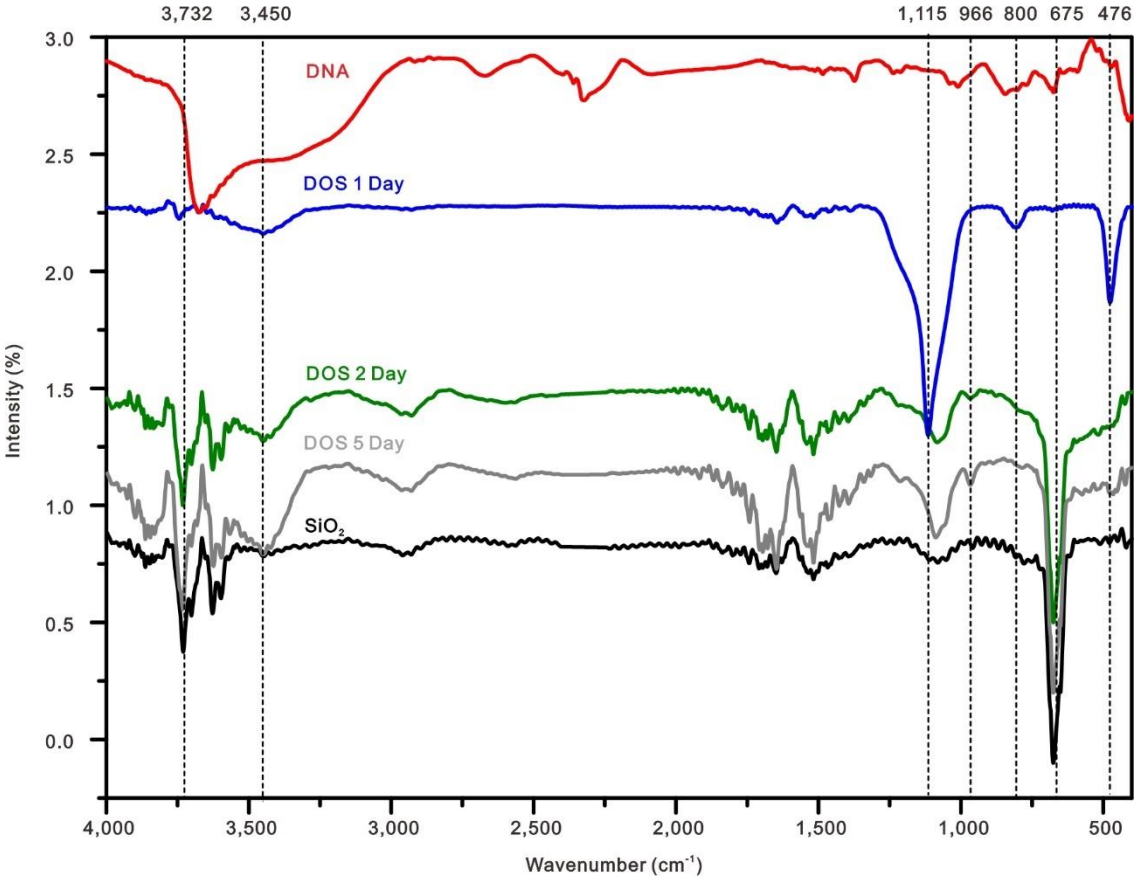

Figure 28 | IR spectra of SiO_2, DNA, and DOS reacted for 1, 2 and 5 days, respectively. The sudden decreases at 3,300 cm^{-1} and ~ 3,500 cm^{-1} can be attributed to adsorbed water and/or to silanol -OH hydrogen bonded groups. The bands that lie in the range of 3,650-3,750 cm^{-1} can be attributed to silanol -OH unassociated groups. The 1,115 cm^{-1} sudden decreases are associated with the TO mode of the Si-O-Si asymmetric bond stretching vibration. The 980 cm^{-1} bands are associated with the stretching mode of the Si-OH. The band at 800 cm^{-1} has been assigned to a Si-O-Si network symmetric bond stretching vibration. The bands at 675 cm^{-1} are associated with the Si-C-C asymmetric stretching vibration. The bands at 476 cm^{-1} are associated with a network Si-O-Si bond bending vibration[45].

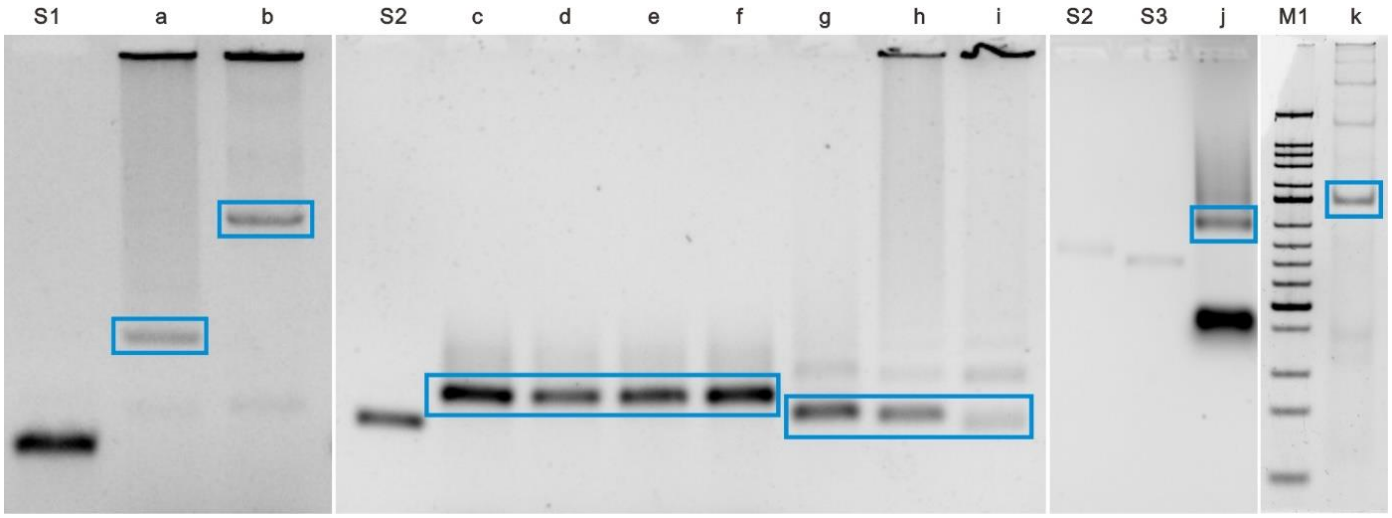

Figure 29 | Gel electrophoresis of different DNA frames. S1: P8064; a: tetrahedron-100 nm; b: cube; S2: M13mp18; c: triangle; d: rectangle; e: cross; f: 6-helix; g: hemisphere; h: toroid; i: ellipsoid; S3: phiX174 DNA; j: diatom; M1:50 bp DNA ladder; k: tetrahedron-16 nm; Blue box is drawn to highlight the target band.

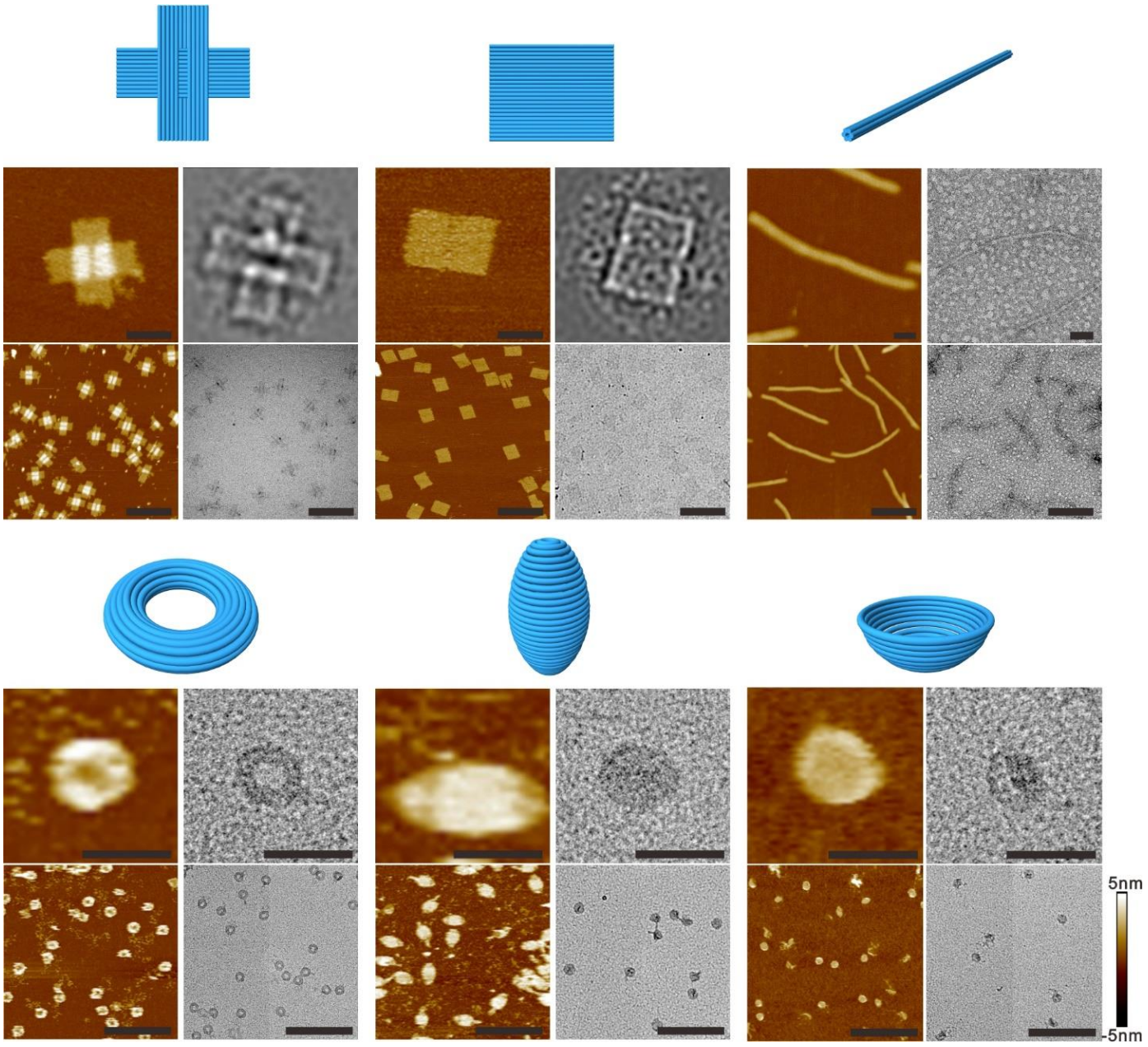

Figure 30 | AFM and TEM characterization of various DNA frames. Scale bars, zoomed in, 50 nm, and zoomed out, 250 nm.

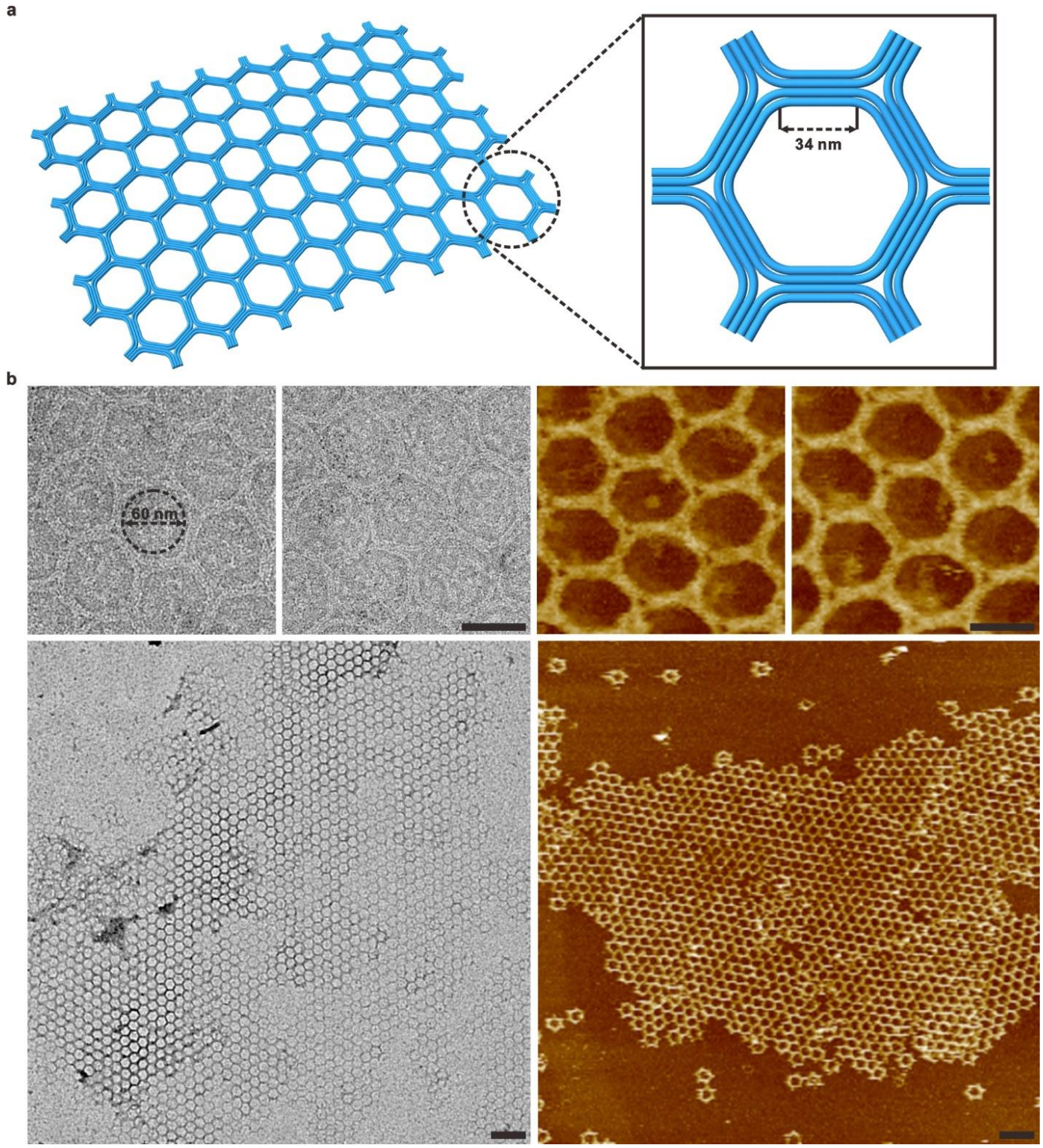

Figure 31 | DNA honeycomb framework. a. The honeycomb structure was assembled by using a hexagon DNA origami with an average pore diameter of ~ 60 nm[6]. **b.** Left column, TEM images of negatively stained samples; Right column, AFM images. Scale bars, zoomed in, 50 nm, and zoomed out, 200 nm.

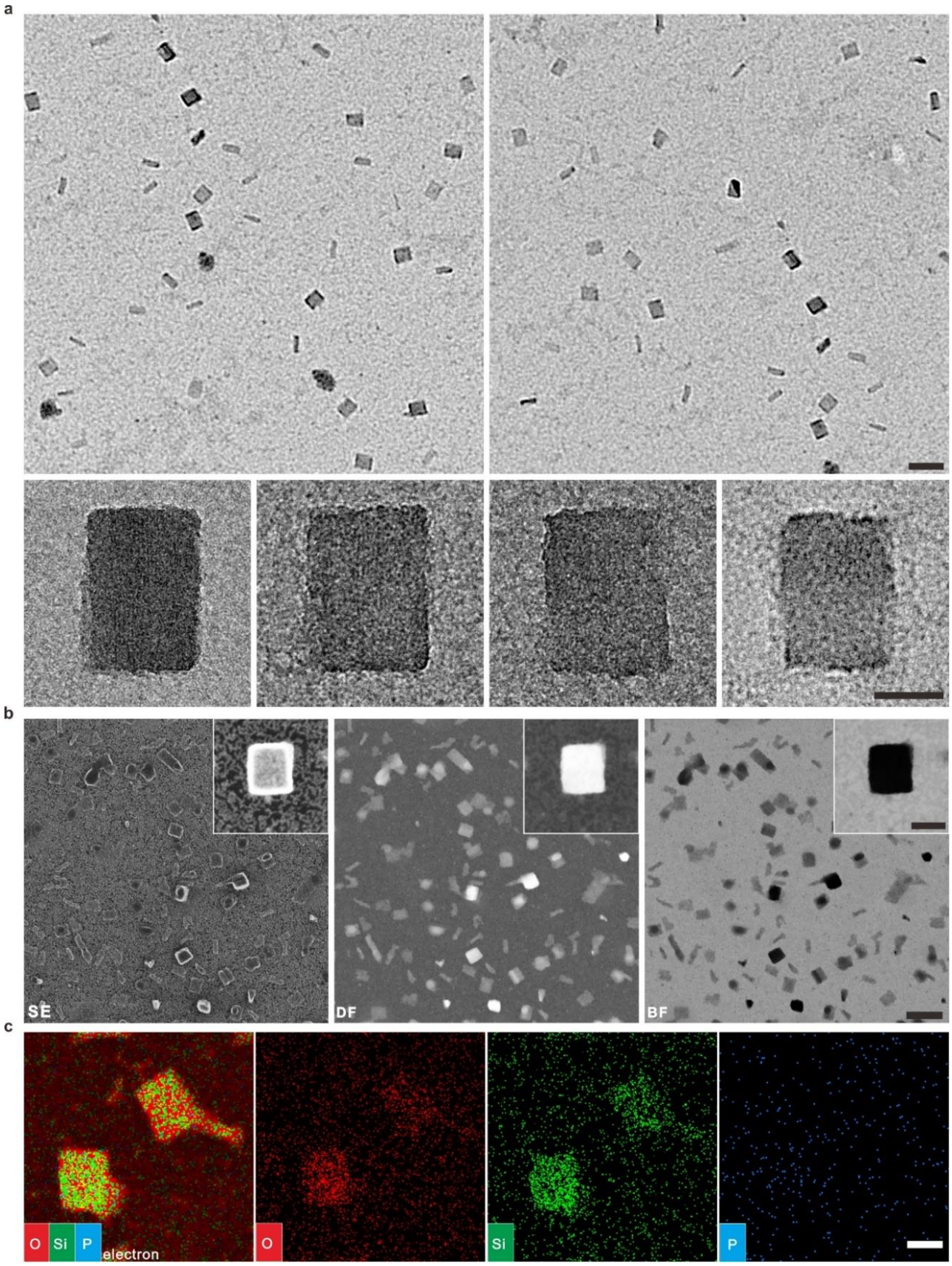

Figure 32 | EM and EDS characterization of a DOS rectangle. a. TEM zoomed out/in images showing the homogenous rectangular shaped DOS after 5 days of silicification. **b.** Second electron (SE), dark field (DF) and bright field (BF) STEM images of the sample. **c.** EDS mapping confirmed the micro-area chemical composition of the corresponding sample. From left to right, (Energy dispersive spectroscopy) EDS mapping overlapped with an SE-STEM image, O, Si mapping represent silica and P, O mapping represent DNA frameworks, respectively. Scale bars, zoomed in, 50 nm, and zoomed out, 200 nm.

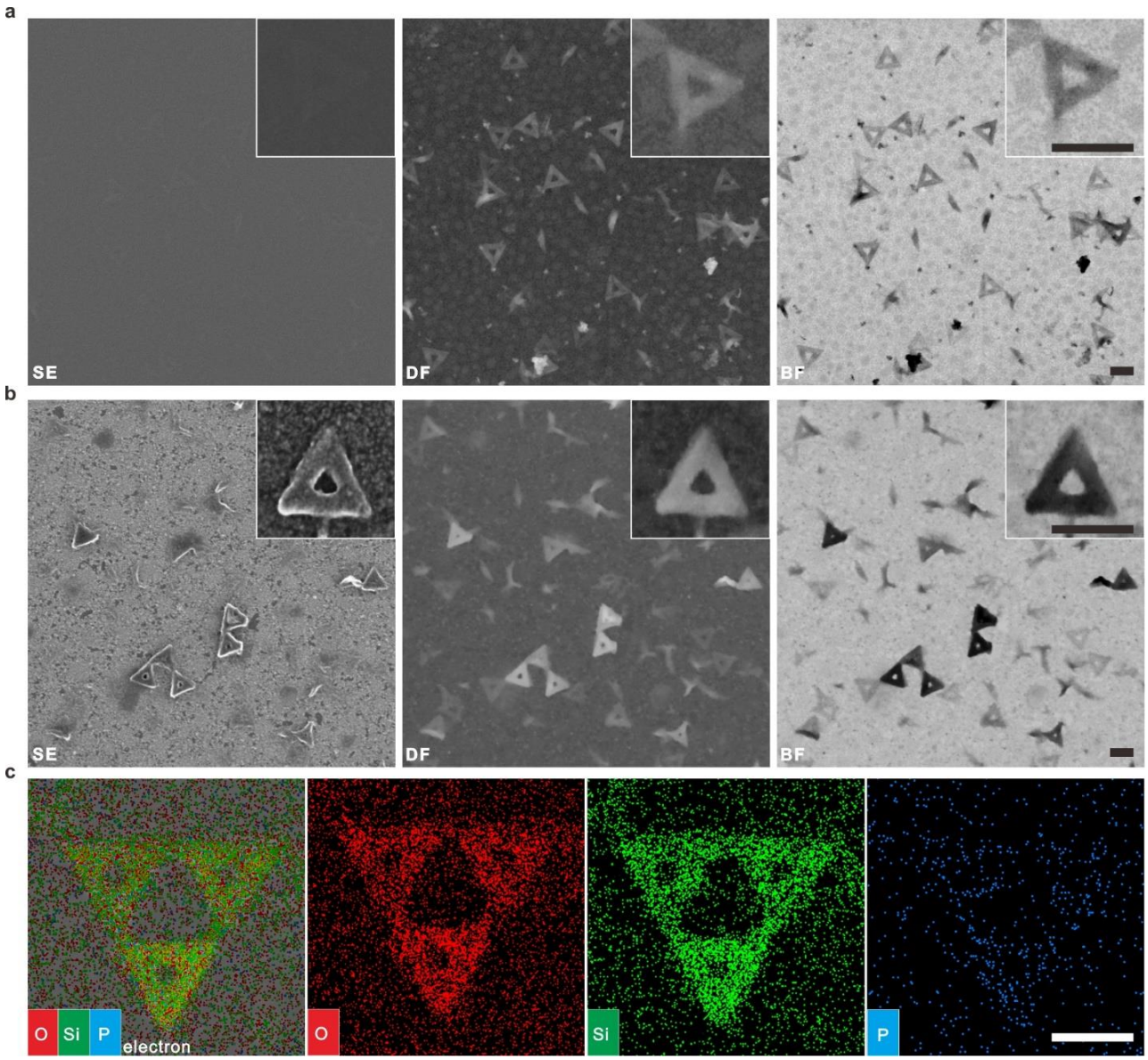

Figure 33 | STEM and EDS characterization of a DOS triangle. STEM zoomed out/in images (SE, DF and BF for the same area) show the homogenous triangular shaped DOS after **a.** 1 day and **b.** 5 days silicification. **c.** EDS mapping confirmed the micro-area chemical composition of the corresponding 5-day sample. From left to right, EDS mapping overlapped with SE-STEM image, O, Si mapping represent silica and P, O mapping represent DNA frameworks, respectively. Scale bars, 100 nm.

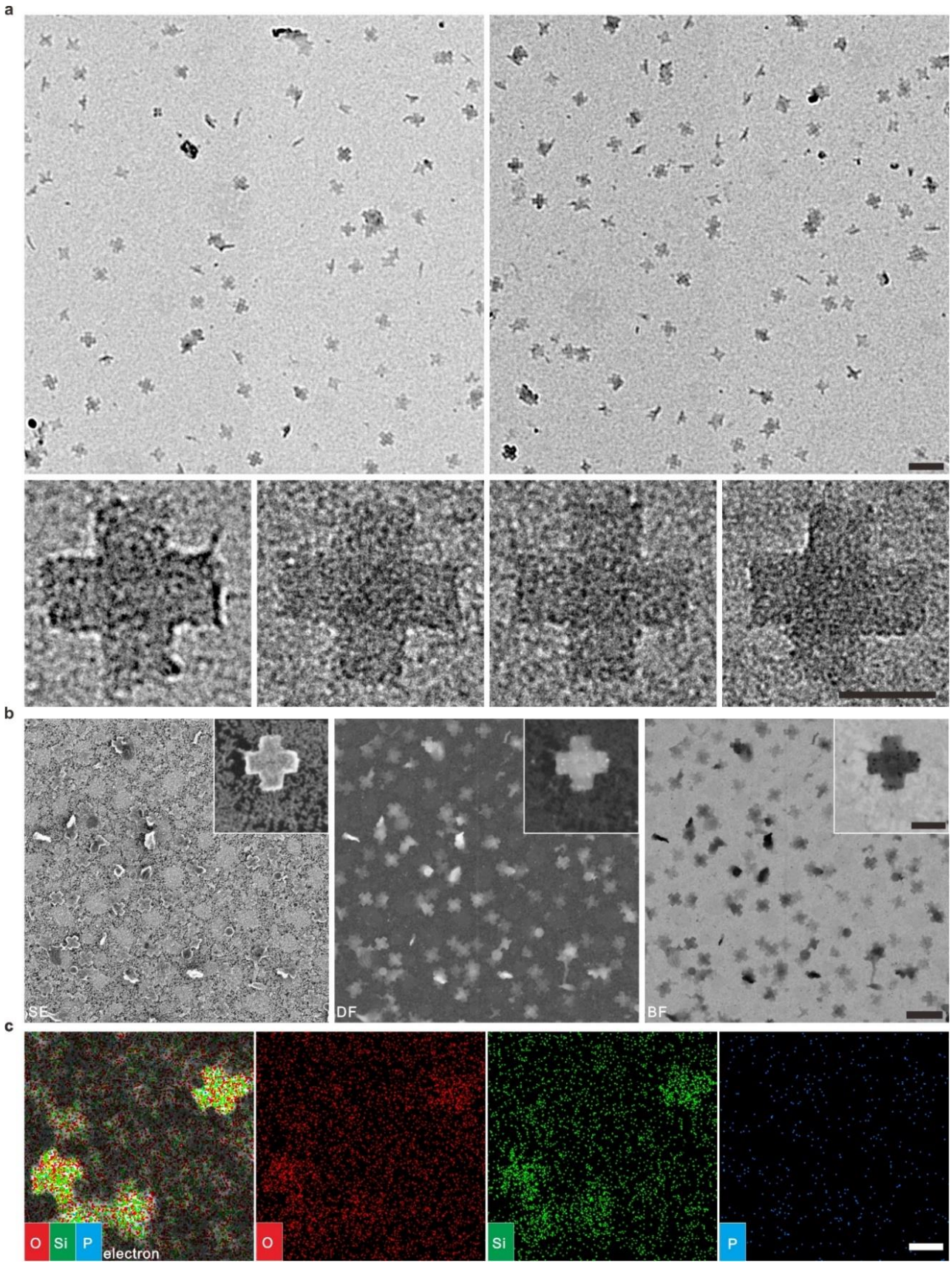

Figure 34 | EM and EDS characterization of a DOS cross. a. TEM zoomed out/in images show the homogenous cross-shaped DOS after 5 days of silicification. **b.** STEM zoomed out/in images (SE, DF and BF for the same area) of the same sample. **c.** EDS mapping confirmed the micro-area chemical composition of the corresponding sample. From left to right, EDS mapping overlapped with SE-STEM image, O, Si mapping represent silica and P, O mapping represent DNA frameworks, respectively. Scale bars, zoomed in, 50 nm, and zoomed out, 200 nm.

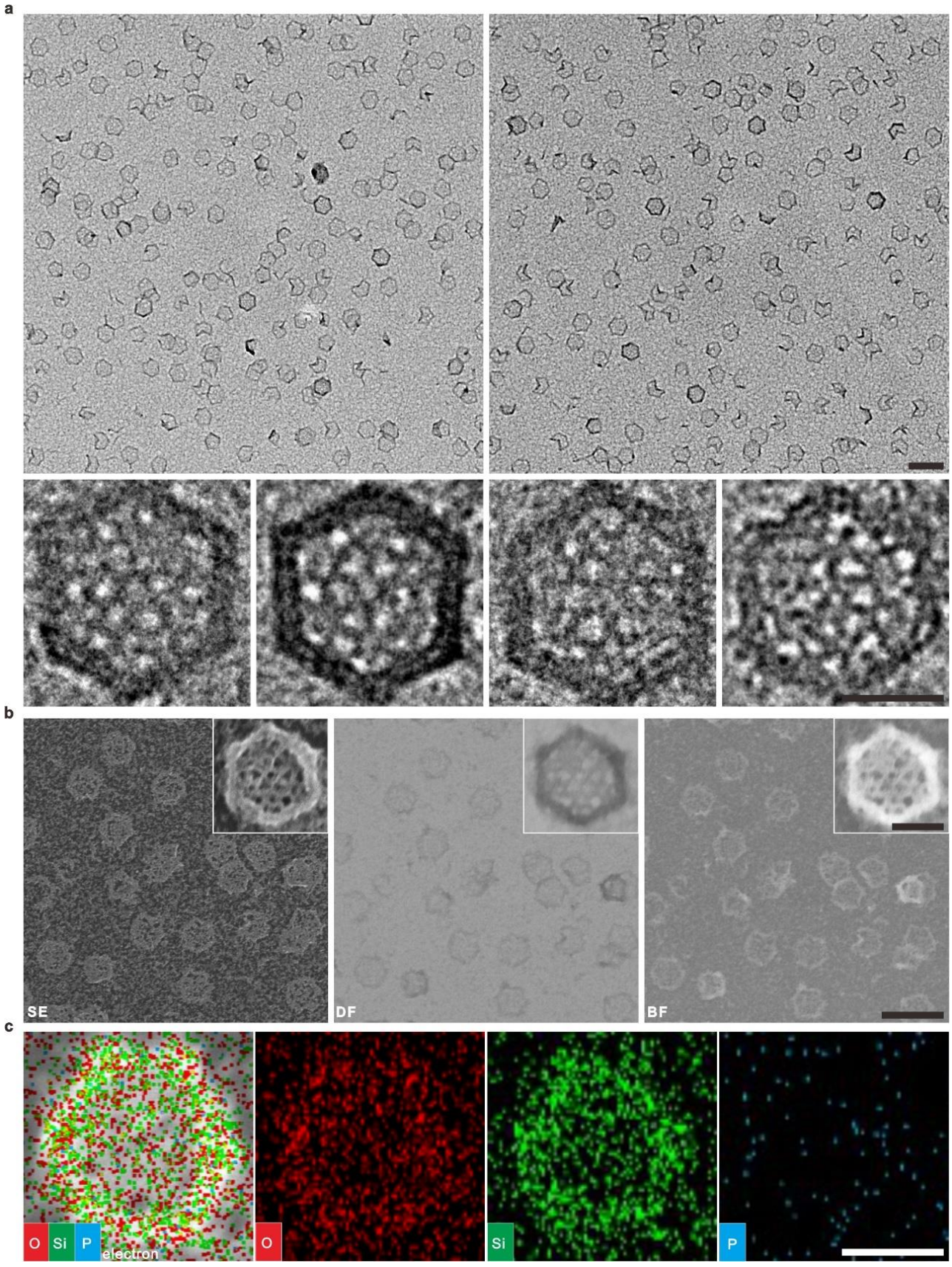

Figure 35 | EM and EDS characterization of a DOS diatom. a. TEM zoomed out/in images show the DOS-diatom after 5 days of silicification. **b.** STEM zoomed out/in images (SE, DF and BF for the same area) show the surface and inner details of the DOS diatom hierarchical structure. **c.** EDS mapping confirmed the chemical composition of the corresponding sample. From left to right, EDS mapping overlapped with SE-STEM image, O, Si mapping represent silica and P, O mapping represent DNA frameworks, respectively. Scale bars, zoomed in, 50 nm, and zoomed out, 200 nm.

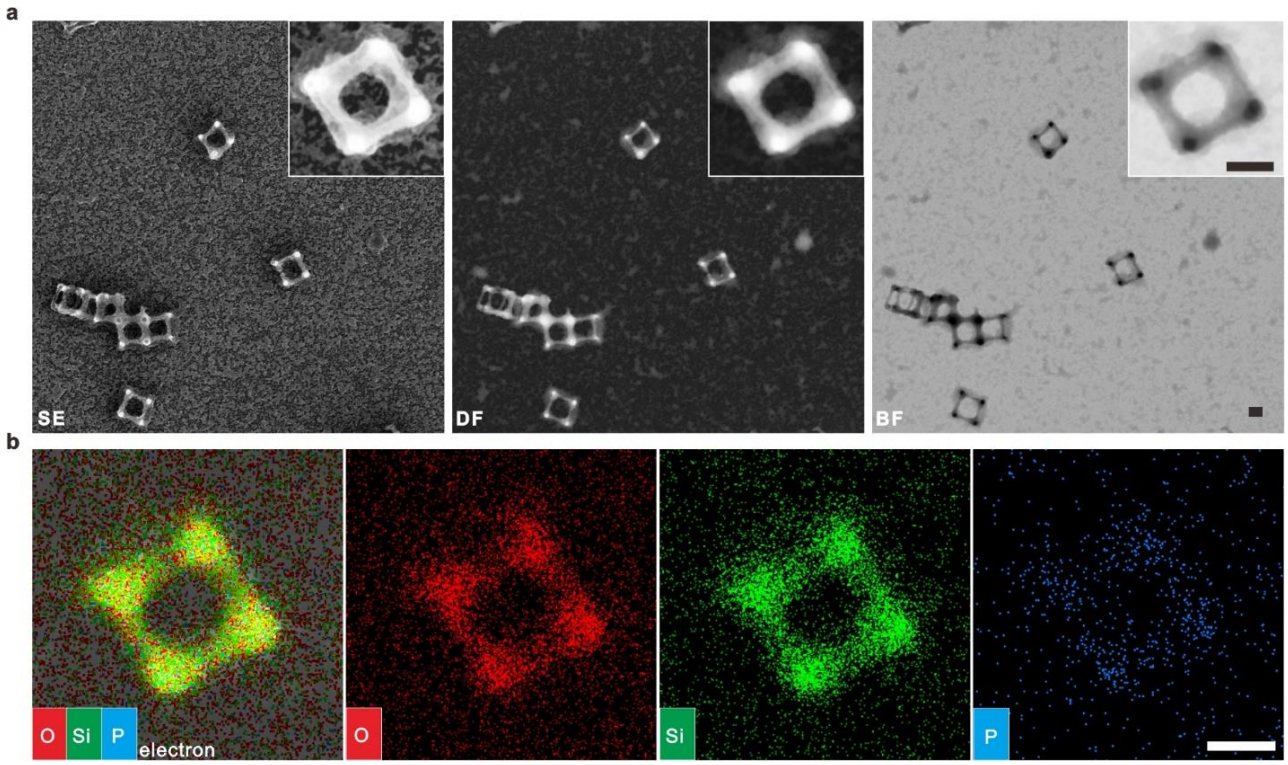

Figure 36 | STEM and EDS characterization of a DOS cube. a. STEM zoomed out/in images (SE, DF and BF for the same area) show the homogenous DOS cube after 5 days of silicification. **b.** EDS mapping confirmed the micro-area chemical composition of the corresponding sample. From left to right, EDS mapping overlapped with SE-STEM image, O, Si mapping represent silica and P, O mapping represent DNA frameworks, respectively. Scale bars, 50 nm.

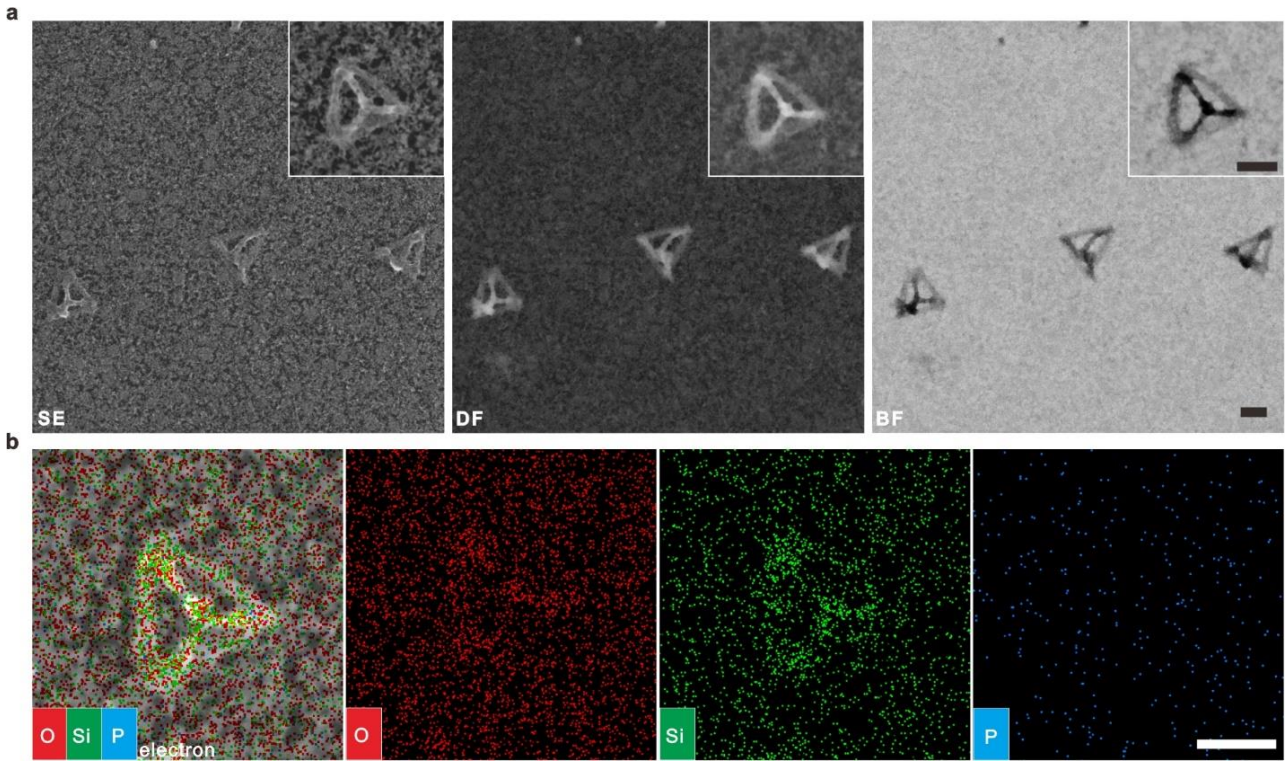

Figure 37 | STEM and EDS characterization of a DOS tetrahedron. a. STEM zoomed out/in images (SE, DF and BF for the same area) shows the homogenous DOS tetrahedron after 5 days of silicification. **b.** EDS mapping confirmed the micro-area chemical composition of the corresponding sample. From left to right, EDS mapping overlapped with SE-STEM image, O, Si mapping represent silica and P, O mapping represent DNA frameworks, respectively. Scale bars, 50 nm.

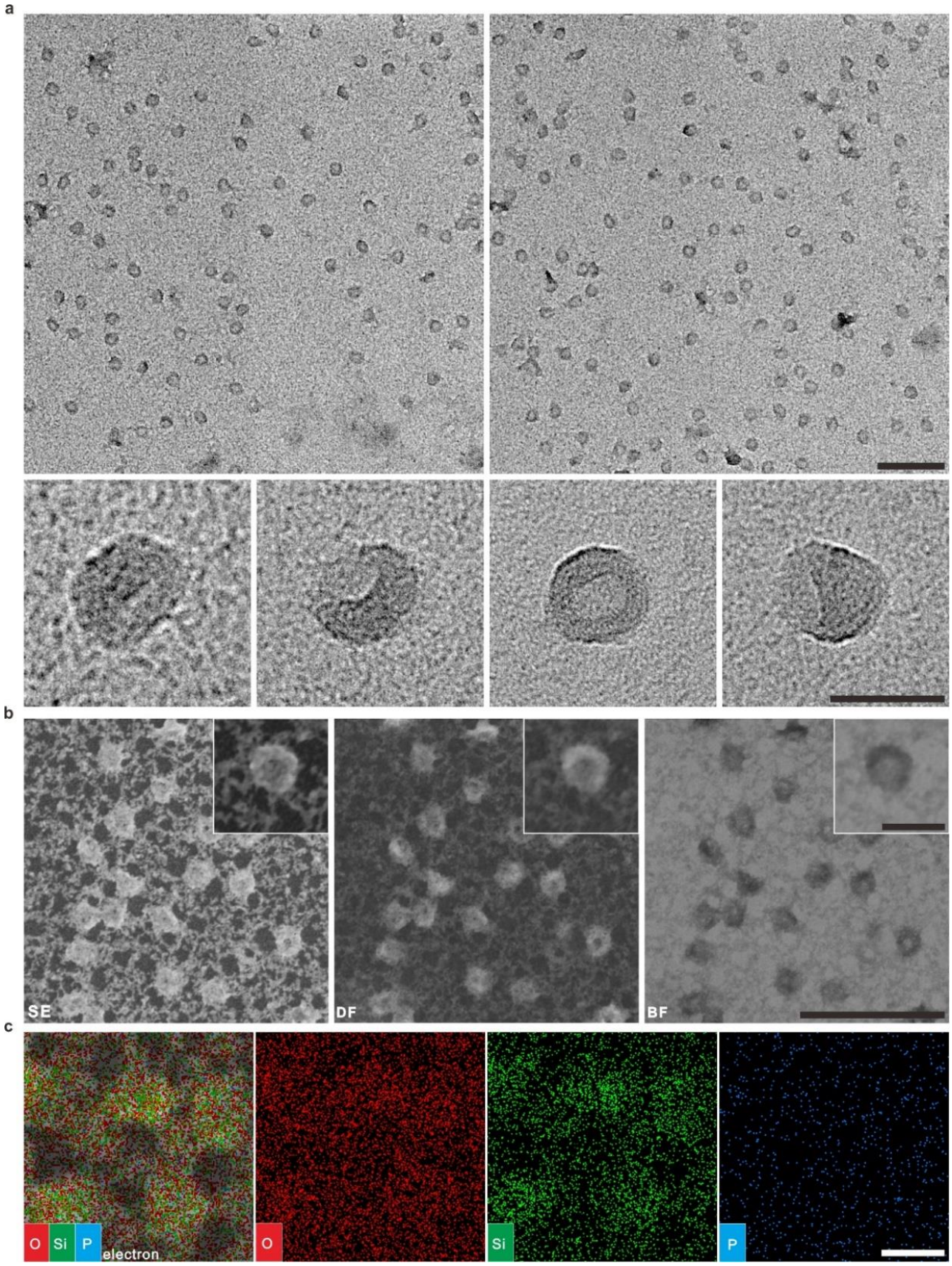

Figure 38 | EM and EDS characterization of a DOS hemisphere. a. TEM zoomed out/in images show the homogenous DOS hemisphere after 5 days of silicification. **b.** STEM zoomed out/in images (SE, DF and BF for the same area) of the same sample. **c.** EDS mapping confirmed the micro-area chemical composition of the corresponding sample. From left to right, EDS mapping overlapped with SE-STEM image, O, Si mapping represent silica and P, O mapping represent DNA frameworks, respectively. Scale bars, zoomed in, 50 nm, and zoomed out, 200 nm.

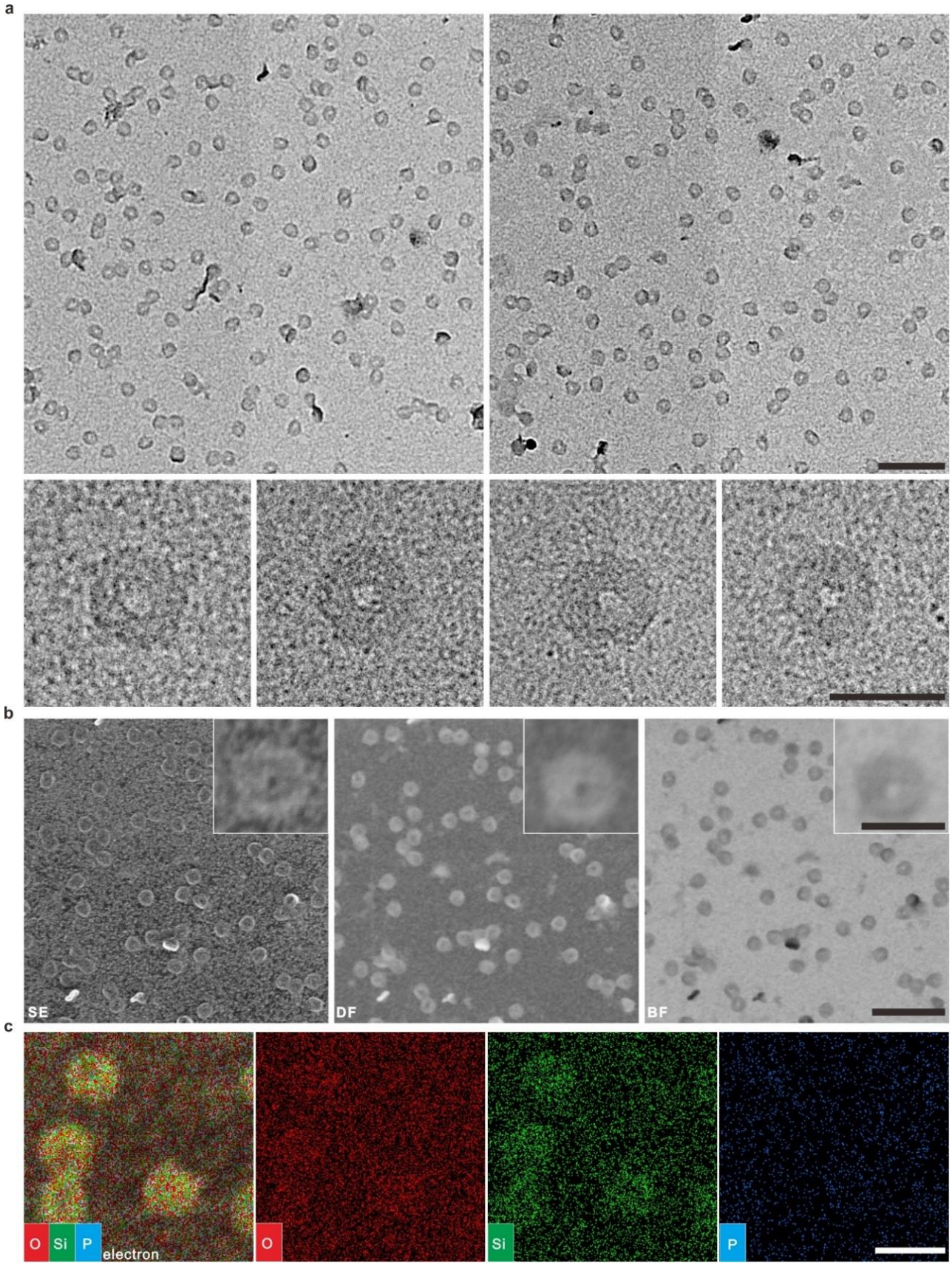

Figure 39 | EM and EDS characterization of a DOS toroid. a. TEM zoomed out/in images show the homogenous DOS toroid after 5 days of silicification. **b.** STEM zoomed out/in images (SE, DF and BF for the same area) of the same sample. **c.** EDS mapping confirmed the micro-area chemical composition of the corresponding sample. From left to right, EDS mapping overlapped with SE-STEM image, O, Si mapping represent silica and P, O mapping represent DNA frameworks, respectively. Scale bars, zoomed in, 50 nm, and zoomed out, 200 nm.

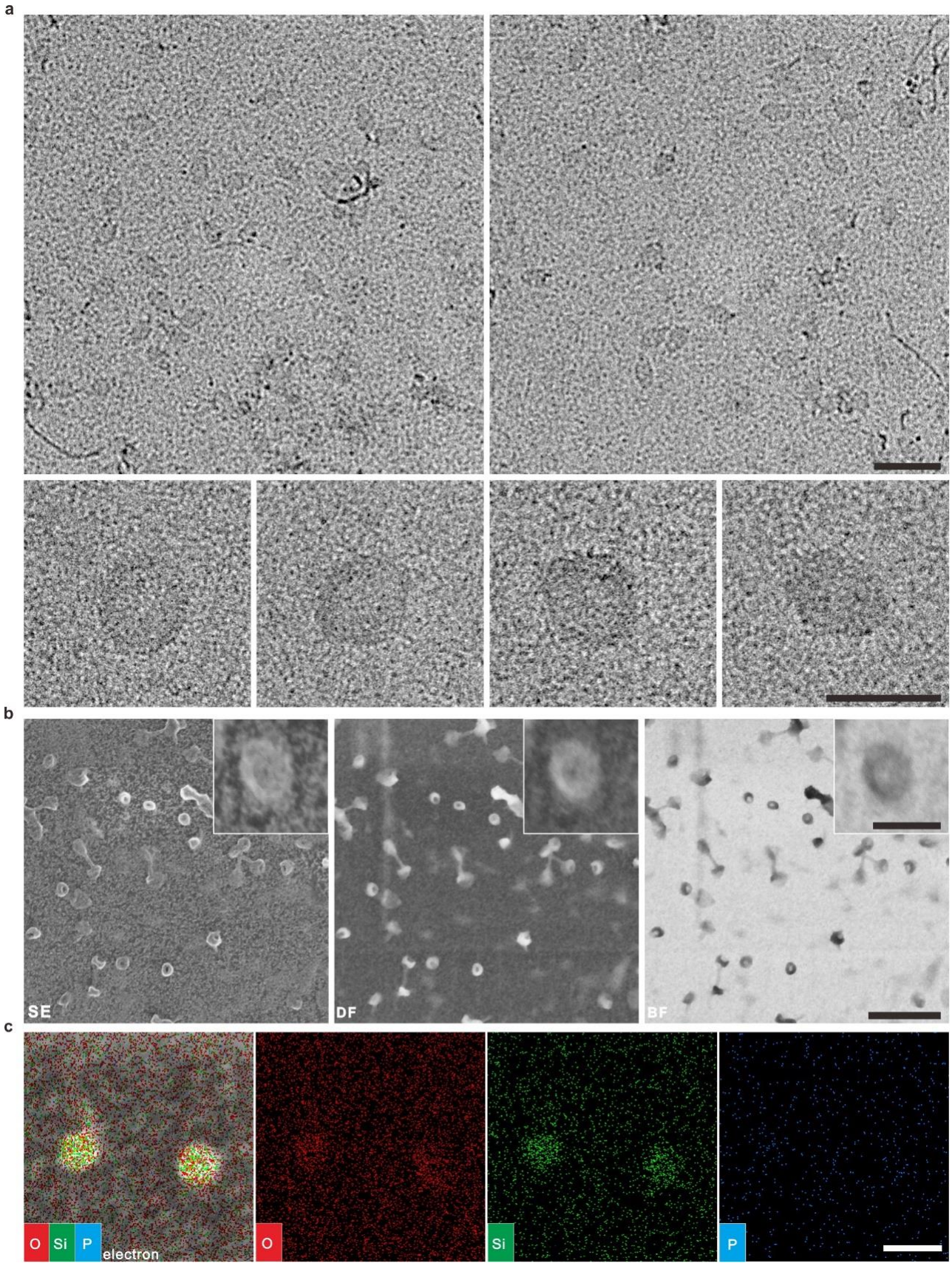

Figure 40 | EM and EDS characterization of a DOS ellipsoid. a. TEM zoomed out/in images show the homogenous DOS ellipsoid after 5 days of silicification. **b.** STEM zoomed out/in images (SE, DF and BF for the same area) of the same sample. **c.** EDS mapping confirmed the micro-area chemical composition of the corresponding sample. From left to right, EDS mapping overlapped with SE-STEM image, O, Si mapping represent silica and P, O mapping represent DNA frameworks, respectively. Scale bars, zoomed in, 50 nm, and zoomed out, 200 nm.

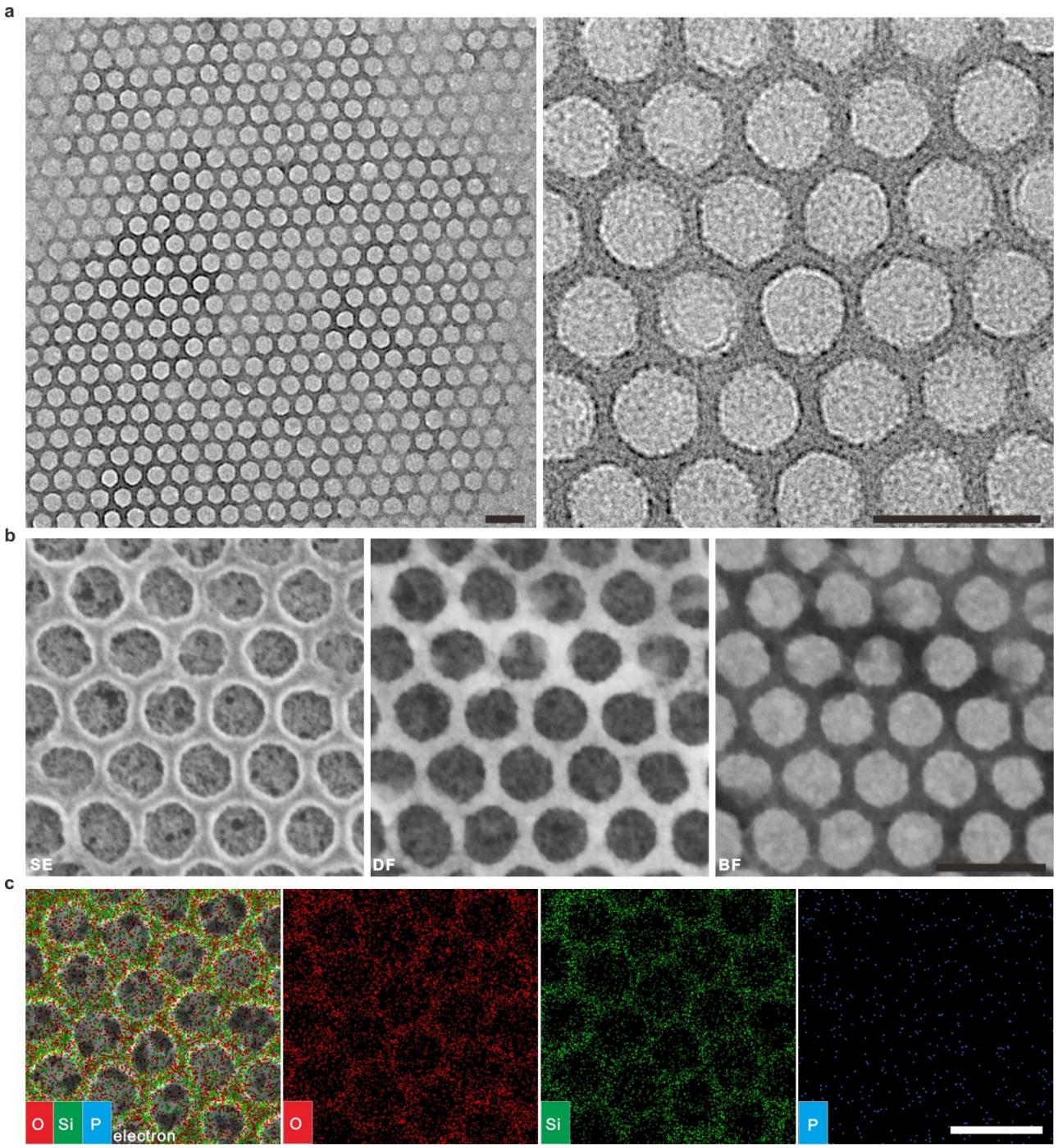

Figure 41 | EM and EDS characterization of a DOS honeycomb. A. TEM zoomed out/in images show the homogenous DOS honeycomb after 1 day of silicification. **B.** Second electron (SE), dark field (DF) and bright field (BF) STEM images show the surface and inner details of the DOS honeycomb sample. The irregular floccules in the honeycomb hole might be due to substrate contamination by freely deposited amorphous silica clusters. **C.** Energy dispersive spectrometer (EDS) mapping confirmed the micro-area chemical composition of the corresponding sample. From left to right, EDS mapping overlapped with SE-STEM image, O, Si mapping represent silica and P, O mapping represent DNA frameworks, respectively. Scale bars, 100 nm.

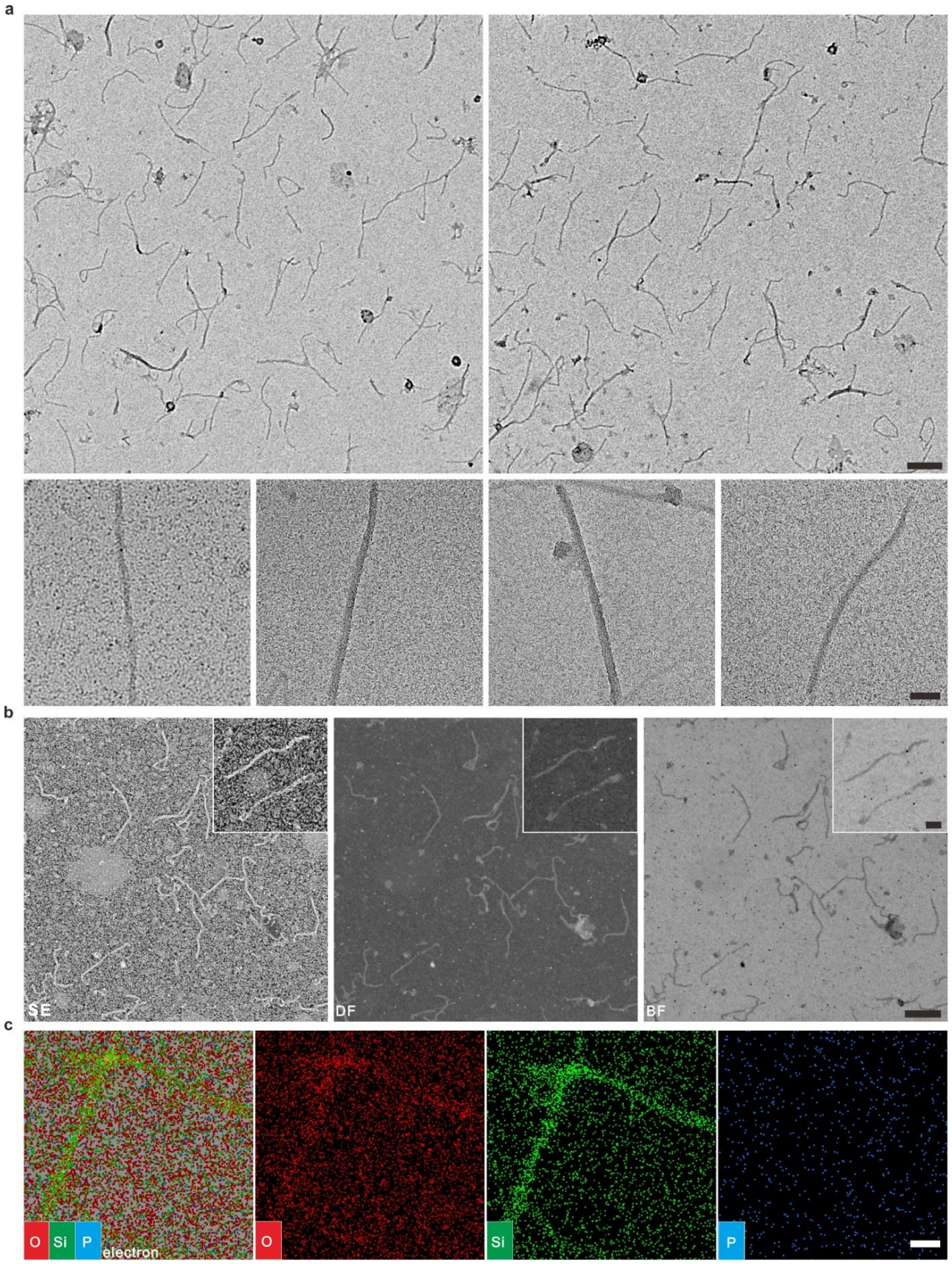

Figure 42 | EM and EDS characterization of a DOS 6-helix. A. TEM zoomed out/in images show the homogenous DOS 6-helix after 5 days of silicification. **B.** STEM zoomed out/in images (SE, DF and BF for the same area) of the same sample. **C.** EDS mapping confirmed the micro-area chemical composition of the corresponding sample. From left to right, EDS mapping overlapped with SE-STEM image, O, Si mapping represent silica and P, O mapping represent DNA frameworks, respectively. Scale bars, zoomed in, 50 nm, and zoomed out, 200 nm.

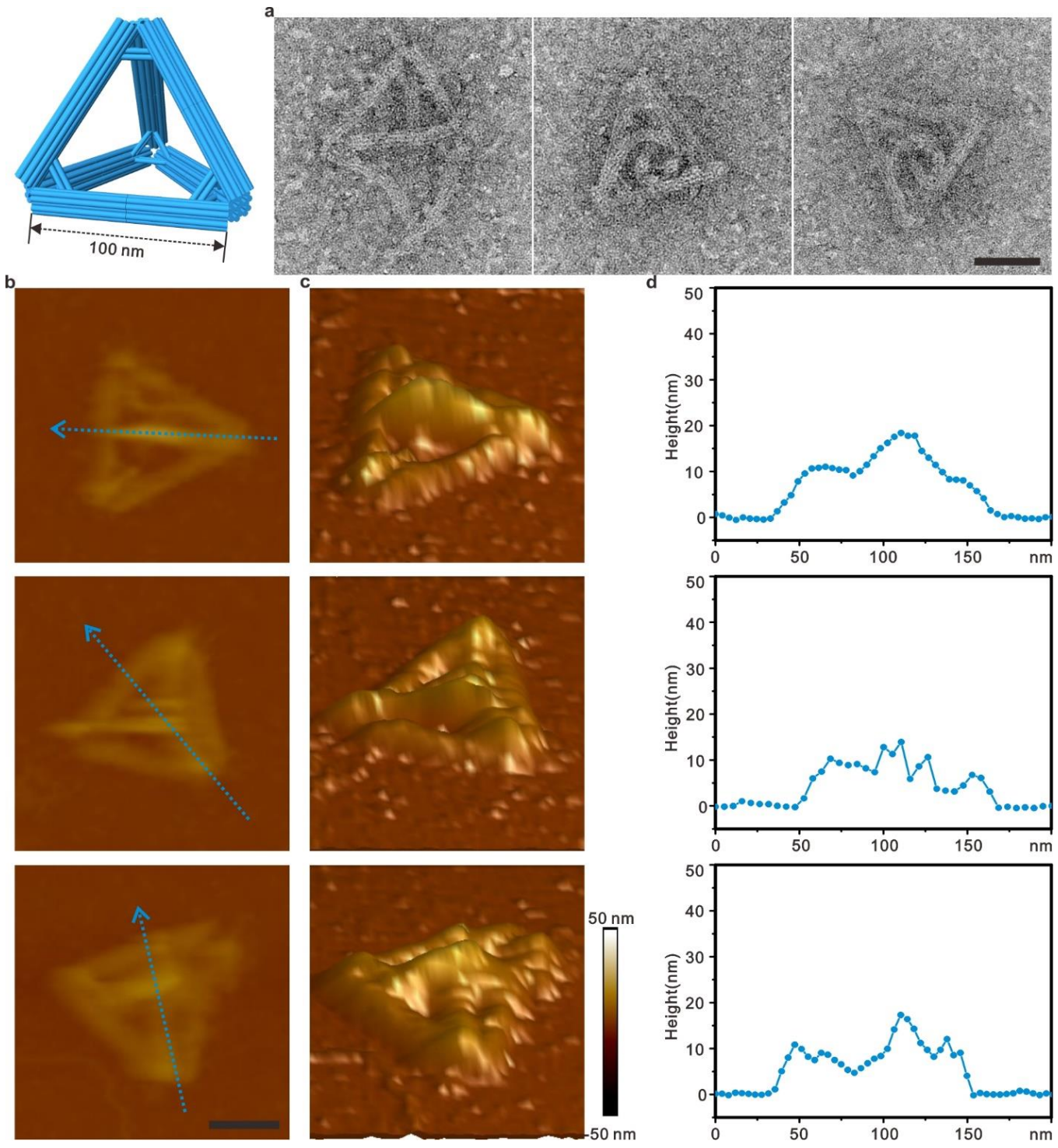

Figure 43 | TEM and AFM characterization of a tetrahedron DNA origami (100 nm in side length). a. Negatively stained TEM images. **b**. 2D images taken with AFM in fluid mode. **c**. Corresponding 3D images. **d.** Height of one edge. For TEM images, this kind of DNA origami is always distorted on the carbon film surface because the rigidity of the DNA frame was not strong enough. While a few of the tetrahedrons in the sample were upright, usually the three edges at the top were always distorted. The low rigidity of the DNA origami structures was more obvious in the AFM images. The three edges at the top of the structures were flattened even under the lowest forces used (about 50 pN). The peaks were no more than 20 nm, while the theoretical height of a rigid tetrahedron is 74.0 nm, which indicated a total collapse of such structures. Scale bars, 50 nm.

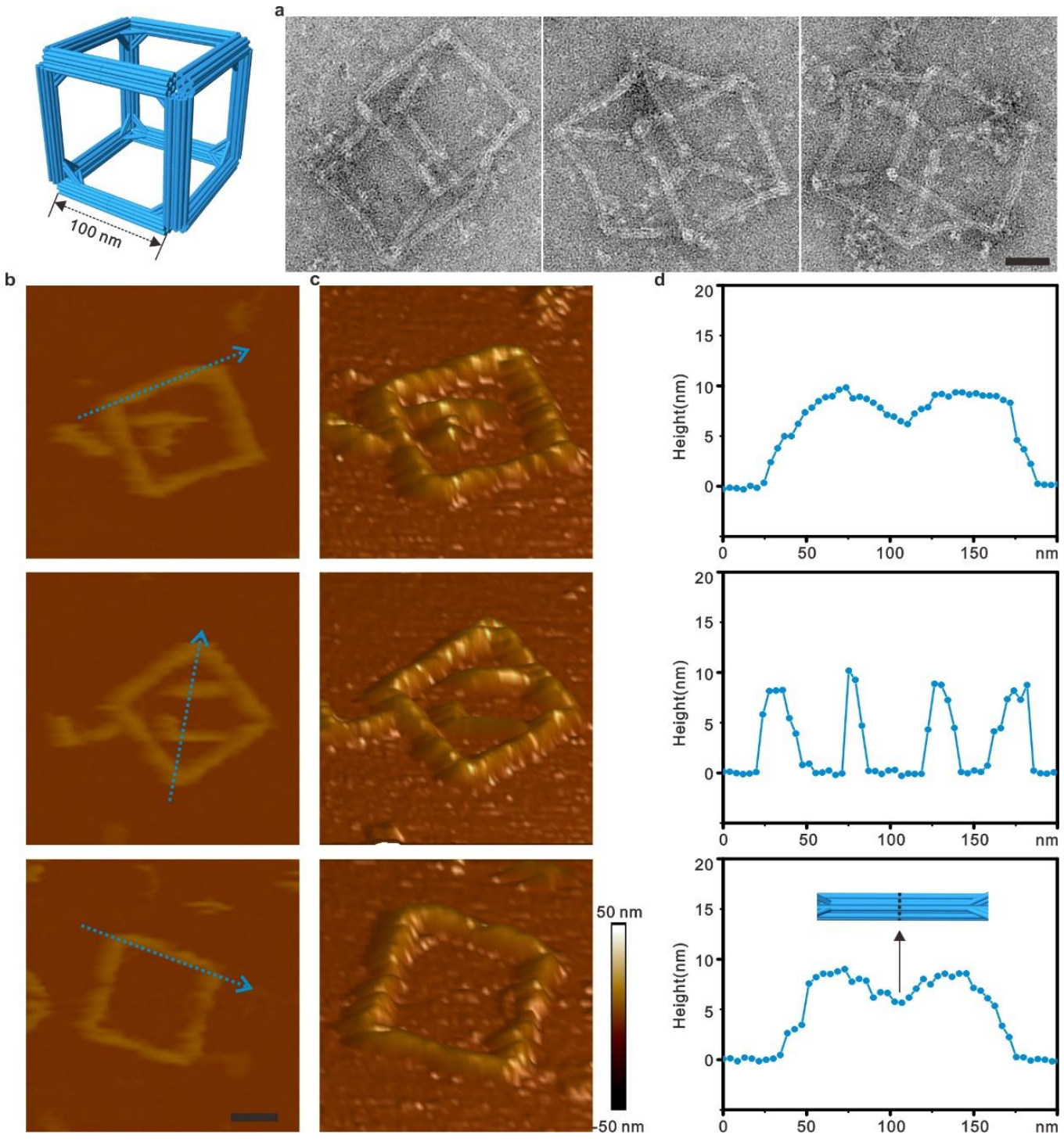

Figure 44 | TEM and AFM characterization of a cube DNA origami (100 nm in side length). a. Negatively stained TEM images. Almost all of the cube DNA origami structures were distorted on the carbon film surfaces. The distortion was caused by a lack of rigidity. The cube configuration had a much worse rigidity than the tetrahedrons. However, a square shape could be seen if the cube structure was standing up on the carbon film surface. **b**. 2D image taken with AFM in fluid mode. **c**. Corresponding 3D images. **d.** The height of one edge (top image). Only the four bottom edges and some destroyed edges could be seen after scanning with AFM tips in fluid mode (middle image). However, the side edges could not be identified because the heights of the vertices and the edges were too similar to one another. Interestingly, we found that the height in the middle of the bottom edges were a little lower than the heights of either the vertices or the ends of the edges (bottom image). This depression (loss in height) may be the gap between the joints of the two tripods, which is marked in the bottom image of d. Scale bars, 50 nm.

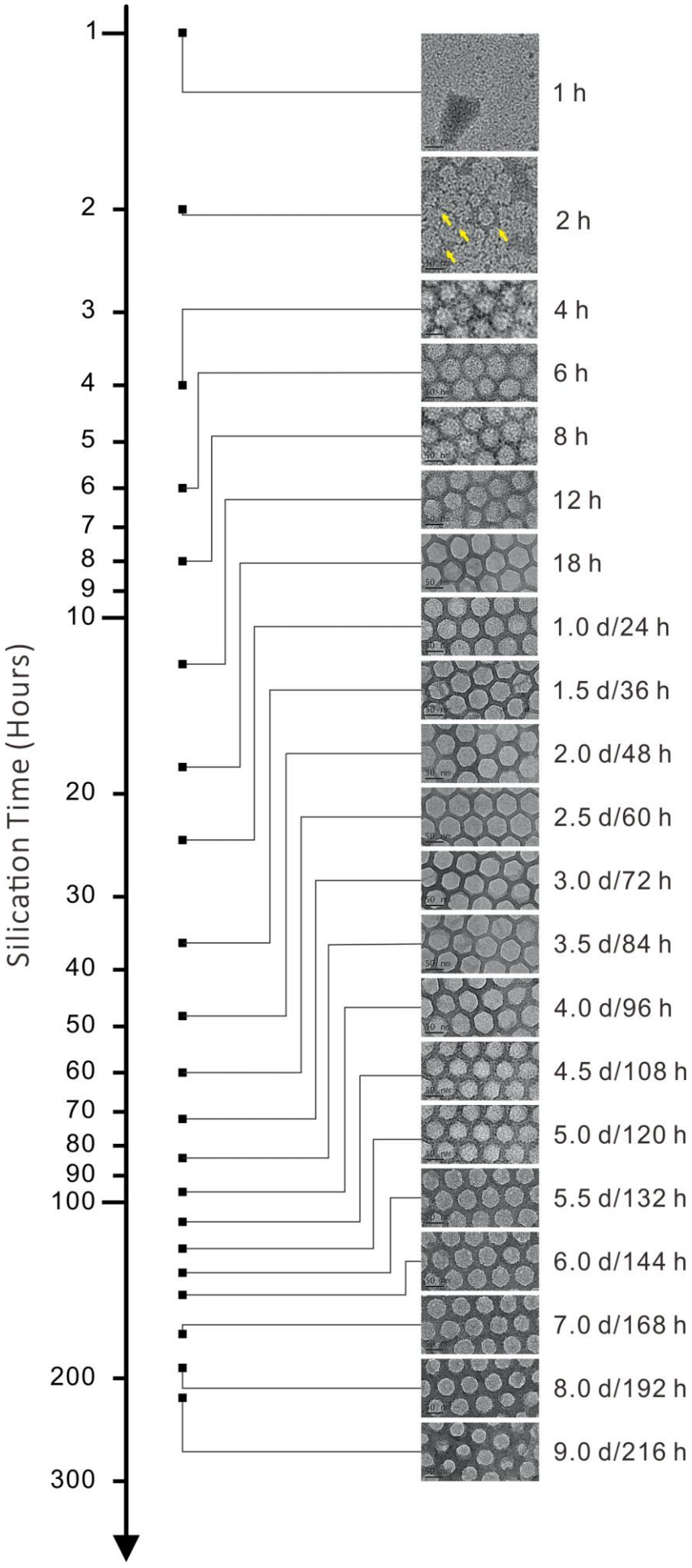

Figure 45 | Growth tracking of DOS honeycomb structure. TEM images of the silicification process of a DOS honeycomb from the initial reaction day 0 to day 9. At 2 h, the pre-hydrolyzing cluster attached onto the DNA origami resulting in visible hexagonal frameworks. The silica layer became gradually thicker and thicker during the first 9 days. On day 9, irregular growth occurred, the outer layer of newly formed silica was rougher compared to the samples reacted for a shorter period.

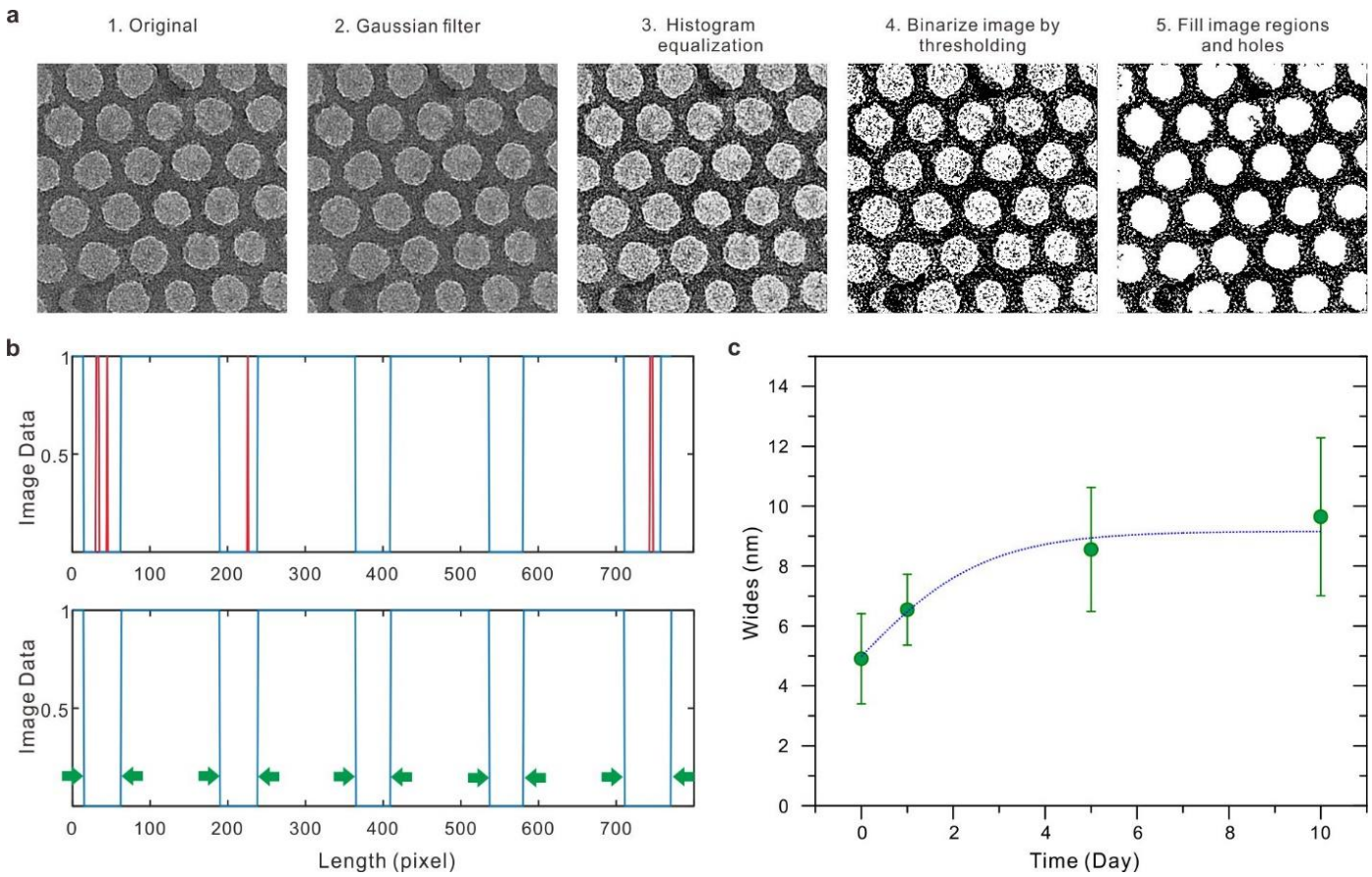

Figure 46 | Statistical analysis of the edge thickness of the DOS honeycomb. a. Typical image processing procedure. The aim is to exclude background noise and acquire an adequate number of samples. **b.** The derived edge thickness before and after the thresholding treatment. The red lines indicate the presence of impurities inside of the honeycomb holes. The distance between the two adjacent blue lines represents a single edge thickness. **c.** Statistics acquired from samples reacted for 0 (negatively stained DNA sample), 1, 5 and 10 days. The edge thickness almost reached its summit after 5 days of silicification, with an average width of ~ 9.0 nm.

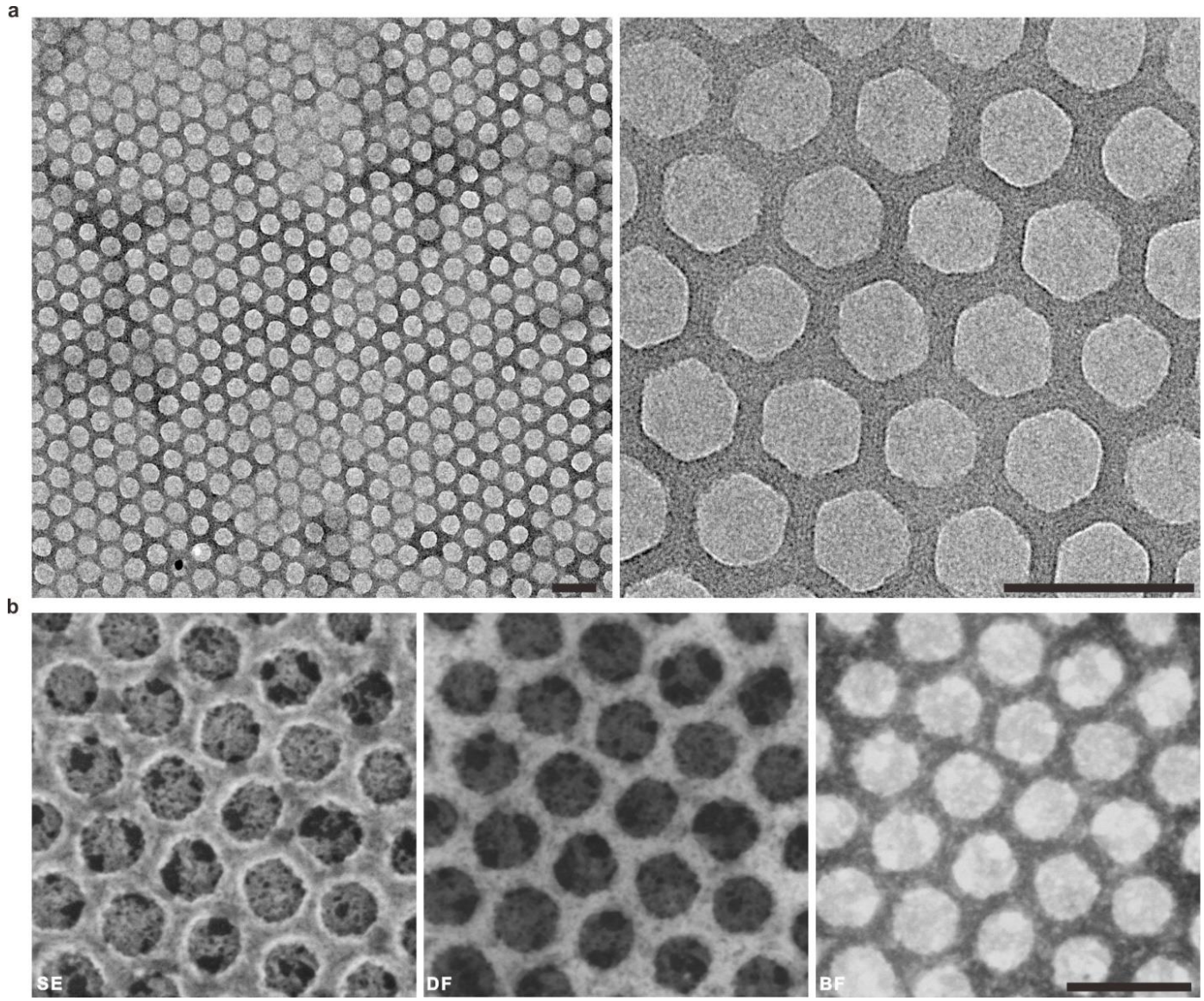

Figure 47 | A DOS honeycomb after 2 days of silicification. a. TEM zoomed out/in images show the homogenous honeycomb pattern at both a micrometer and a nanometer scale. **b.** SE, DF and BF-STEM images show the surface and inner details of the DOS honeycomb sample. Scale bars, 100 nm.

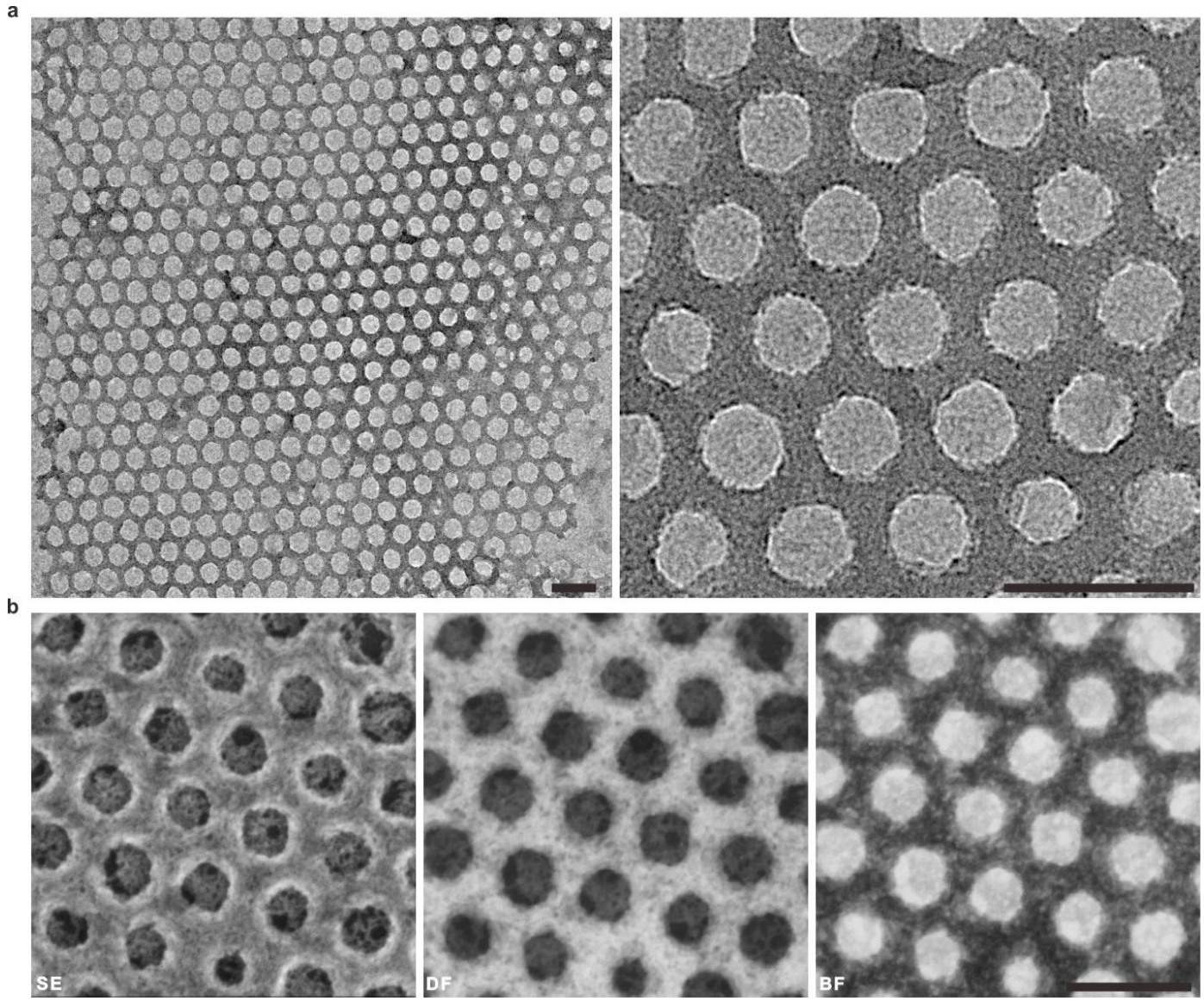

Figure 48 | A DOS honeycomb after 5 days of silicification. a. TEM zoomed out/in images show the homogenous honeycomb pattern at both a micrometer and a nanometer scale. There were obvious increases to the edge thicknesses as compared to the 1- and 2-day samples. **b.** SE, DF and BF-STEM images show the surface and inner details of the honeycomb DOS sample. Scale bars, 100 nm.

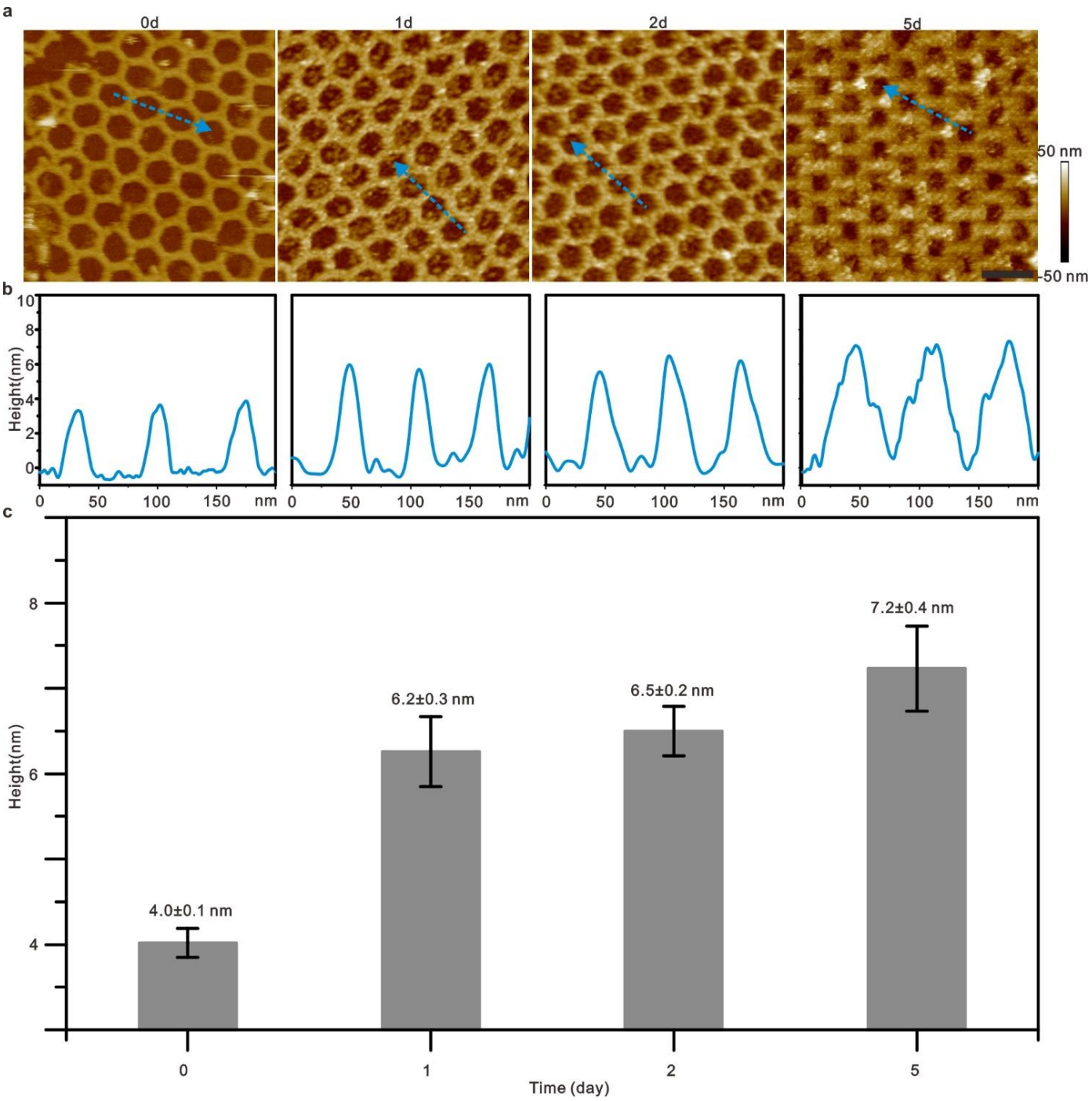

Figure 49 | AFM characterization of the DOS honeycomb after 0, 1, 2, and 5 days of silicification. a. AFM images and height diagrams of DOS honeycomb structures at different silicification periods. **b.** The corresponding height statistics (N = 20). Scale bars, 100 nm.

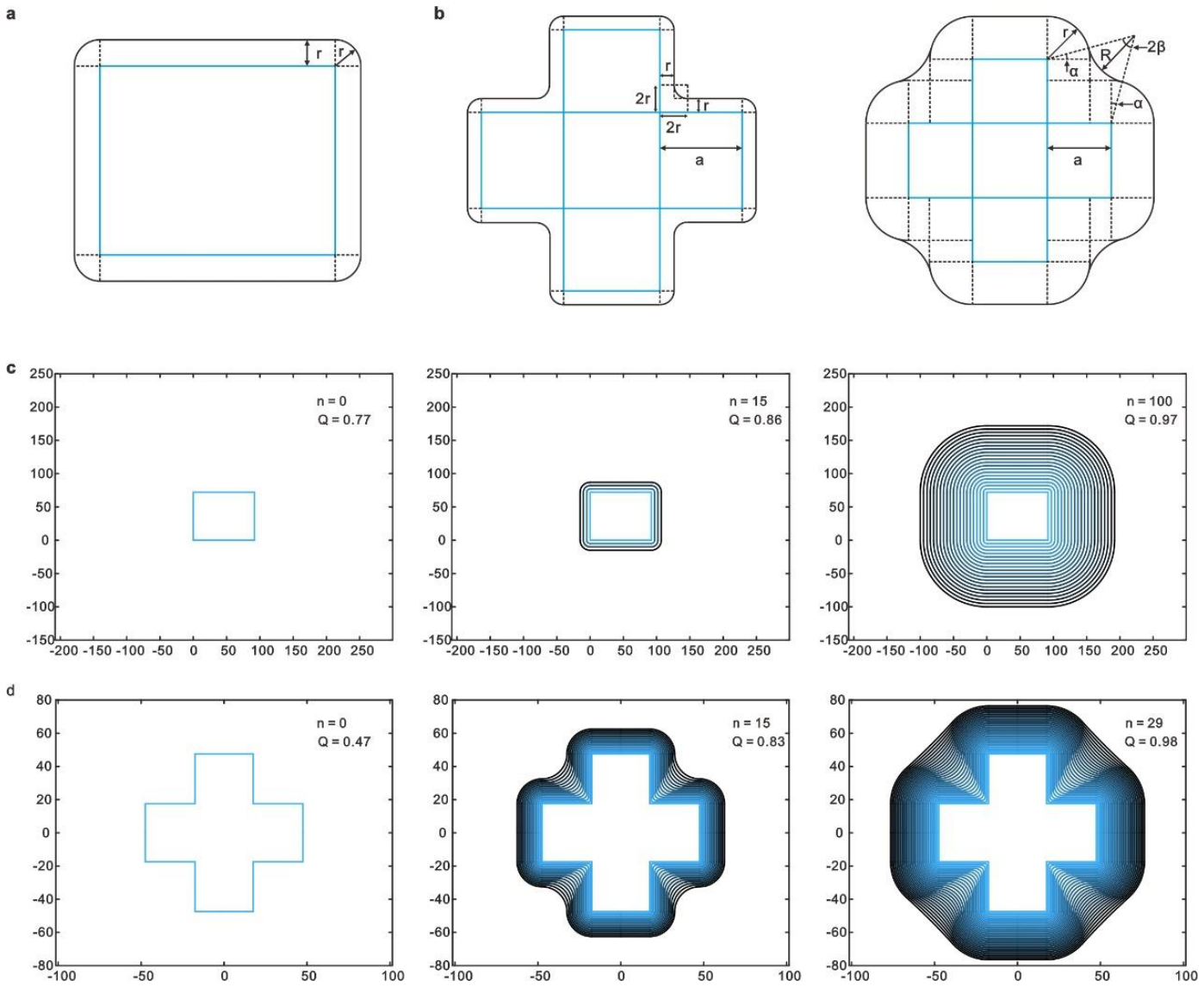

Figure 50 | An isoperimetric inequality simulation for the tunability of silica shells for typical 2D DOS structures. a and **b**. Simulation parameters for square and cross origami. These two shapes represent the typical convex polygon and concave polygon shapes. The thickness of the newly grown layer was *r*. The situation for the convex polygon was simple, while the situation for the concave polygon was more complicated. When *r* < *a*/2, the situation was similar to that of the convex polygon, when *a*/2 < *r* < *a*, and more parameters were introduced, where $= (2r \times 45)/a - 45$ $R = (\sqrt{2}/2\ a)/(\cos(45° + \alpha)) - r,$ $2\beta = 2 \times (45 - \alpha)$. **c** and **d**. The isoperimetric quotient $Q = 4\pi A/L$ ranges from 0 (an infinitely elongated polygon) to 1 (a perfect circle). When *n* was set to 1 nm, (The original origamis were drawn to the real life-sized scale) and we could observe a 100 nm thick layer on the 2D square that resulted in a quasi-circle with *Q* = 0.97, while for a 2D cross, only a 29 nm thick layer could change *Q* from 0.47 to 0.98. The simulations here indirectly proved that the tunability of thickness is achievable, but limited in complex DNA origami. This implies that the over grow of a silica layer will eventually result in the loss of the initial geometric information encoded by the DNA origami. All of the units for the un-labeled axis are in nm. The unit of ***n*** is nm. We figured out from the graph that the 100 nm thick growth of the silica resulted in a chamfering square.

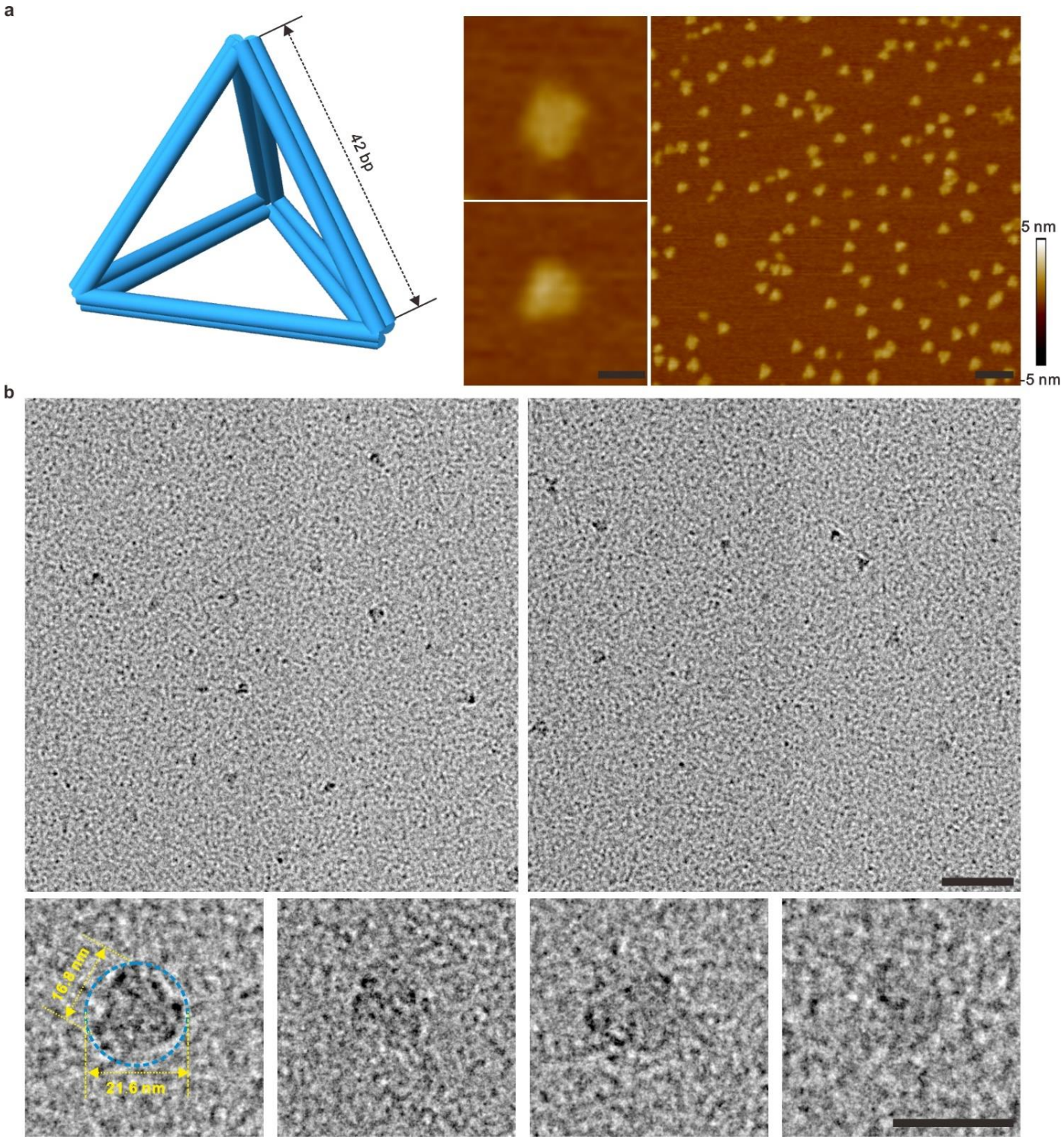

Figure 51 | Characterization of tetrahedron DNA frameworks（16 nm in side length）and corresponding DOS tetrahedron. a. AFM characterization of tetrahedron DNA frameworks in air mode. **b.** TEM characterization of DOS tetrahedron. The side length and circumscribed circular diameter of a DOS tetrahedron was 16.8 nm and 21.6 nm, respectively. The cavity of the DOS tetrahedron was difficult to visualize because the silica growth towards the interior of the circle ended up filling the cavity. Scale bars, zoomed in, 25 nm, and zoomed out, 100 nm.

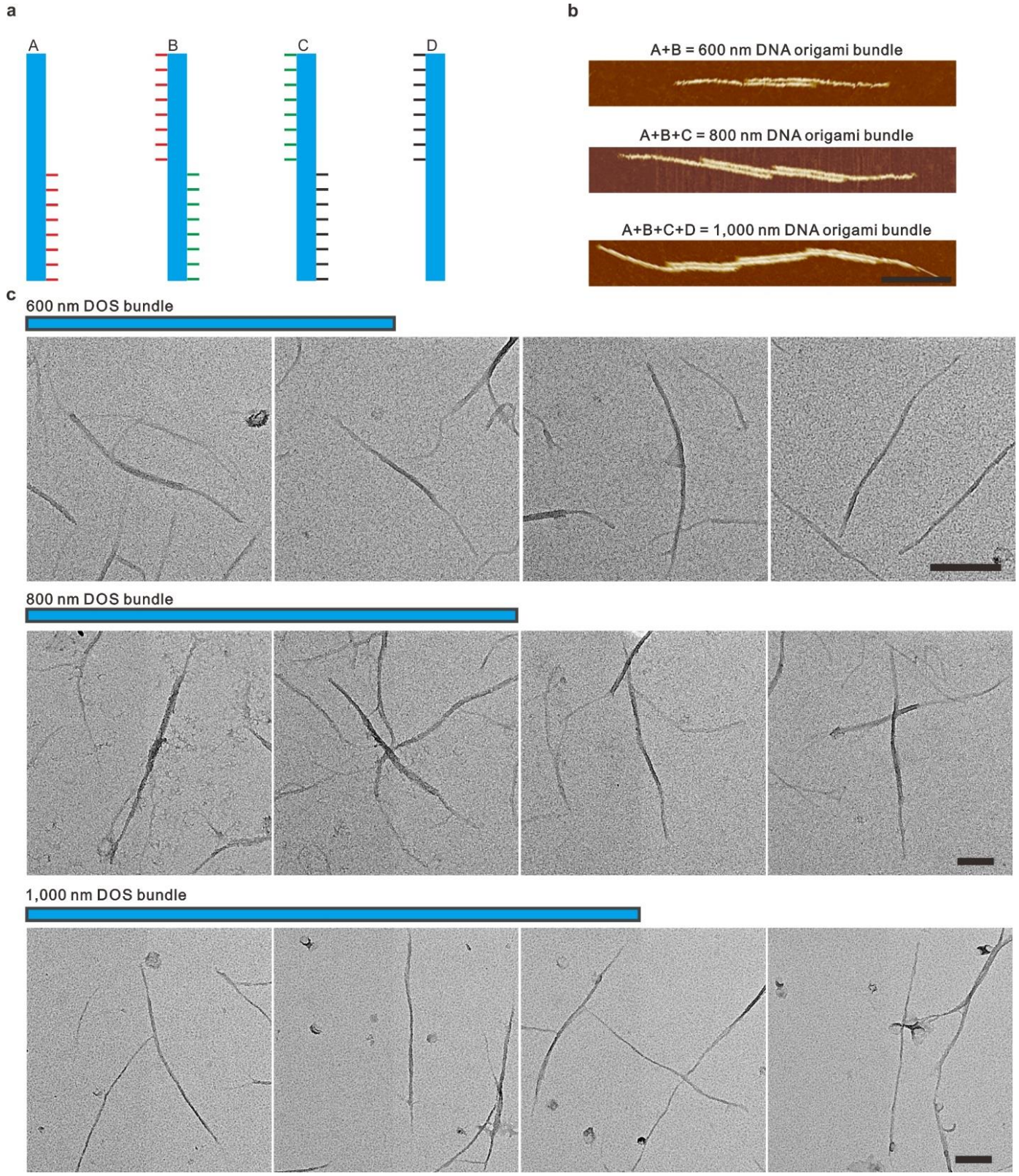

Figure 52 | Characterization of 6-helix DNA origami bundles and corresponding DOS bundles of different lengths. a. Schematic illustration for the assembling of various lengths of 6-helix DNA origami bundles. **b.** AFM characterization of DNA origami bundles of different lengths. **c.** TEM characterization of a 600 nm DOS bundle, a 800 nm DOS bundle, and a 1,000 nm DOS bundle. Scale bars, 200 nm.

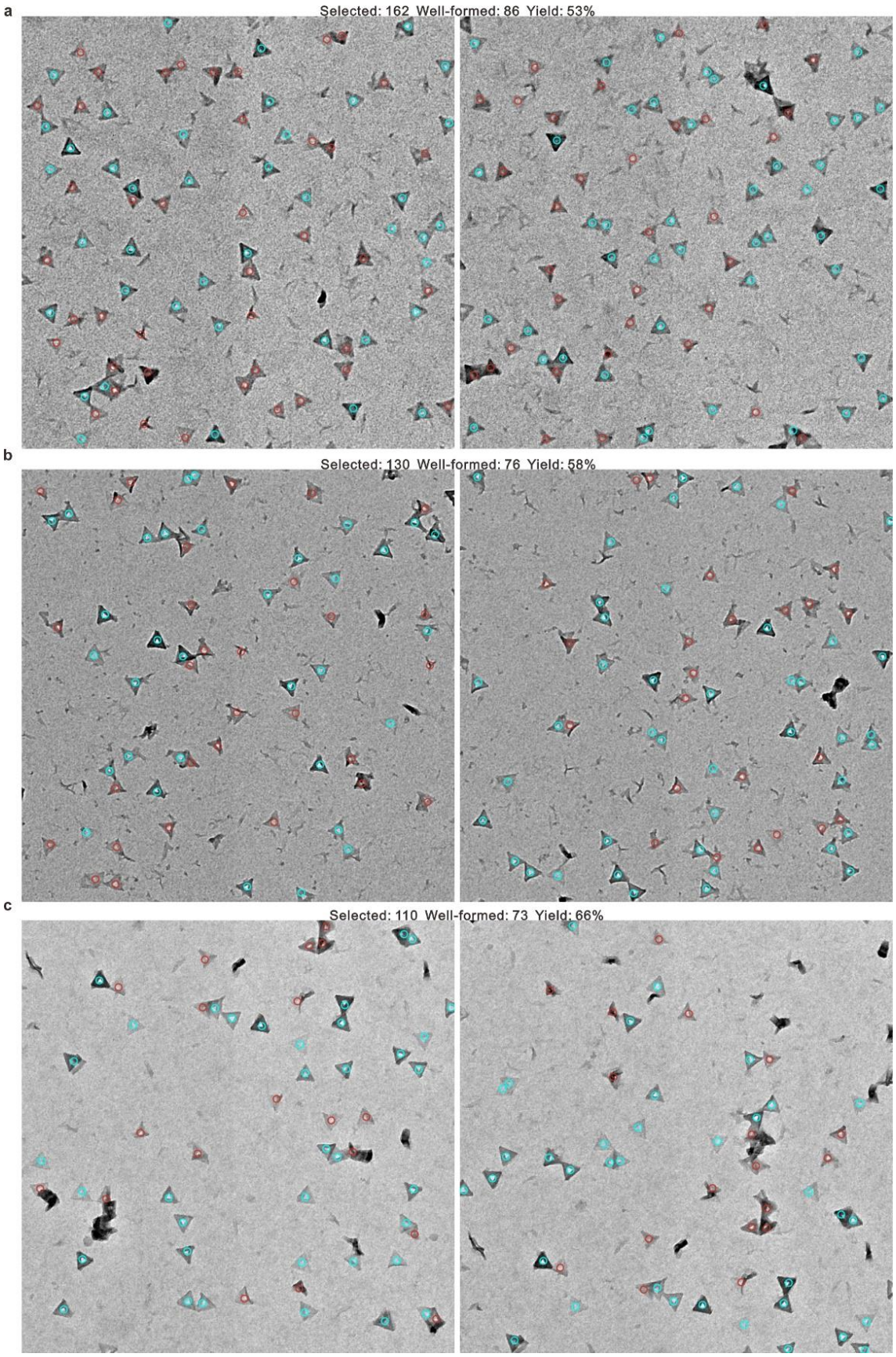

Figure 53 | Exemplary TEM images of DOS triangle after a. 1 day, b. 2 days, c. 5 days reactions with yield calculation (2.7 µm × 2.7 µm). The DOS triangles marked with red circles are “ill-formed” and those marked with green circles are “well-formed.” The yield was calculated as the ratio between the number of “well-formed” DOS triangles and the total number of selected shapes. As the silica thickness increased, the yield of well-formed DOS triangles without any distortion increased slightly (53.1% to 58.5% to 66.4%).

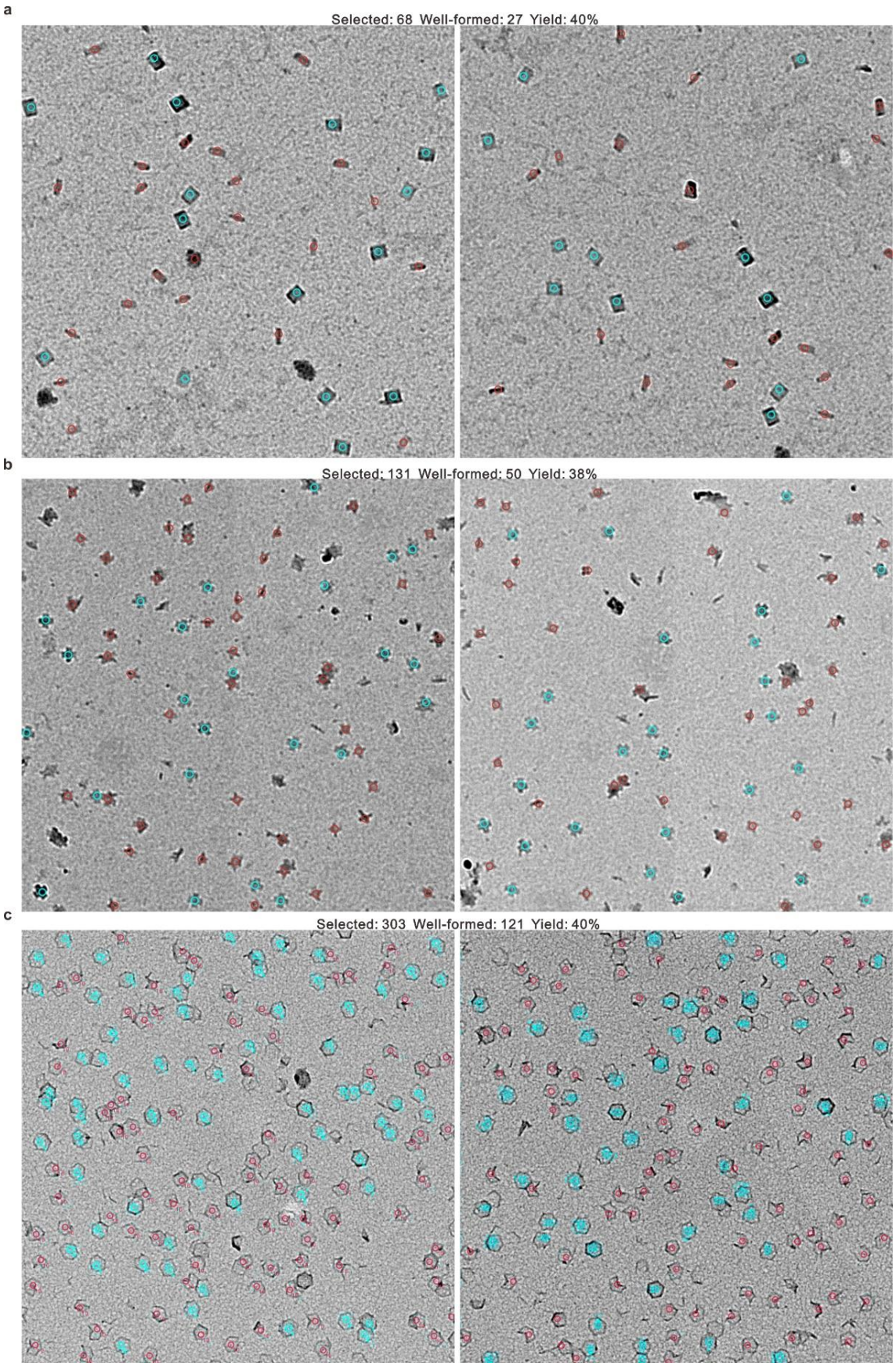

Figure 54 | Exemplary TEM images of a. rectangle, b. cross and c. hierarchical pore DOS nanostructures after 2 days of reaction with yield calculation (2.7 µm × 2.7 µm). The DOS nanostructures marked with red circles are “ill-formed” and those marked with green circles are “well-formed.” The yield was calculated as the ratio between the number of “well-formed” DOS nanostructures and the total number of selected shapes.

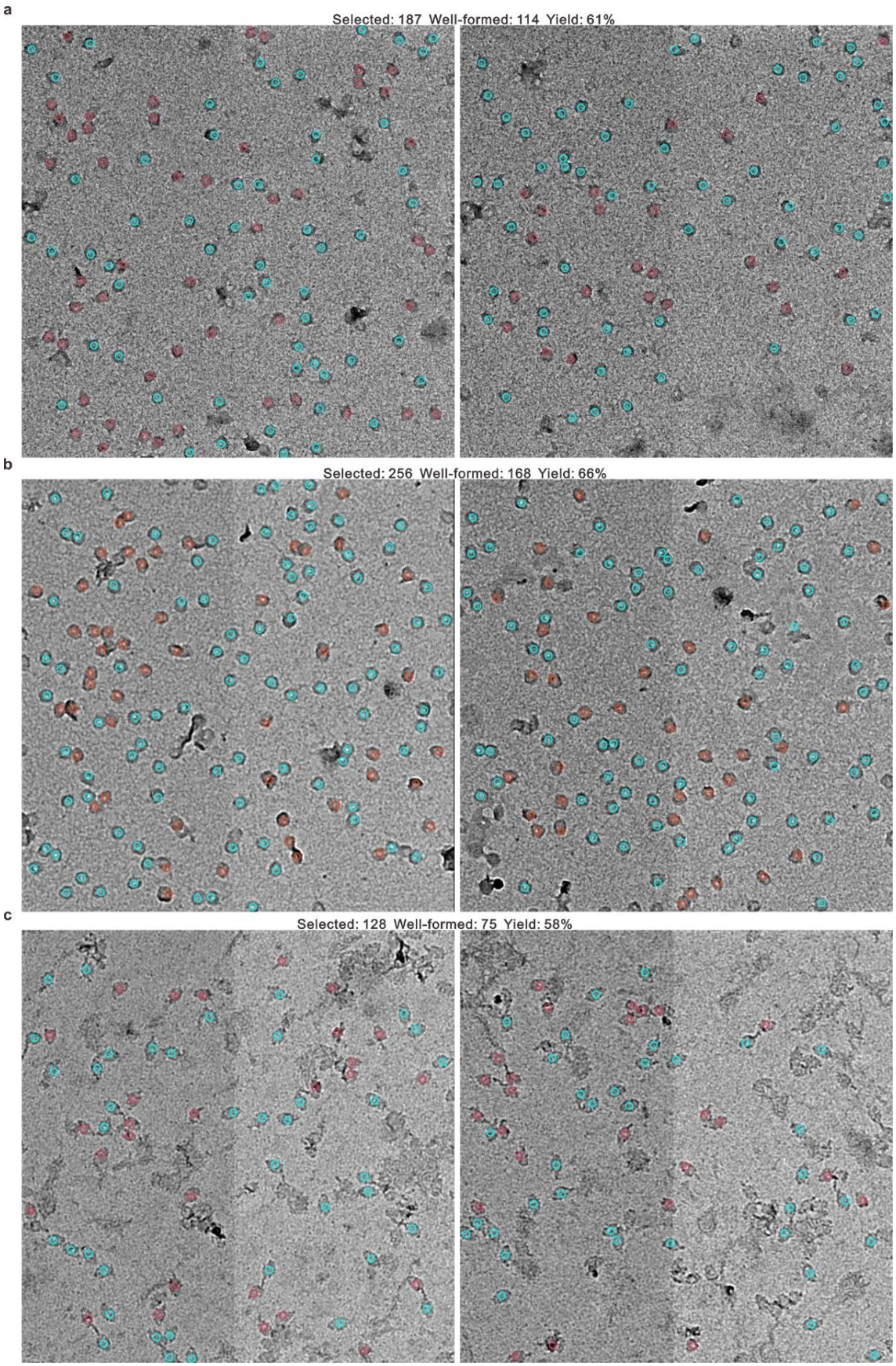

Figure 55 | Exemplary TEM images of a. hemisphere, b. toroid and c. ellipsoid DOS nanostructures after 2 days of reaction with yield calculation (2.7 µm × 2.7 µm). The DOS nanostructures marked with red circles are “ill-formed” and those marked with green circles are “well-formed.” The yield was calculated as the ratio between the number of “well-formed” DOS nanostructures and the total number of selected shapes.

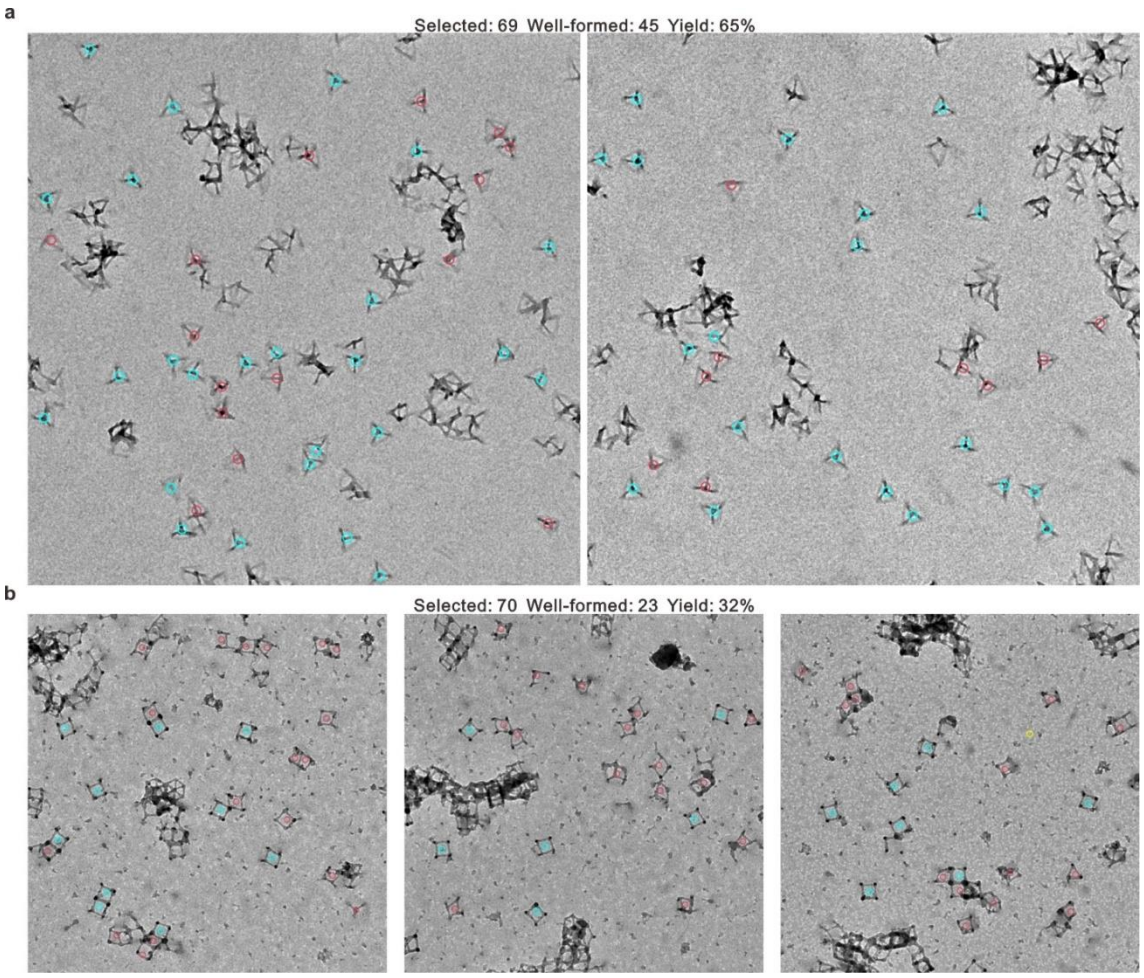

Figure 56 | Exemplary TEM images of a. tetrahedron and b. cube DOS nanostructures with yield calculation (2.7 µm × 2.7 µm). The DOS nanostructures marked with red circles are “ill-formed” and those marked with green circles are “well-formed without any tilt.” The aggregates that had issues because of the DNA origami themselves were not included in the selection of the particles. The yield was calculated as the ratio between the number of “well-formed” DOS nanostructures and the total number of selected shapes.

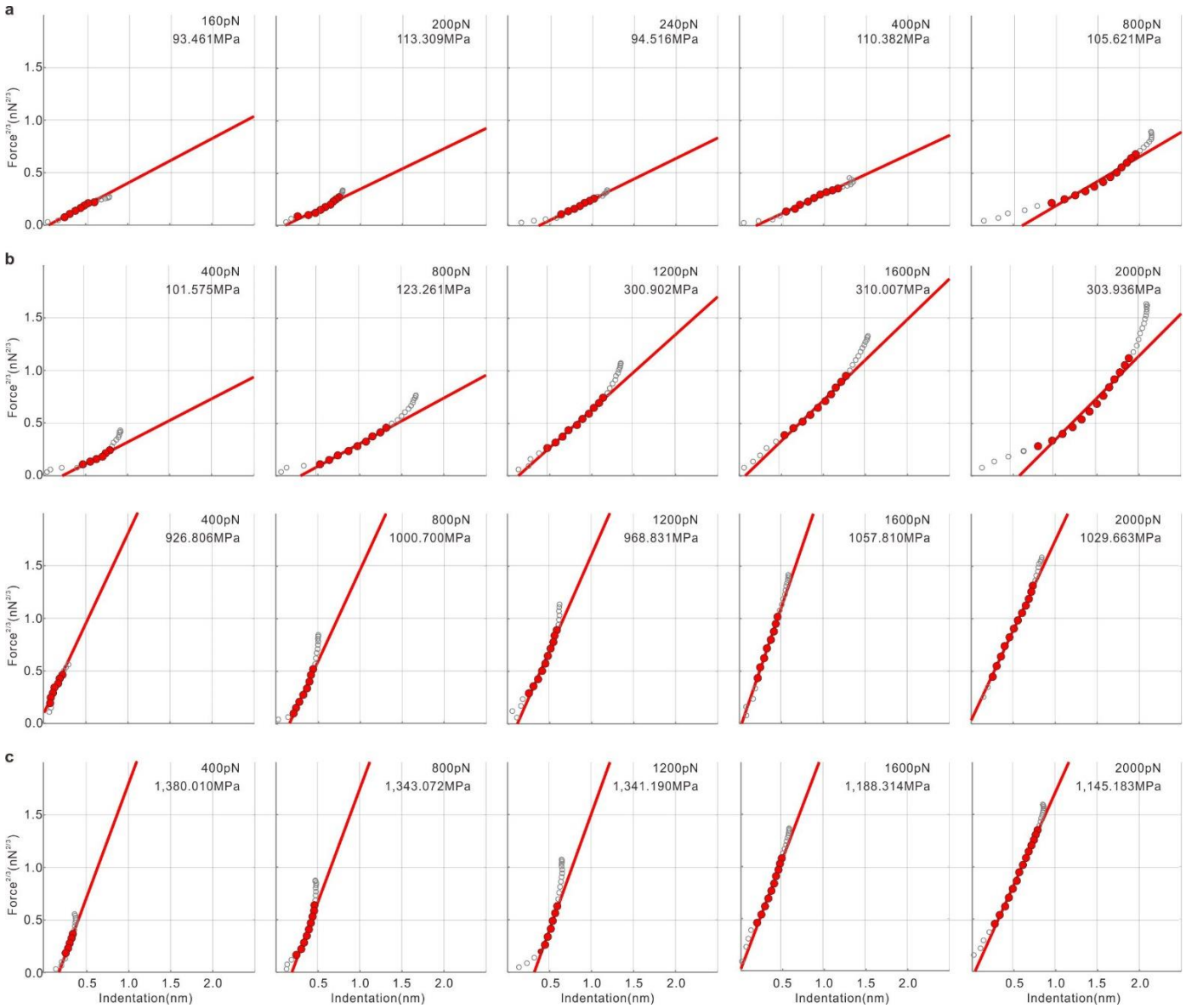

Figure 57 | Exemplary data of Force$^{2/3}$-Indentation curves from the MSEC model. From equation (4) in the materials and methods section, we know that the Force$^{2/3}$ is proportional to the indentation during the second step of the experiment and that the slope is proportional to the *E*-modulus. **a.** The Force$^{2/3}$-Indentation curves of the DNA framework. The indentation forces were 160, 200, 240, 400 and 800 pN. The average *E*-modulus was around 100 MPa, which represents the nanomechanical properties of the molecular DNA. **b.** The Force$^{2/3}$-Indentation curves for the 1-day sample. The indentation forces were 400, 800, 1,200, 1,600 and 2,000 pN. It is supposed that after 1 day of silicification, that the thin silica layer could not completely cover the DNA framework surface. Therefore, bare areas of DNA exist, which accounts for the low modulus ~ 100 MPa (intact DNA, under 400 and 800 pN) and ~ 300 MPa (over compressed DNA, 1,200, 1,600 and 2,000 pN). **c.** Force$^{2/3}$-Indentation curves from a 5-day sample. The maximal indentation forces were 400, 800, 1,200, 1,600 and 2,000 pN. The average *E*-modulus was about 1,200 to 1,400 MPa, which was representative of the DOS nanostructure.

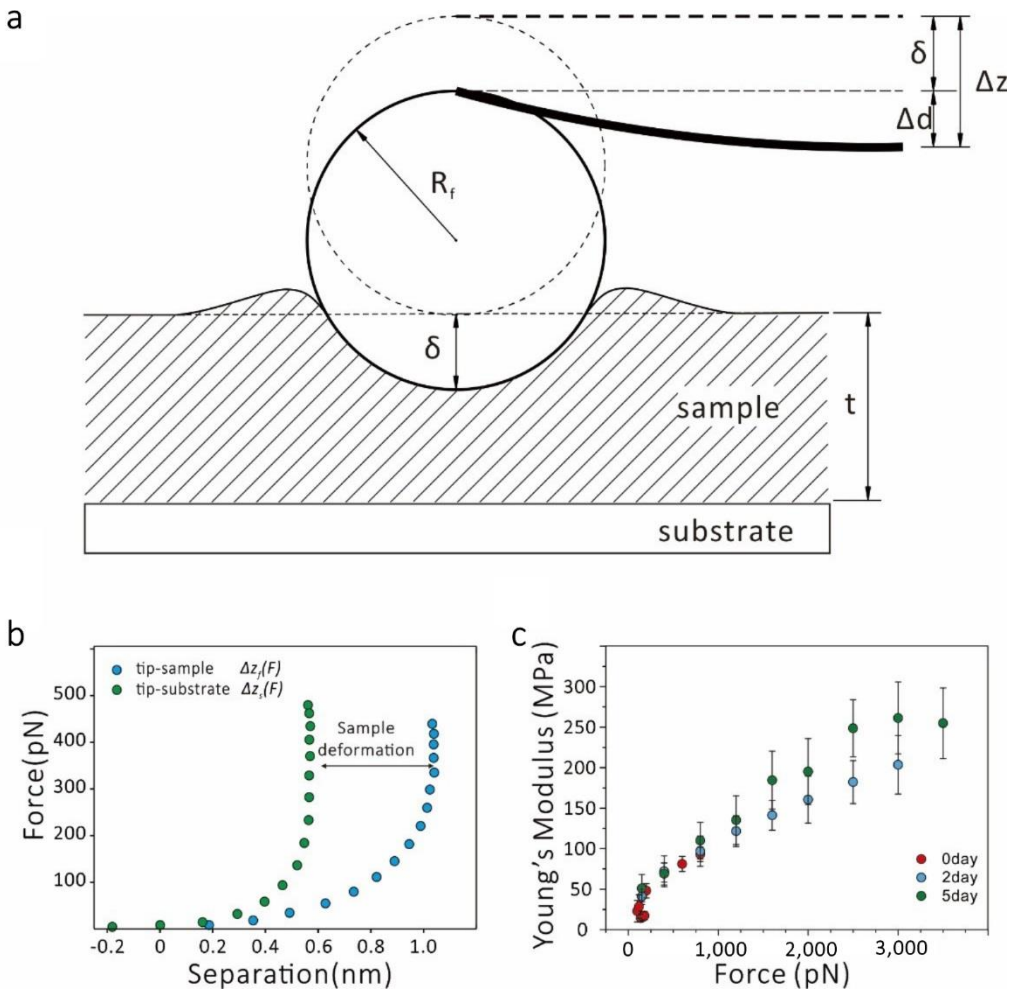

Figure 58 | Mechanical properties obtained from AFM. **a.** Schematic illustration of the indentation experiments. **b.** Force-separation curve of the tip-sample and the tip-substrate interactions. Force (F) = indentation force (F_i) - adhesive force (F_{ad}). Separation means tip & cantilever system z-direction separation (Δz). **c.** E-Modulus obtained by an unmodified DMT model.

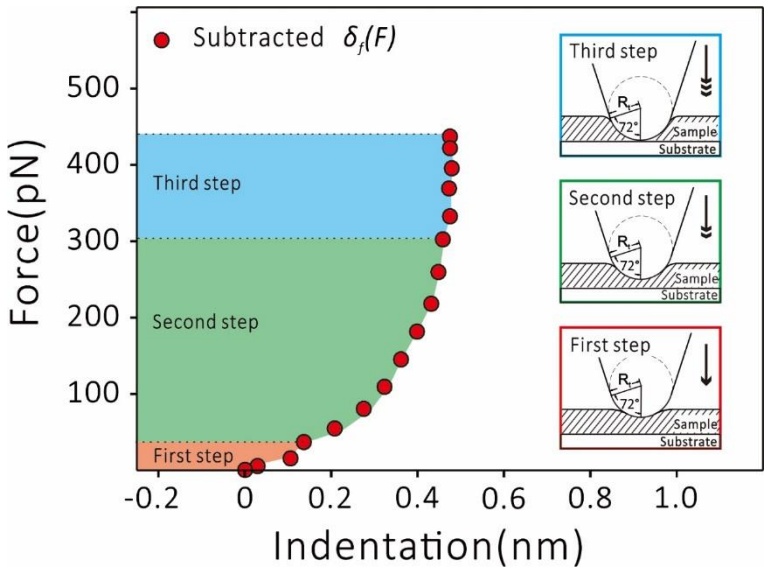

Figure 59 | Three steps of the indentation process. Force-indentation curve obtained from a tip-sample FS curve that was subtracted by a tip-substrate FS curve. Three steps occurred during the process: 1st step, initial contacting step, the force on the tip is unbalance. 2nd elastic deformation step, from ~ 10 % of maximal forces to ~ 70 %. 3rd inelastic deformation step.

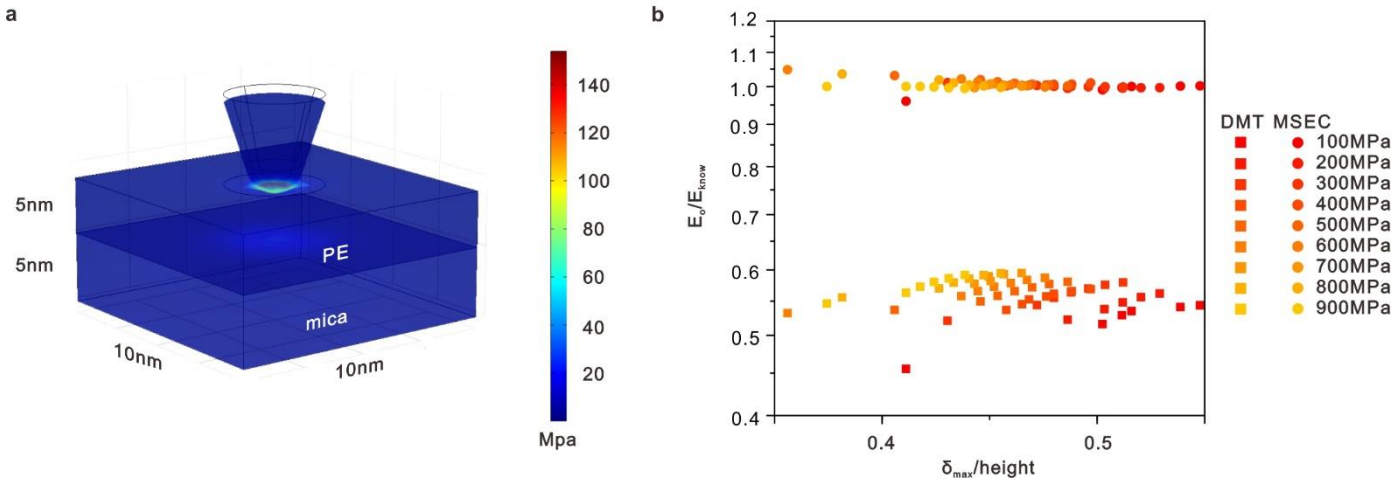

Figure 60 | COMSOL verification of MSEC. a. A COMSOL model of the AFM mechanical simulation. **b.** The calculated *E*-modulus using a DMT model was sample indentation and force dependent, showed an obvious deviation from the E_{know}. Conversely, when the MSEC was applied, the calculated E values were indentation independent and matched well with the known modulus of the presupposed PE film.

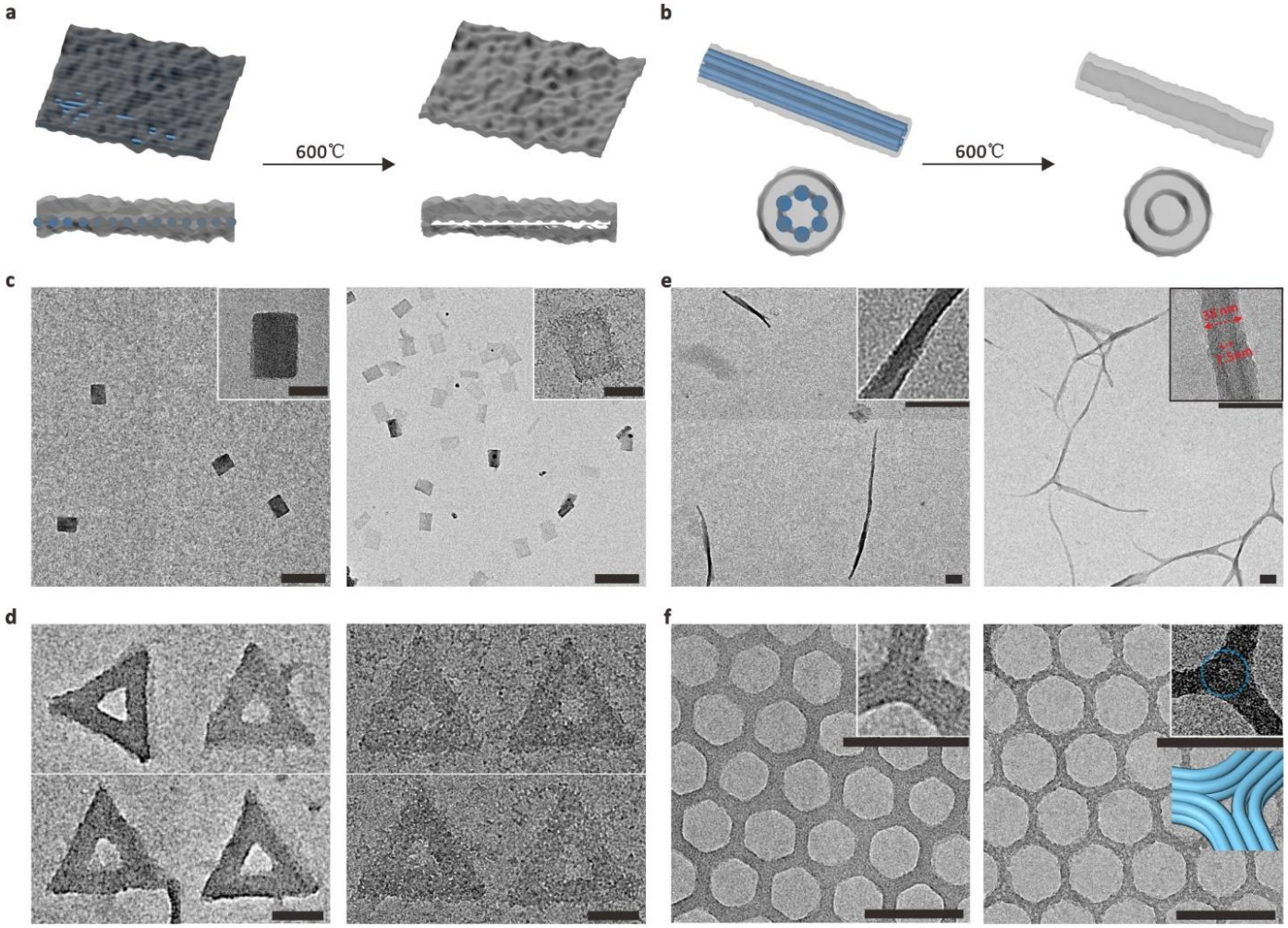

Figure 61 | TEM characterization of various DOS structures after calcination at 600 °C. a, c and d. After calcination, single layered DOS structures clearly showed a lower contrast, possibly due to the removal of the DNA origami. Many pores on the single layered DOS structures revealed that the silicification did not happen over the entire area of the DNA-origami. However, dsDNA channels could not be seen in the single layered DOS structures after calcination. This proved that the TMAPS and TEOS could not grow inside of the gaps between the dsDNA strands in the origami, which was also consistent with the MD simulation results. **b, e and f.** The 6-helix DNA-origami channel was clear in 6-helix DOS structure after calcination. d = ~ 7.5 nm corresponds to the diameter of the six-helix DNA-origami structures. For a honeycomb structure, we discovered an interesting phenomenon in regards to the channels before and after calcination. Before calcination, periodic channels could be dimly seen. However, the channels disappeared after calcination. Thus, the channels before calcination, we believe, should be the gaps between the dsDNA strands in the origami. The reason the channels could be seen prior to calcination may be due to the high contrast of the double-layered DNA origami, which was obvious in TEM images of negatively stained multi-layered DNA origami structures. Scale bars, zoomed in, 50 nm, and zoomed out, 100 nm.

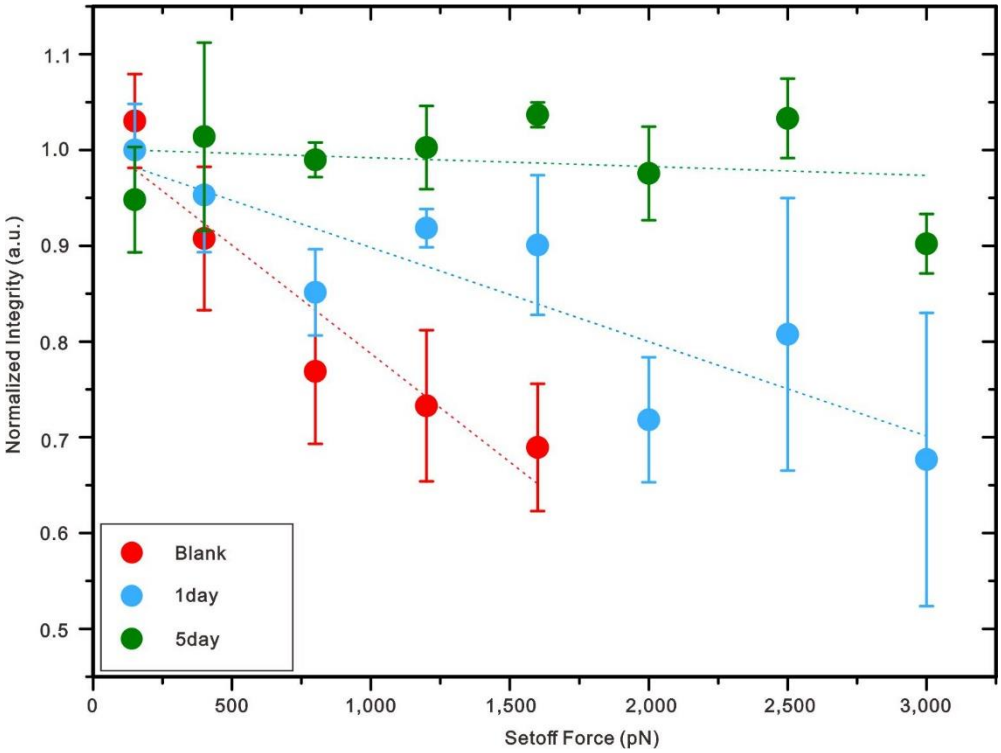

Figure 62 | Destructive AFM tip forces on the integrity statistics of a blank DNA origami and a DOS nanostructure that was reacted for 1 and 5 days. Based on the *E*-modulus data, it was expected that the compression strength of the DOS nanostructures would be greatly enhanced. We applied increasing AFM tip forces to test the mechanical property of both the pure DNA origami and the triangular shaped DOS. The derived *E*-modulus agreed well with the AFM data for the sample integrities under different setoff forces. The pure DNA origami structures were heavily damaged under 1,600 pN. With larger forces up to 3,000 pN, the height signal was not stable and thus could not be used with the rest of the statistical results. On the contrary, the DOS with 5 days of growth was almost intact even under 3,000 pN. The DOS with 1 day of growth was gradually destroyed as the force increased from 150 pN to 3,000 pN.

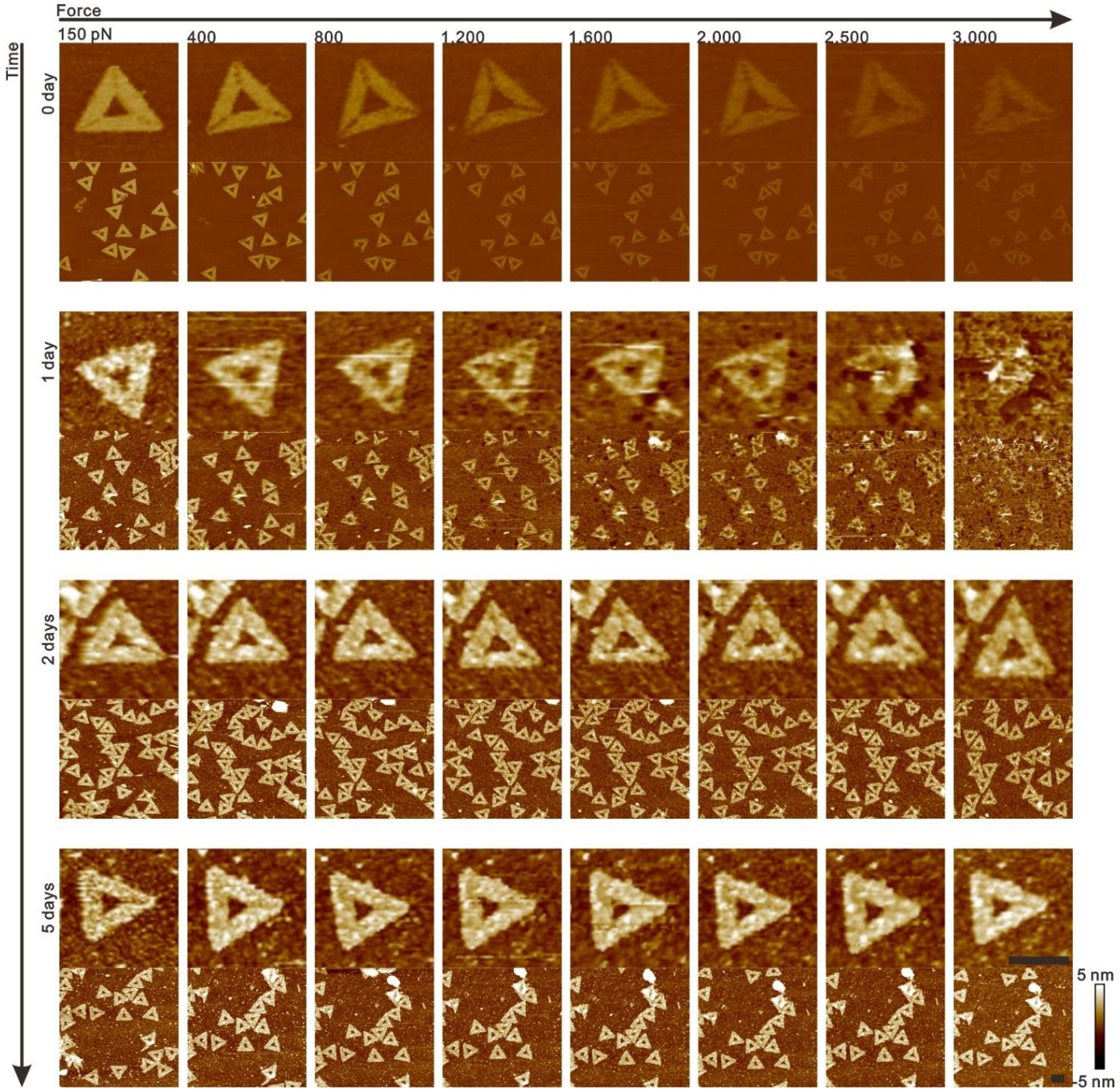

Figure 63 | AFM images show the integrity of triangle DNA-origami framework and DOS triangle, that was reacted for 1, 2 and 5 days, under increasingly applied forces. The heights of the sample decreased dramatically, judging from the height of the scale bar. When the applied forces surpassed 3,000 pN, the DNA framework was almost destroyed. The strengths of all of the DOS triangles were enhanced and were stronger than the DNA framework. Also, the integrity of the DOS triangles were obviously increased with longer silicification time. The statistical data are shown in **Fig. 4b.** Scale bars, 100 nm.

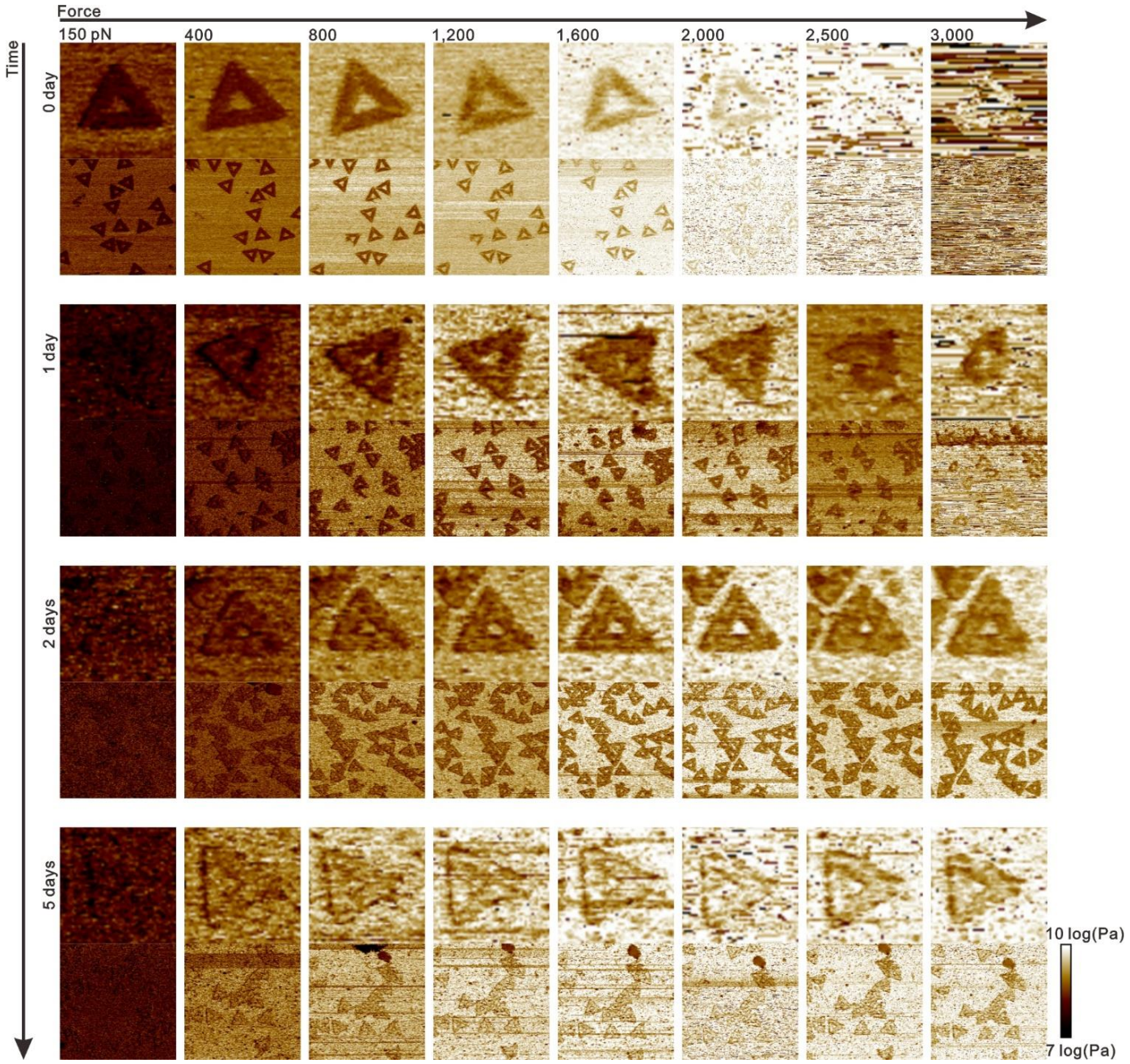

Figure 64 | AFM images show the DMT Modulus of triangle DNA-origami framework and DOS triangle, that was reacted for 1, 2 and 5 days, under increasing applied forces. The modulus of the sample and the mica increased dramatically when the force was increased, judging from the changes in the color of the images. This phenomenon indicated that the modulus was directly measured by the AFM peaking force QNM and that using the DMT modulus was not accurate. We noticed, while using the same force at a different point in time that the modulus of the sample increased slightly. The colors of the sample were becoming lighter with a longer silicification time. However, the colors of the DNA-origami sample were changing quickly, maybe because the DNA sample was being squashed by the tip when the force was higher than 800 pN. This phenomenon demonstrated the enhanced rigidity of the DOS triangle.

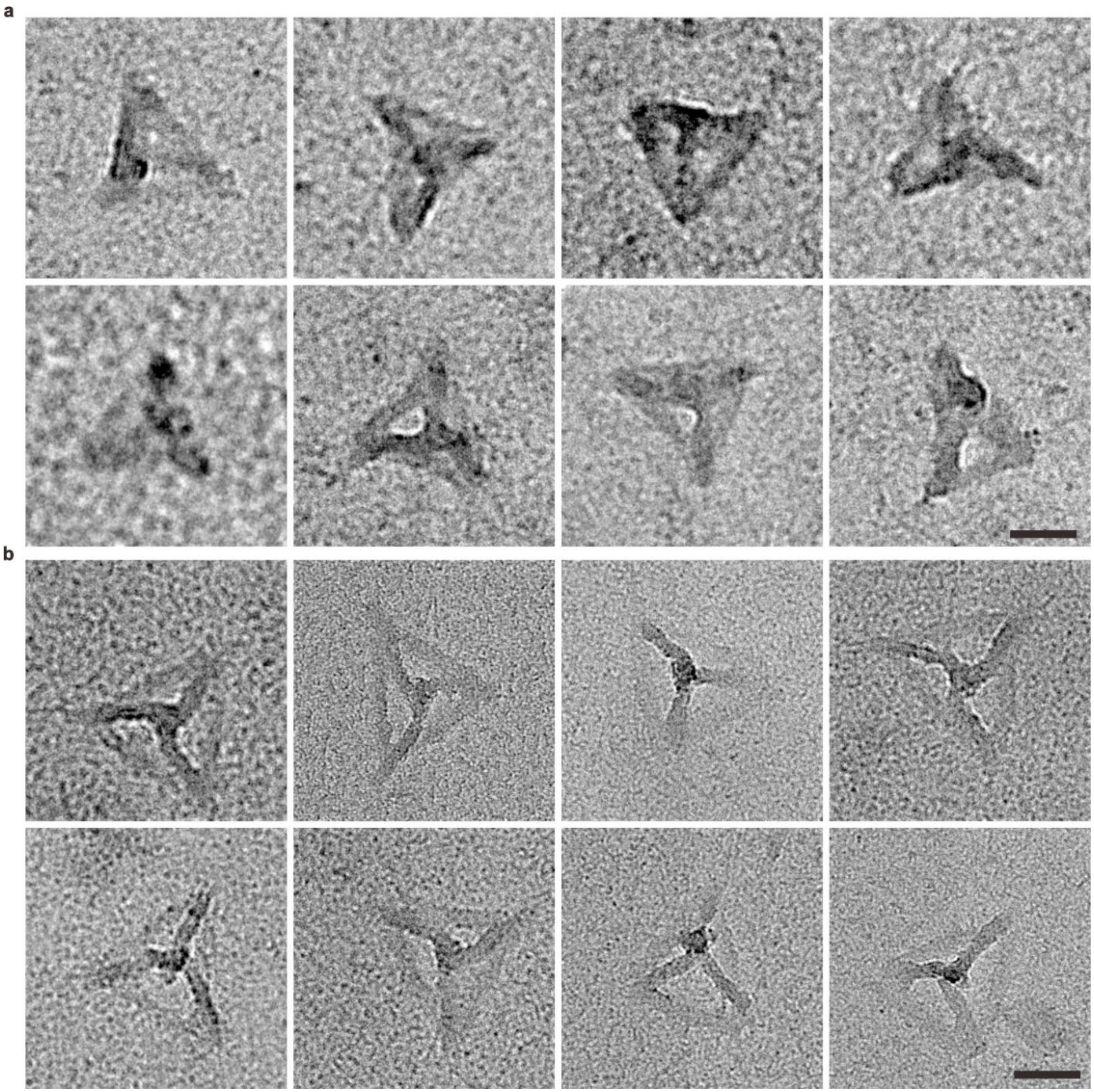

Figure 65 | TEM images of DOS tetrahedron (100 nm in side length) that was reacted for 1 or 2 days. a. The enhancement effect of the silica shell for the 1-day sample was negligible. The 1-day sample was not markedly different from the DNA frame alone. **b.** For the 2-day sample, the silica shell was strong enough to allow the DOS tetrahedron to stand upright on the substrates, with very slight distortion on the standing edges. Scale bars, 50 nm.

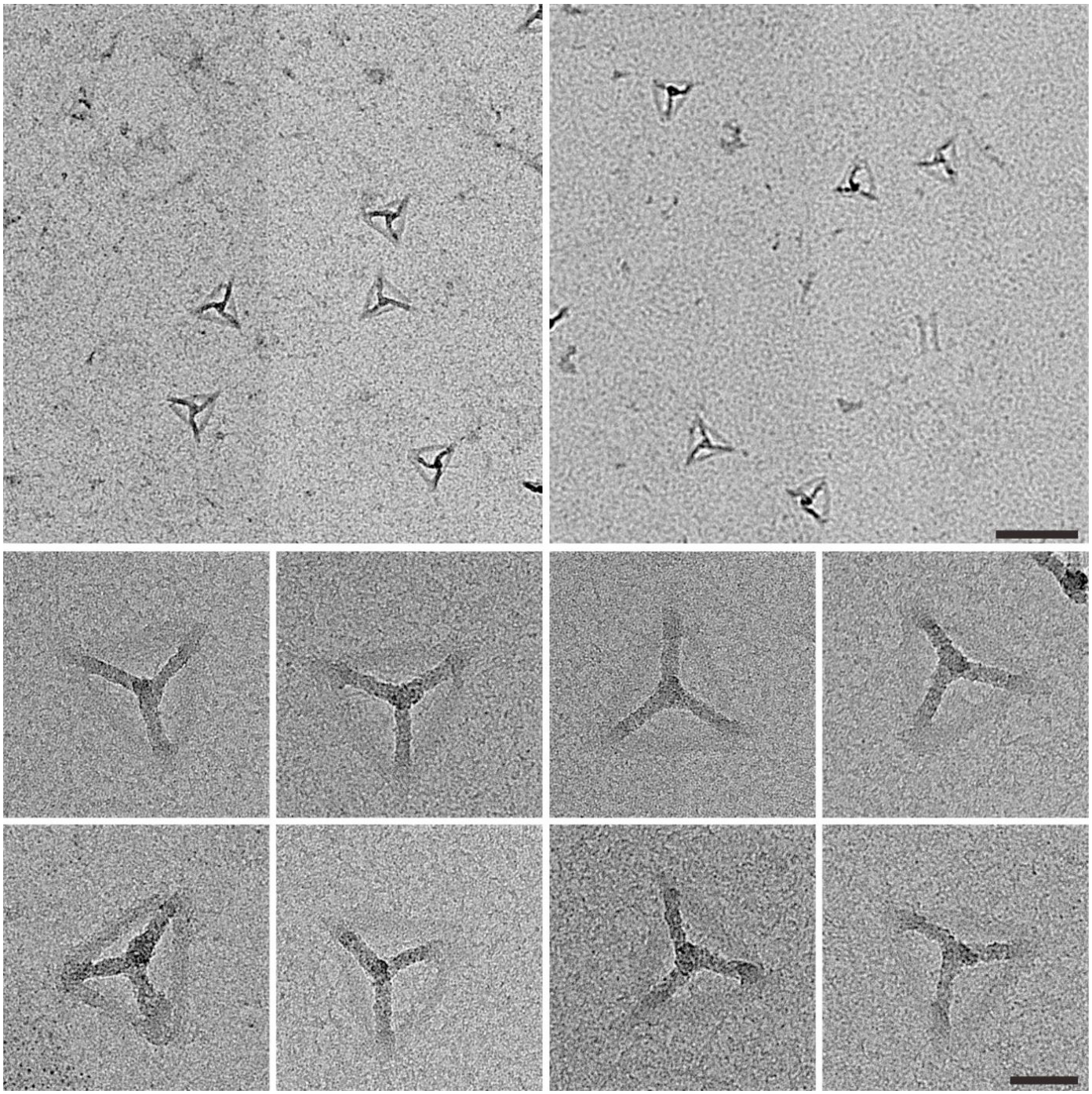

Figure 66 | TEM zoomed out/in images of DOS tetrahedron that was reacted for 5 days. In comparison with the 1- and 2-day samples, most of the 5-day DOS tetrahedron could free-stand on the substrates. The degree of distortion on the edges of the 5-day DOS tetrahedron was less than that of the 1- and 2-day samples. Scale bars, zoomed in, 50 nm, and zoomed out, 200 nm.

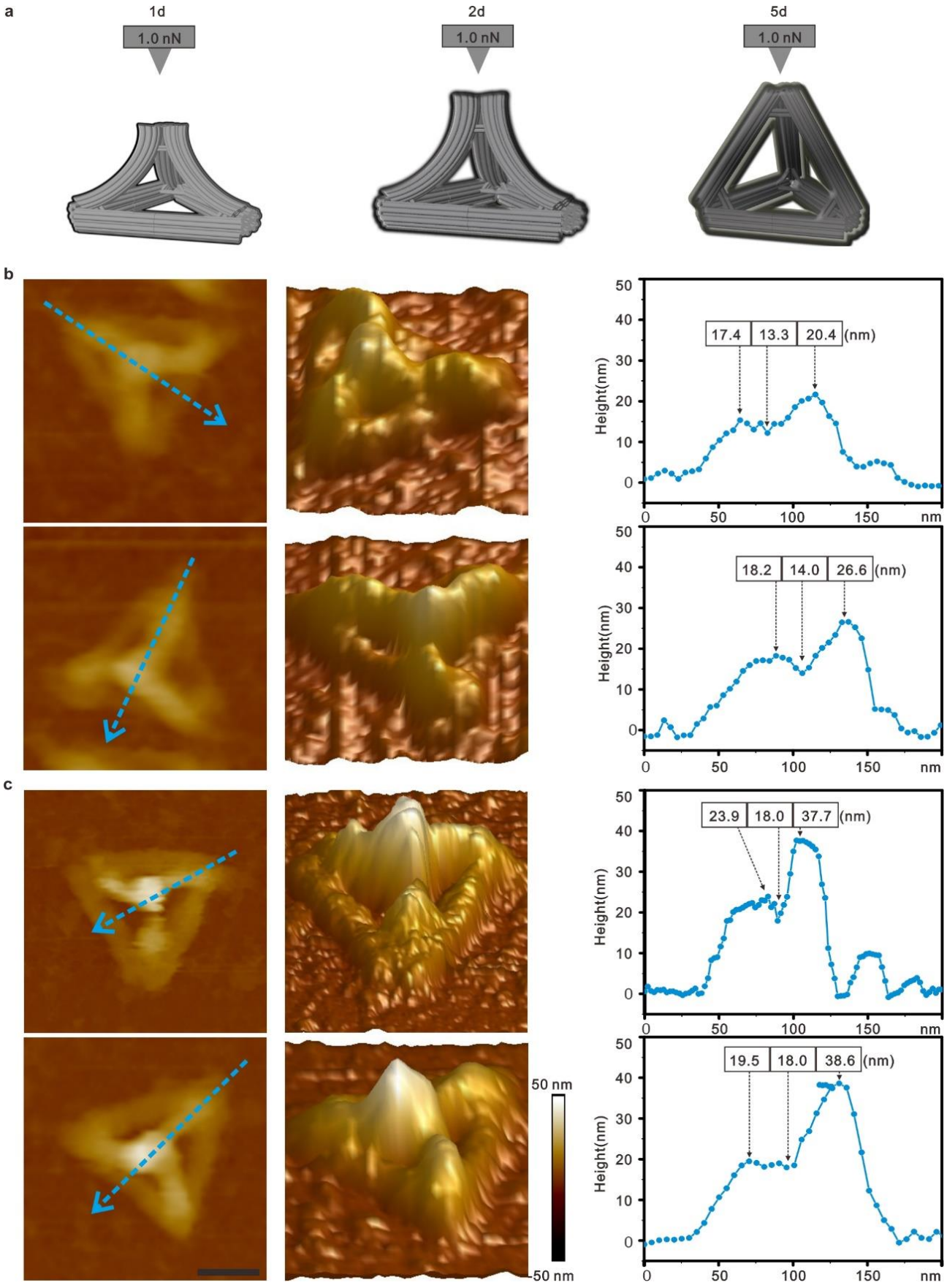

Figure 67 | AFM images of 1- and 2- day DOS tetrahedron under 1.0 nN. a. Schematic illustration for shape changing of DOS tetrahedron under 1.0 nN force. **b.** 1 day**,** and **c.** 2 days. For both the 1- and 2-day samples, the strength of the silica layer was not high enough to support the tetrahedron structure under a 1.0 nN peak force. The typical height diagrams showed that the edges were bent in the middle and formed a 13.0 ~ 18.0 nm step region. Scale bars, 50 nm.

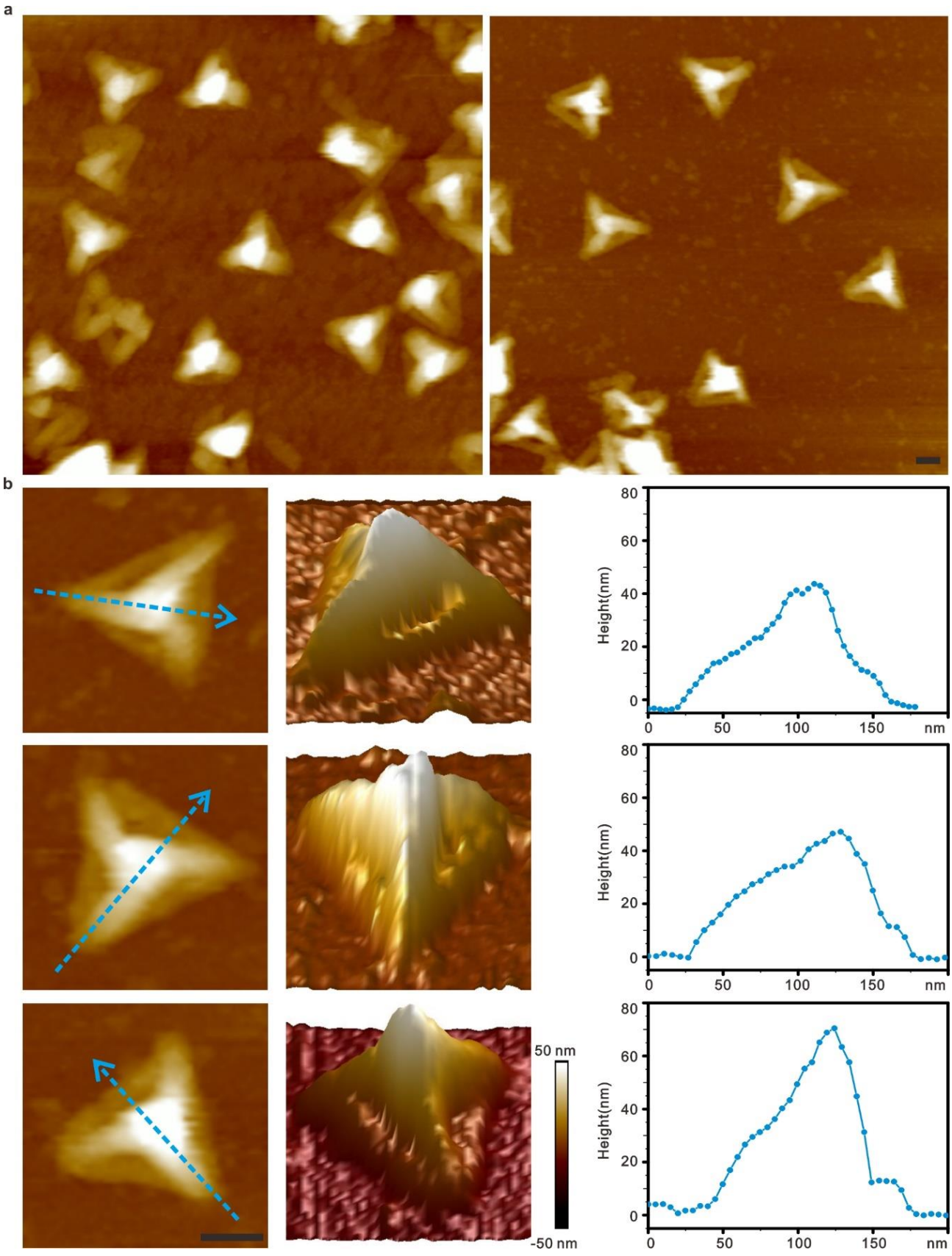

Figure 68 | AFM zoomed out/in images of the 5-day DOS tetrahedron under 1.0 nN. a. The zoomed out images showed homogeneous well-formed DOS tetrahedrons on the mica surface. **b.** Section diagrams showed that the DOS tetrahedrons had standing edges that were almost completely straight. Along with the TEM results, the above data proved that the structural strength of DNA framework had been enhanced. Scale bars, 50 nm.

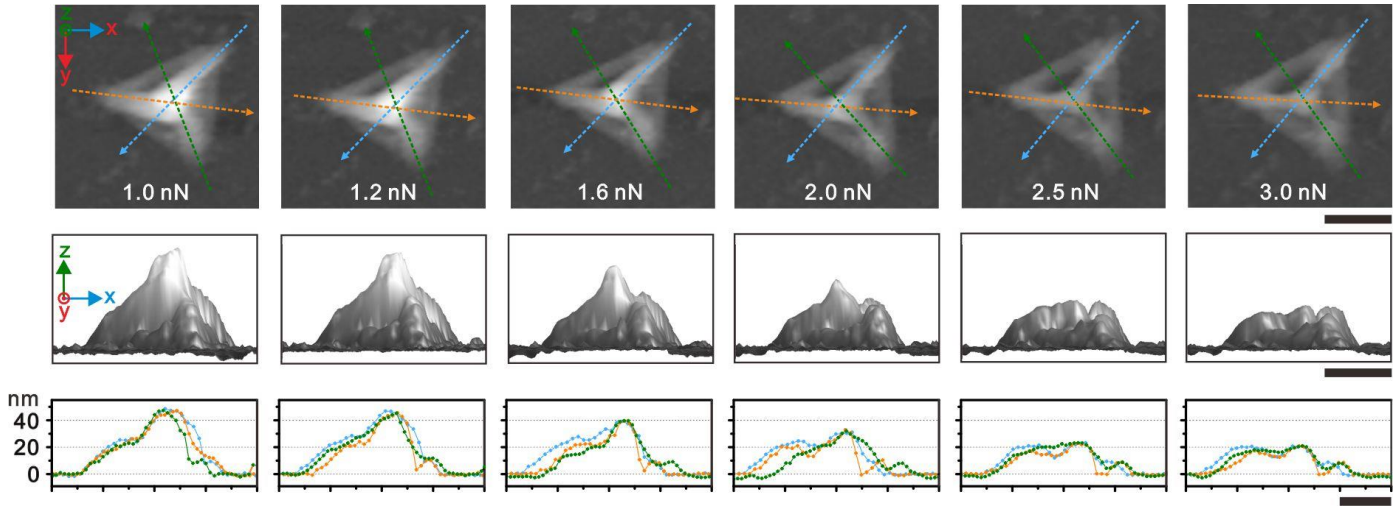

Figure 69 | Height changes during the deformation of a single DOS tetrahedron that was reacted for 5 days, under increasing tip forces, showed changes from 1.0 nN to 3.0 nN. The reported maximum compression force that still maintained the structural integrity of the dsDNA tetrahedron was about 100 pN[47]. In our case, for forces up to 1,000 pN, there was no obvious shape change to the DOS nanostructures. Even for the 3.0 nN load force, the structure was only bent, but not damaged. The larger applied tip forces can lead to a greater bending of the DOS tetrahedrons that had 5 days of growth. The heights along the three edges showed an indentation on each of their center parts, indicating a bending of ~ 10 nm in diameter on the load-bearing edges. Scale bars, 50nm.

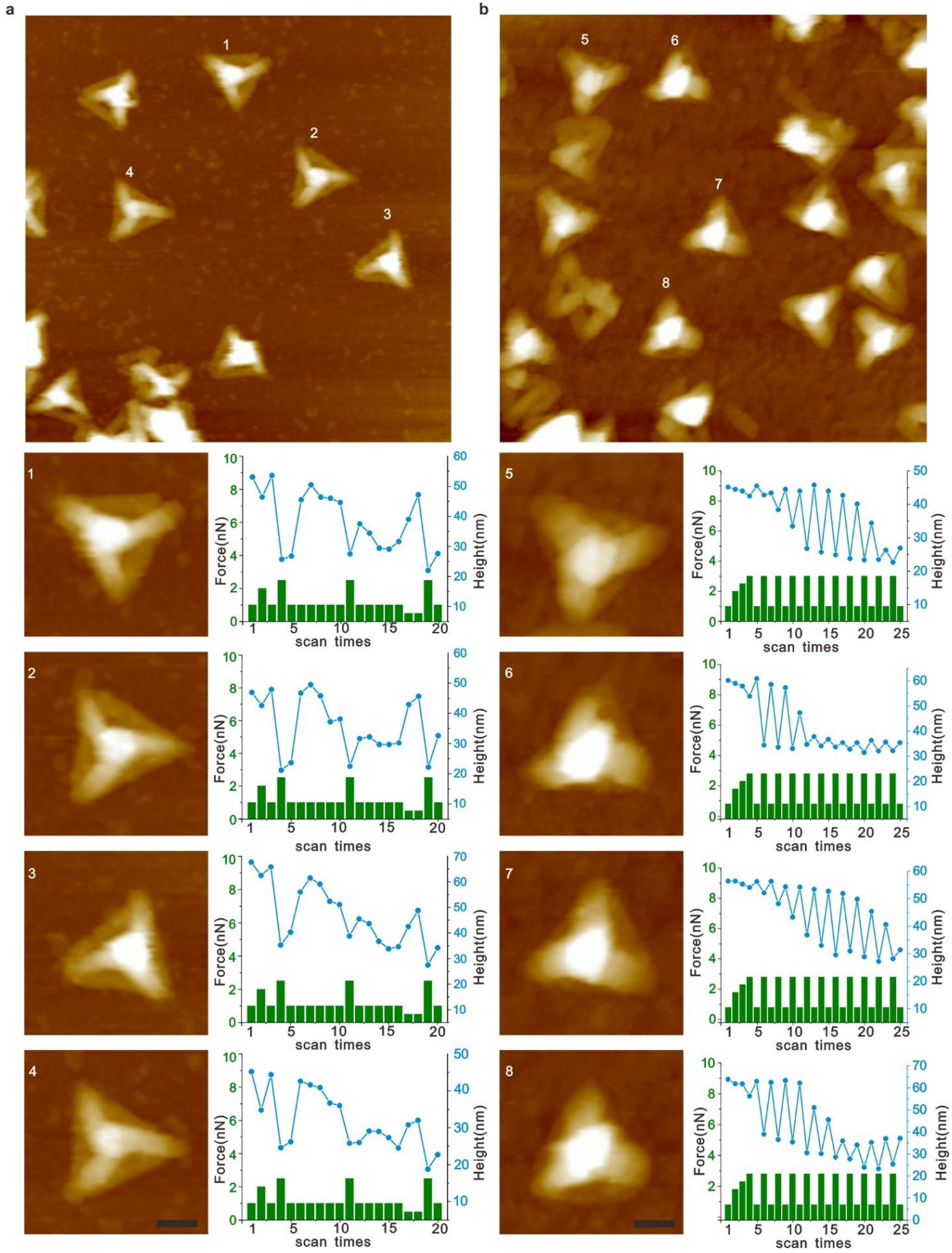

Figure 70 | Exemplary mechanical libraries of tough, yet flexible DOS tetrahedrons.

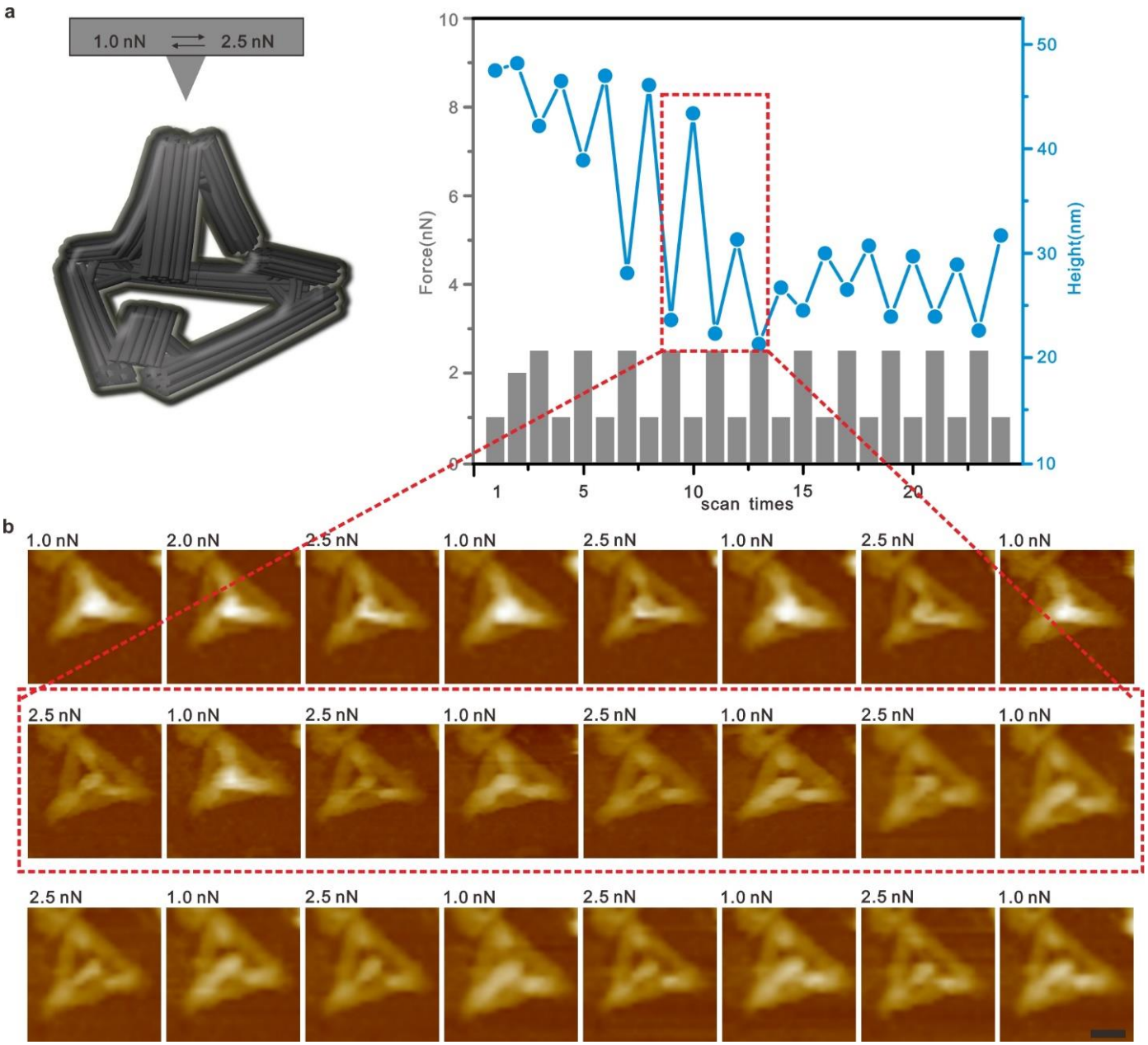

Figure 71 | AFM images and corresponding height changes for a 5-day DOS tetrahedron that was placed under a 1.0 nN and 2.5 nN cycling force. a. Generally, the height of the structures mostly recovered after the first several cycles. However, the heights did not recover after several cycles (red color). **b.** As shown in the AFM images in the middle row, the dramatically decreased recovery heights were due to a fracture in one of the edges. Scale bars, 50 nm.

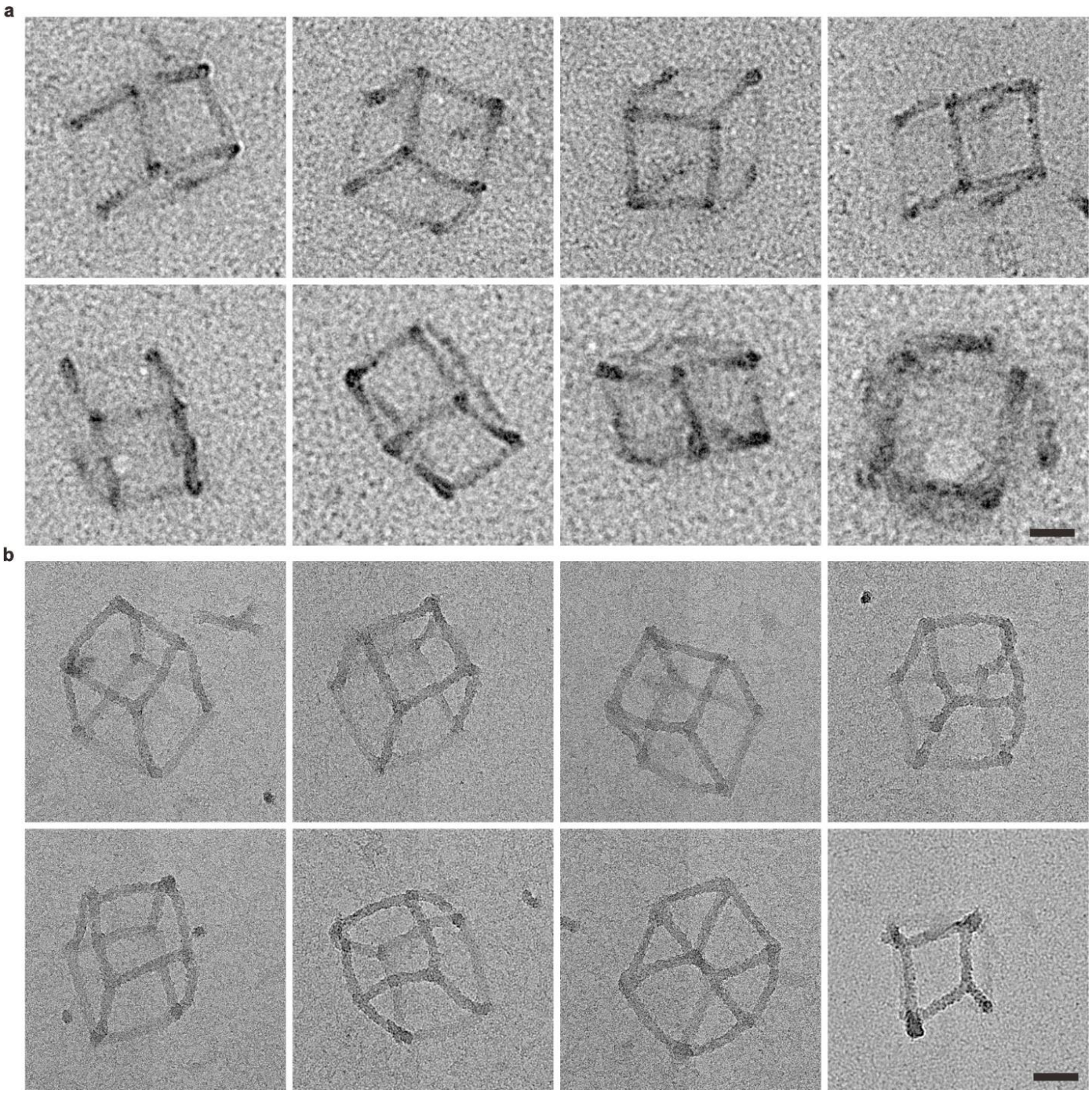

Figure 72 | TEM images of DOS cube that was reacted for 1 or 2 days. a and b. Because the cubic framework was not geometrically rigid, the results of a 1 or 2 days silicification time did not result in any obvious enhancements to the DNA origami's strength as compared with the strength of the DNA origami frames alone. The DOS cube would instantly collapse onto the substrate and was found lying down in random directions on the substrate. Scale bars, 50 nm.

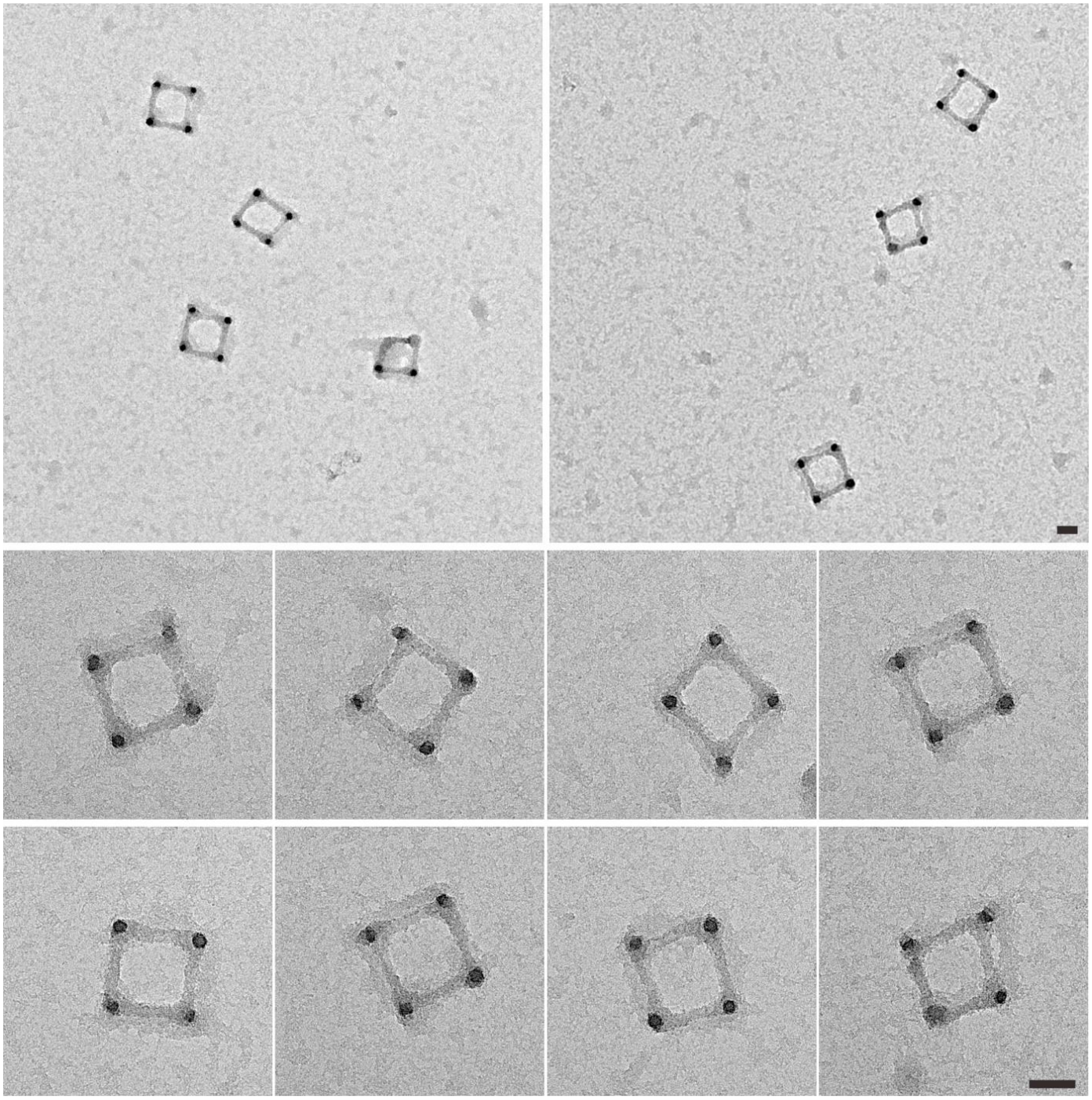

Figure 73 | TEM zoomed out/in images of DOS cube that was reacted for 5 days. After 5 days of silicification, the DOS cube was strong enough to stand freely on the substrate. The images show a typical top view of these cubic nanoobjects. The contrast of four vertexes were higher than the sides of the nanoobjects in every image because of the four standing side edges. Scale bars, 50 nm.

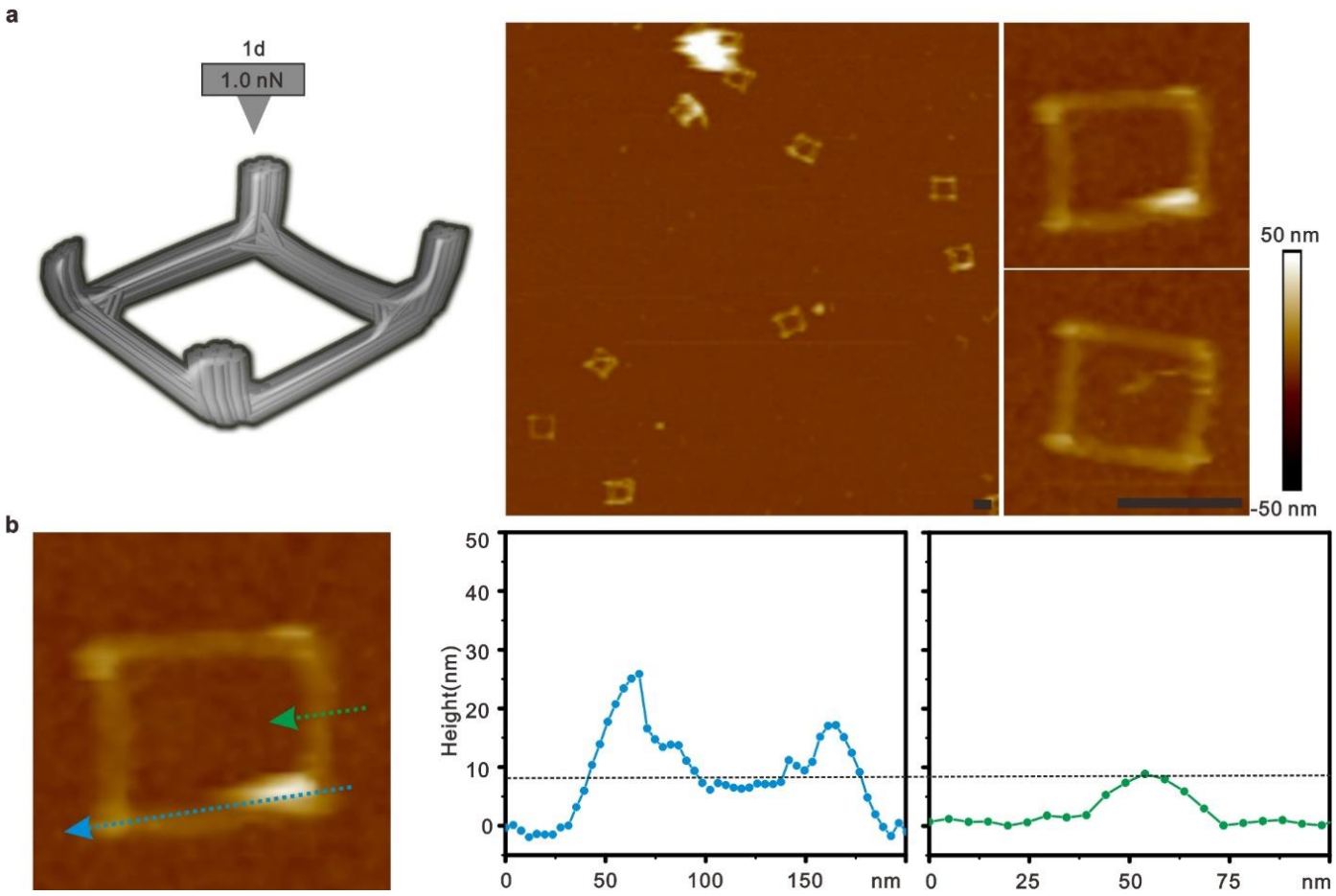

Figure 74 | AFM images of DOS cube that was reacted for 1 day under 1.0 nN. a. Many of the DOS cube had well-formed square shapes, but they were also often very short. **b.** Section diagrams revealed that the upper parts of the DOS cube were lost during the scanning process due to the poor mechanical strength of the standing edges. Scale bars, 100 nm.

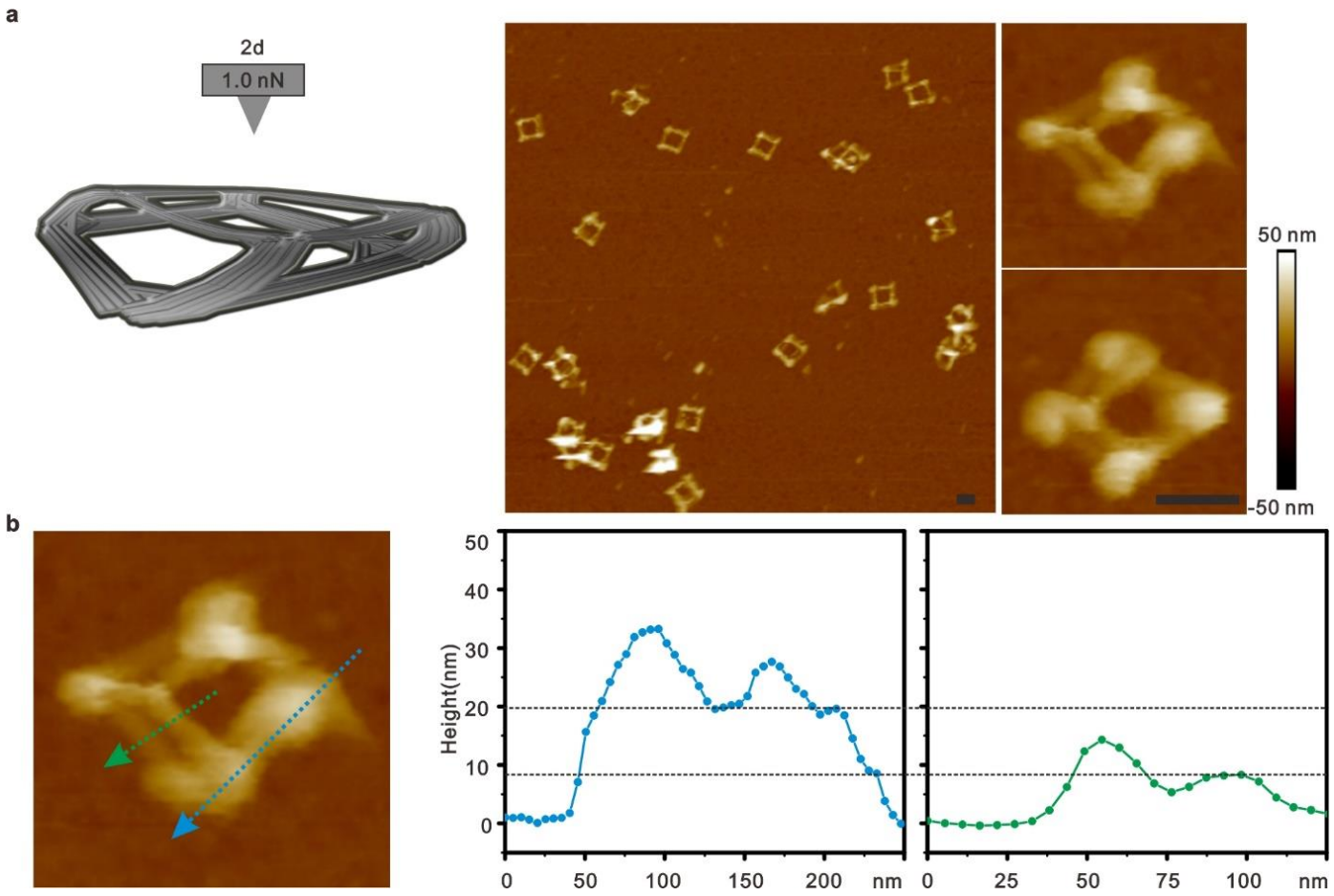

Figure 75 | AFM images of DOS cube that was reacted for 2 days under 1.0 nN. a. Many of the DOS cube had well-formed square shapes. They also had distinct, two-layered structures. **b.** Section diagrams revealed that the cubic DNA-diatom was intact, but the girder of it bent into a 'U' shape. Scale bars, 100 nm.

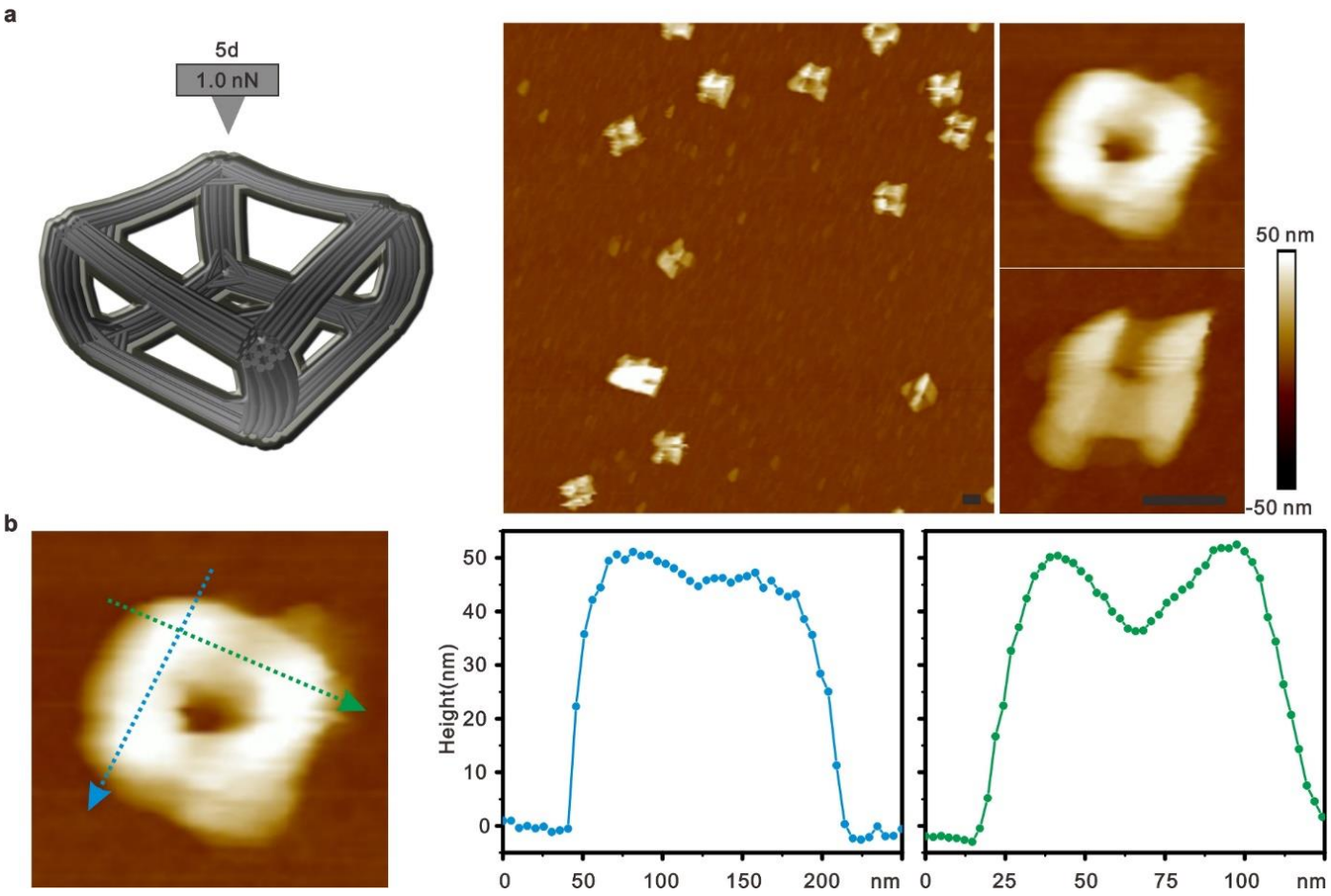

Figure 76 | AFM images of DOS cube that was reacted for 5 days under 1.0 nN. a. Many of the DOS cube had well-formed square shapes. They also had distinct, two layered structures. These structures were taller than the structures in the 1- and 2-day samples. **b.** Section diagrams revealed that the DOS cube was almost intact, and the girder was less bent, as compared to the 2-day samples. These results agreed well with the DOS tetrahedron and further proved that there was an obvious mechanical enhancement made as a result of silicification the DNA structures into DOS nanostructures. Scale bars, 100 nm.

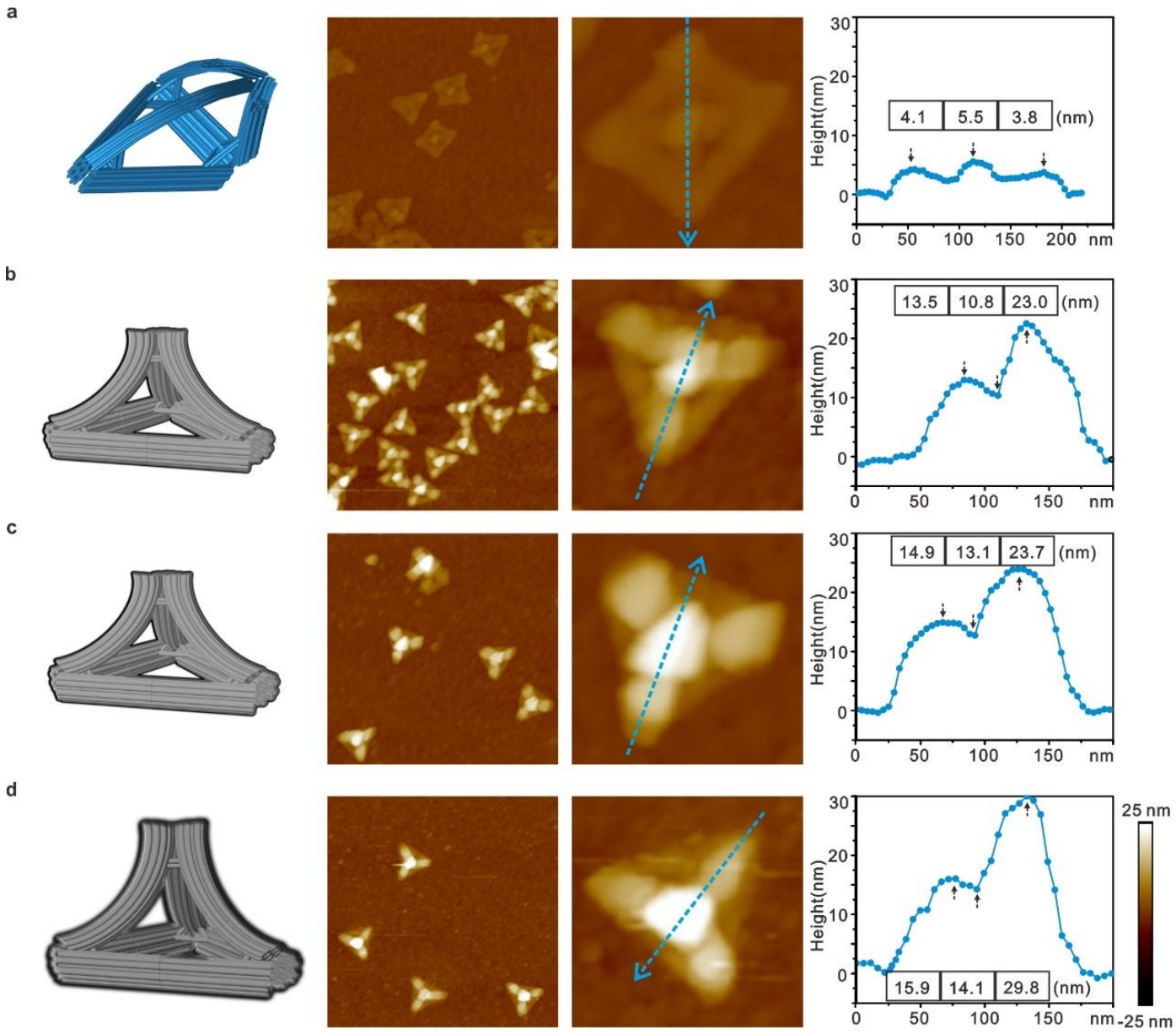

Figure 77 | In air AFM characterization results for tetrahedron DNA origami and corresponding DOS structures. a. AFM images for pure tetrahedron DNA origami in-air mode. **b. c.** and **d.** DOS structures that were mineralized for 1, 2, and 5 days. The peak heights for all of the groups observed in-air are significantly lower than that of the peak heights for the groups that were in fluid. Specifically, in-air the peak heights were,~ 5 nm, ~ 20 nm, ~ 22 nm and ~ 30 nm, while the in-fluid heights were ~ 20 nm, ~ 25 nm, ~ 40 nm and ~ 60 nm.

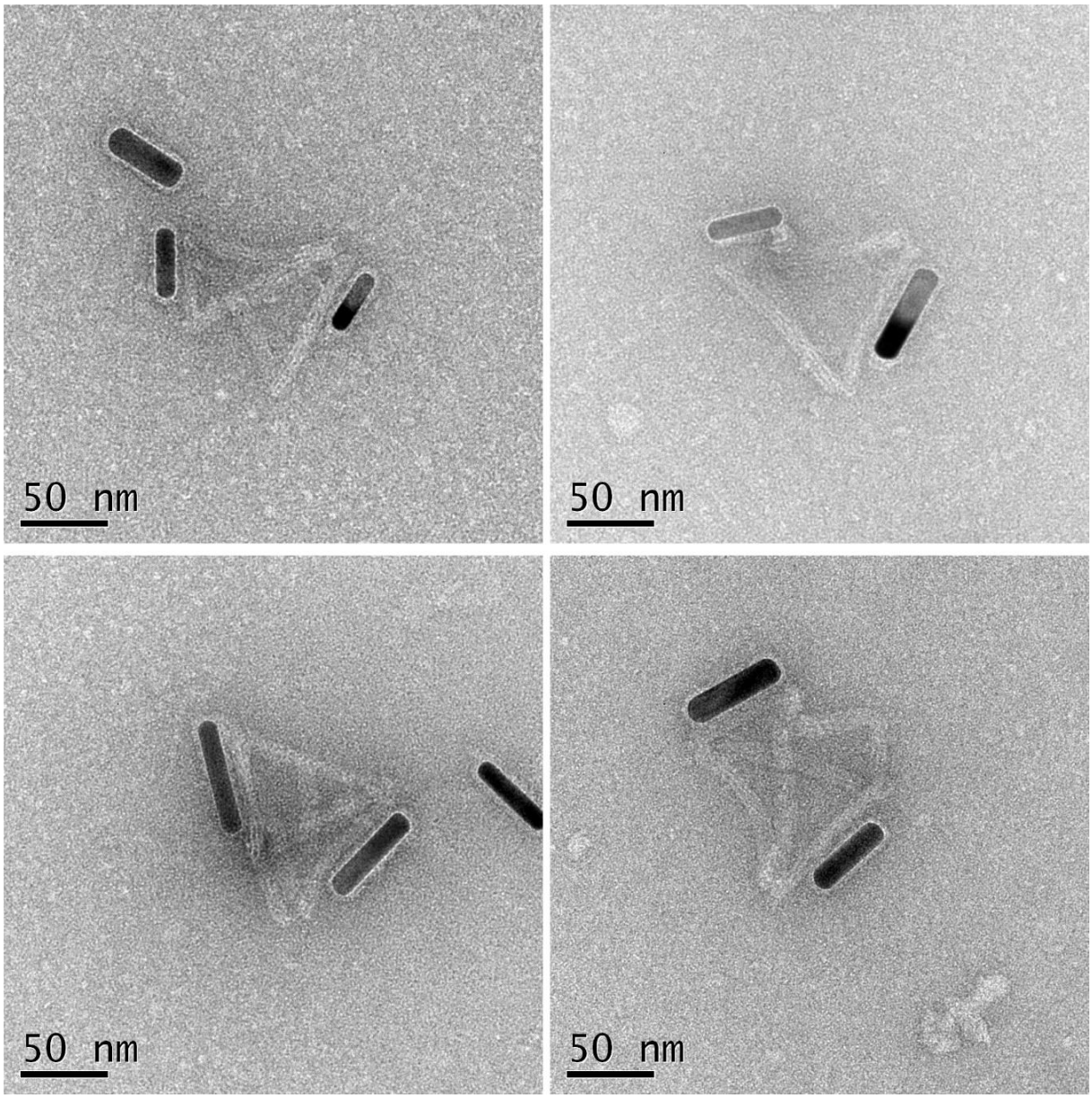

Figure 78 | Additional TEM images of pure DNA origami-AuNRs.

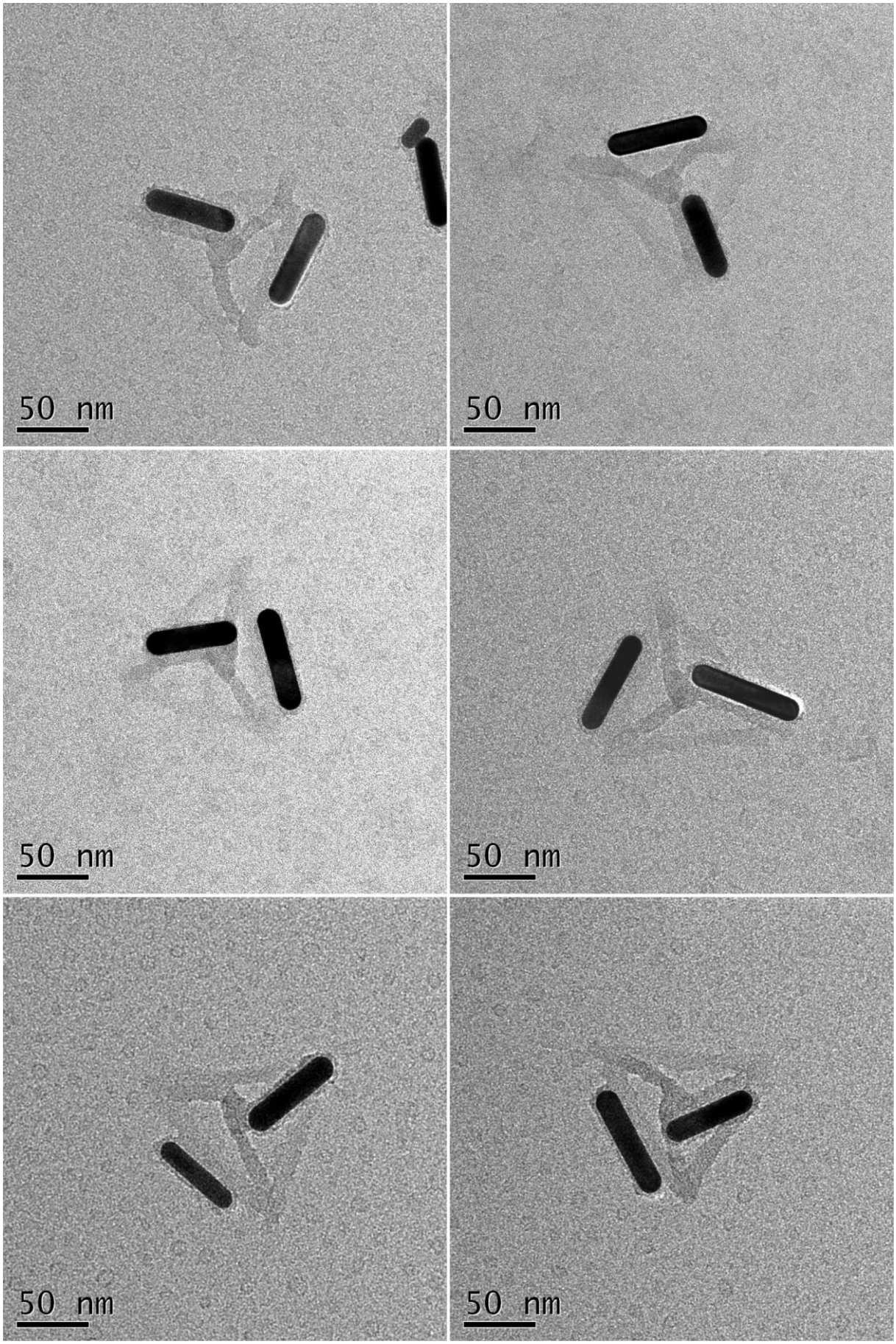

Figure 79 | Additional TEM images of DOS-AuNRs.

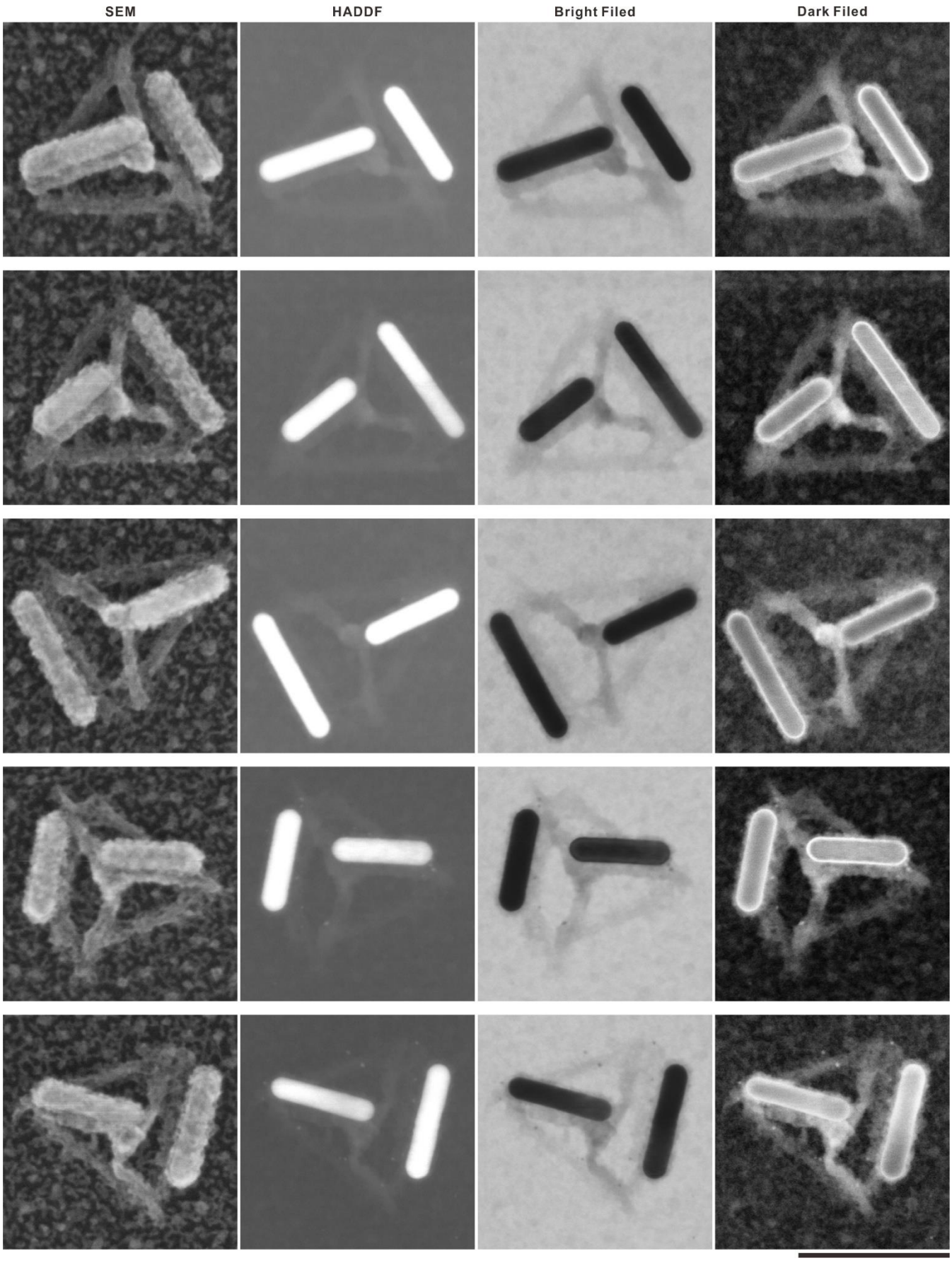

Figure 80 | Additional STEM images from four different signal channels of DOS-AuNRs. From left to right, SEM images reveled the surface situation of DOS-AuNRs, HADDF images revealed the elemental distribution of the structure, the heavier the element, the brighter the image. Bright and dark filed TEM images revealed more details of the silica shell. Scale bar, 100 nm.

DNA sequence of DNA-diatom

No.	Sequences
1	GCATAACCACTTCTCGAATAATAAGCATAAAGTGTAAAGCCGGCCAGTTTTCATTT
2	ATGTAGCCGGAATTTTTTCACGTTGAAAATCTCCAATTTG
3	TTCAGCTCCTTTTGATAAGAGGTCATTAAAAAAGGGCTCACAA
4	CTGGGTTATCCCTCCAAAAGGAGCCTTTAATTGCCTTTAATTTTCCATATAACAG
5	AAGCCAACAGGTCAGGATTAGAGAGTACCATTAAATCATAGCT
6	TTGATTCCAGAAGAGCAACTAACTCAGCTCCTCAGTTGAGATTGCAA
7	GCCCCTTCAAAGCGAACCAGACCGGAATAGGAATACAAAAGGA
8	AAGAATAACGCCCACATTCAACTAATGCAGATTG
9	CGATAAACGAATCGCGAGT
10	TCACTTTCATGATTGGTCACATTAAATGCGAAGCGATAACCGGAGTATCTCGA
11	GGAGCTGAGTTAATTTAATGGC
12	TGTAGCTTGGAGTAACAGAAGTGATCACGAAGAAGTG
13	GGTCGGCAGATACGGAA
14	ATTACGAGTTTACCAGTACCCTGAATCGTCATAAATATTCA
15	CAATTAGTAAAAACTATCATAACCCTCGGCATAGTAAGCA
16	GTTTCCTGTAATTCGTAGAGTAGATCTCTTCGCCTGGATAGCGTC
17	CGATCGGAAAGGGCGGGTACCGAGCTCGGTGAAATTAAGT
18	TTCCACACGACTCTAGTCGCAAATTAGTAGCATTGGAAGGG
19	CAGGTCAACATACGTTTAAATATGGCTTAGAGCTTAATTGCTG
20	ACCAGTTTTTAACGA
21	ATATGCCAAGCTGCCAGGGTTTTCCCAGTCACG
22	AAAGGTGGCATCAATTCTTGGGTAACTGCATGCCTG
23	CGGATGCAACTAAAGTACGATACATTAGGATCCCGGATGTGCTG
24	ATAGTCCAATTCTGCGAACATCATGGTTGTTTAGATA
25	ACTCGGATTGCATCAAAAAAGGTCTTACGACGATAAGAAGTTTT
26	TTGAATTTTGCAAAAAAACCAAAATAGCAGGTGC
27	CGAAGAAGCTTAGGTGTCTG
28	GAACCTTTTTAGCTT
29	AAAATATAACGTTGACGAGGAGGGTAAAGGATAAACA
30	TAAAACGAGAGGCTCCCCCTCACCATAAATCAAAAATCGATT
31	GCCAGAGGGGGTAAACTGCGGACTATT
32	TTACGCCAGCTGGCGTGCGGGCTTAGTTTGACCATTAGGTGT
33	CAAGGCGATTAAGTACTAATAGGGTCAATAACCTGTTTCAAC
34	CCAACGTCAACACTATTAAAGAACGTTTTTCGAGCTGA
35	AACGTGGCTTTTTATGCTGTAGCTAGCT
36	AATTCGAGGAAAGACTTCAAATATCC
37	ATAGCACCAAACATAAATCACGCGTTTT
38	GCTGGAGATTTTTAAATAATCTCTAATA
39	TCATACAGAAAACGAGAATGAAATGCTTTAAACAGTTGGCAGTCG
40	CGACCATTCAGTCGGAACCGAAGAATTTTTTCAAAGCG
41	TTGGAACTTCACCGGGTGGTTTTTCTTTTCCTGGGGTGCGGCG
42	CCGTCGGGAAAGCCCTAATGACTAAAGGAATTGCCGAGGATATATTCGGTCGCCGCCCAC
43	TGCCAAGCTAAAAACTTTTAC
44	CGAAACGACCCCCAGCGATTAACTTCTCAGGGA

45 TAGCCCATTAAAAATACCGACACACGACTTGATTAG
46 TAAAGCGTAACCACCACACCCGCCGCGCAAAAGTTTACAGACA
47 CCAGAAGGAGTTTTGCGGAACAAAGTTTTTCATCACTT
48 GCCTGAGTAGAAGAACTCCAATCGTCAAAGGGACAT
49 TACATTTTGACGCTAAACTATCATTAACCGTTGTAGCAGCGG
50 CGAACTGACAACAGAGTCACGCAAGGCCTTGCTGGTAATAT
51 ATATTTTTGCGTAAGAAAGTGAGGCCCGCCAGCGTGGTTCCGAAA
52 CCAGAAACGCTCACTTCTGACCTGAAAGAATGGCTACAGG
53 TAGATTAGTCTGAGTTTCGTCACCAGTACAAAGTTTAATGCGGTACGCCAGAATC
54 AACGCCGCTACAGGGCGCGTACTATGGGTAACACTTTAATGCG
55 GAGCAAACATCGAAGCCCAATAGGAACCCATGTACCTTGC
56 TCTGGCTAGCCCTATAAACAGGACGAGCACGTATAACGTGCTT
57 TTGCAACAGGAAAACAATATTACACCGAGTAAAAGAGTATTT
58 GGTCGATGTTTTTATAATCTACGTGGCGTTTGATGCA
59 TTTGAGGCCGATTAAAGGGCTGTCCAATAGAACCTGGAAATACC
60 TTCTCAGTAATATGAAATGGATTATTTACATTG
61 AAATCTTTTTCCAGT
62 GCGTAGATTTTTTTTAGAATCAGAATAC
63 CTGAGAAGGGTACCTGTCGTTAGCTTGGCATTTGCTAAACAACCACG
64 CCCCAGGGCGCTGGCAAGTGTAGCGGTTTTCAACACACTGCCC
65 AAGGTTGCGCTGTTTCAGCGGAGTGAGAATAGAACGGG
66 AGAAAGGAAGGGAAGAAAGCGAAAGGAGAGGAACAAGTGAGCT
67 AACTCACATGCGTATTGCGATGGCCGTTGAGTGTTGTTCCAGT
68 TAGCCCAGCGGTCGGGGAGAGGCGGTTTTAATTGCGGAGC
69 GCTTTCCAGAATCGGCTCAAGTTTCTTATAAATCAAAAGAA
70 TCGGAAAATCCTTGCCAGCTGCATTAATGTCGGGAAGCCG
71 CTGCGCACTAAATCGGAACACCCAAACAACGCGCCACGCTGGTT
72 CGCTGATTTAGAGCTTGACGTATCAGGGGGCGCCAGCCTGGCCCTG
73 GGGCAACAGCTGATTGCCCAAGAGTCAGGGCGAAAAA
74 AGAGAGTTGCAGCAGAGATAGGCACTACGTGAACCATCCCTA
75 TGCCCCAGCAGGCGCAAAATCCTTTGG
76 CAGAGCCTAATTTGCCAGTTACAAAATAACAGTTAATTAATTG
77 GAGTAAGTTATCTATATCTGGTCAGTTGGCACGAACCAAAATT
78 TCATAAAATAAAGCCAGCAGACCACCCTCATTTTCCGAGTACCAAGCG
79 CACAACGATCTCTAAATTACG
80 ATGGCAGACCGTGCACCCCCCA
81 ACGAGCATAAACGCAAGCCTCAACTTCTGATTTC
82 TTACAGTAATCCACGCTCTTAATCAATAAACAAAGT
83 AGAATCGCCTCCAGACGAGAACGCGAGCAAGCCGTTTTTATTT
84 ACTCATCATCCTAGGTAAAGTAATTCTGATATTTAAGCTA
85 CCCACAACGCCCTTGAGTAACAGTGCCCGTATAAAACA
86 CAATTATTATTTATCCCAATCCAAATAGTCAGTGCAACATGTA
87 ATTTAGGCTAAAGTACCTTGCGGGATTAAACCAAGTACCGC
88 CCAACAATAATCCAGTAATAAGAGAATAAGAGGCATTAAA
89 AGCCCAATCCTTTTCGAGCCGGTCTGCCATAAGTTTTAACGGGAGAA
90 ACGAGATTAGTTGCTATTTCTCCCGACGACAAAAATTTACGAGC
91 GCCATTTATCCTGAATCTTAGTATTCTAACGACAATTCCTGAACAA
92 TCATCGTAGATAAGAAACAACATGTTCAGCCGCTCAACAACGA
93 TAATGTTTTTTATTT

94 GCGCCTGTTTATCAACAATAGGAATCATAGAAGGCTT
95 GAAAAATAATATCCCGAGAACAAGGCGTTTTAGCGAACTGCA
96 ATGTAGAAACCAATGAACGGGTAGGTT
97 TTGAAGAATAAGAGCAAGAGAAGGTAAGGCTGTCTGT
98 TTTTTGGGGTCACTCATCCTTAATATTTTTAAGGAAAC
99 CGAGGAAACGCAATAATAAAAAGAAAATATGGTTTA
100 ATGTTAGCAAACGTGACTCCTTAATAGCAATAGCTATCCAGA
101 GATTAAAGAAAATGACATTCAACCGATTTTCATTAATAAC
102 CCAGCGAGCATCGGAGAGGGTAGAAGCGCATTAGACGGGAGAA
103 GAGAAGGTGAAATTAGAGCCAGCAAAATCACTGGAAATAGCAAAGAATTGAGTTA
104 CCACGCCTTTACAGAGAGAATAACATAATTTGGGATTATCACC
105 GTCACCGACCAAAGACAGCCCTTTCCCAAAAGAACTGGCAT
106 AGTCACTCAGATCTATTA
107 GTGGTTGAACCTTGAGCCAAAA
108 CAGGATTGAGCGCTAATATTTACCGAAAAAGGGCACATACATAA
109 CGGAAATTAGAGGGAGGAACAATGAATTACGCATTCCTTATCATT
110 TCAATTTTTTGTTTAACGTCAAAAATGAGGGGTGCAATATTGA
111 AGGTGGCAACATATACGGAATATTAAGAAAAGTAAGCAACAA
112 GCCGGAAAATTCCGCAAAGACACCACGGAATAA
113 GAGCTTTTTTGTCAC
114 CAAATCAGATATTACCGCGCCCAATTTTTTTTTAAGACG
115 ATCCGCCAACGCTAGTAGGGCTGCCCCCTGCCTACCGAGAATCCTCAT
116 GCGTCTTTTTTTTAACATCAAGAAGAAA
117 GAGCACATTTTTTGAACACCCTGAGATA
118 TAAAGCATTCACAAACAAATAACTTCTTTTCGG
119 AACCACCAGTATAAAGCCAATAGTTAATAGCGATAG
120 AAATAAATTCTTTATTATTCTGAAACATGAAAGTATTTTC
121 TTTAATCGCGCAGAGGCGAATTATTCATAAGAGGCTGTTTAGT
122 TTACAAAAGCCTGAGACTCCTCAAGAGAAGGACGGTTACAAAATGGAAACAGTAC
123 TAATTCGCCTGATTGCTTTGAATACCAATAATTTAGAACACCG
124 ATAAATCATTCTGAGAGCCAGATCGTTGTGAGTACCGCCACCCTAAC
125 ATTAACCTTTTACATCGGGAGAAACAATCAGAACCACACCGCC
126 ATATAGTATTAGCCACCCTCAGAACCGCCACCCTGTAA
127 TTCAGGTTTAACGTCAGATGAATATACACAGAGCCAAGATAAA
128 ACAGAGGTGTCAAACCCTATCAGATTATTAATTTTAAAAGTTT
129 CTTTGCCTAATAGGCTGAACCTCAAATAAGGCGGTCCAAA
130 TGCAACAGTCTAAAGCCTGATTGTACAACTCGTATTAAATC
131 ACAAATTTGAGGAGCAGCAAATGAAAAATGCCACGCTGAA
132 GGATGGAAGGGTTAGAACCTATAATCATCACCTTATTAGAGCCG
133 CAGTTTTGCACGTAAAACAGTTCCTGATTCAATCAAAAATATCTTT
134 TGAAAGGAATTGAGGAAGCATTATCACGGAATTATCA
135 AGGAGCACTAACAACCGAACGTGATGGCAATTCATCAATACC
136 TCAATAGATAATACACAATTCGTTGGA
137 TTATACATATATGTGAGTGTAAGAATAATTTAGAAGC
138 GAATCATAAGCGTTAAAAATAACCTAACCTCCGGTATTAGACTTT
139 AATTTTTAACAATTTCATTCGCTATTATACCGACTATGTAAATG
140 TTTAATCGTTATACTAATTACAACCTGAGCAAAAGAAGATGAT
141 CTGATGCAAATCCAGAATTTATTTCCCTTAGAATCCTTAACA
142 TTAGGTTGGGTTATACCTTTTTTGCTTCTGTAAATCGTTGAA

143 GAGACTATAACTACGTGTGATAAATAAGTTACTAGACTTT
144 ATCATATGGGTTTGAAAATTAATTCAAAATCATAGGTCTGA
145 ACATTTCATCTTACAAAGAACGCGAGAAAACTT
146 CTGAGAAGAGTCAATAGTATCGCAAGCTGACCTAAA
147 TTGAATGGCAGATTTAATACCAGCATCAATAACATCTTGGCGC
148 CCAGCAGAATTTTCAAAGGTCGCAAAGTAATTAAAATGTGGGG
149 TCGCGTATCAAGTTCAACAAGTAACTTGACTCATCCGAGACGCAGCG
150 AAGTAGCAACGGGATATAGGC
151 GTTGTATATCCCGCGATCTGT
152 AGGAGTCGCCGAAAATTTTTAACCTGACACACTCAATCTTTTAATCAGAAACCATCATG
153 ATAATCTCGGTGCATATCAAGCAACCATTAAGCTCAGGAAATG
154 AGCACGCTTTCTGCAAGCATCTCATTTTGAAACCTGAAAC
155 CCAGCTGTTGCAGGTTTTACCTCCAAATGAAGAACCCA
156 AAAATACAGTATTGTTATCGGTAGCAAGTCATAAGTTGGAAAG
157 ATTGGTGTTCCTTCTGAGCCTGCAGAGGAAGCATCAGCACC
158 ACCACTCTTTTTAACGCGAGCAGTAGACTTTCCATAAGTC
159 ACCATGAAAGAATAGACGCGGATATACAACGACGGTTGTCAGCGCAC
160 ATCAACCAGCTTTAGCCATAAGTGCCTTGATAAGATTGTCCAGT
161 TGCCCTAGGGGCGGCCTCATAACCAAATACCTGGTCTCTCATTTTG
162 CAGCAGTTTTTGAGTTTCGTATTCTGGCGTGAGCTTGAGGAAC
163 GAAGTTTTTTGCAGC
164 CTGAATGCCAGCAATCTCCAAGATAAACTTGCCACCA
165 CATCTCGGCAATCTCTCCCAAGTTATCAGAAACGGCAGAGCA
166 TGCATTTTAGTAAGTACCAGCAACGTA
167 CCTTCAACCAACATAAACGCTACCGCGGATTCTCAGA
168 AACCAAACAGGCAAAAAACCACCATTGAATTATGGC
169 TTAGCGGCGTTGACCCAACAGACGGCGTACGGGGAAGGGGCA
170 TCAGCAAGATGTAGATTAAACTCCTAAGCCTCAGCGGTAG
171 GAGAAATTCGGCGTCTGATTCAGCAAGAGCAGAAGCAATACCG
172 TTTAGCAAAAAACACTGGTCATAATCATGGTGACTTTTGACCAAAGTTAGACCAA
173 CGGTGCCTCCAAACAATTTAGACATGGGACTGGAATTAAAATT
174 TTTACCGCTAAAAGTCTAGTCACACGGCATCAAAAGCAATA
175 TAACTATAACCTCTATTCCACTGCAACAACTGAACGCGCC
176 ACCAGCGAAACCAATCCGCACGTCAATGAAACATTCCATCTGAA
177 TGGTCAACCCAGAAAACTTATTGCCAACAACCTAATCCGGCGTCA
178 CTTTCCTTGAATGCCACCGGAGGCGGCTAGATCGCGCTTCGCT
179 TGCAATGAAGAAAATTTAGGGTCAGTCCTTGACGGTATTTAA
180 ACCAAAAAGTTTACCAGCATTAACCGTCAAACT
181 TCAGCGGCAGTCACGAGTATCCTTTTTTTTGAGGCATG
182 AGTCCCAGGGTTAGTAAGCATATGGTA
183 ACGCTGCCGAGTCTGTTGAACACGACCAGAATG
184 ATTAGAGCTTTTTCGGTTATCCATATAA
185 TTTATAGGACTTCTCATGAAGTAATACTGACCAGCCGTTTATCAGTGAGCCTCCAA
186 TTATTGGTAAAATCACGTTCTTGGTCAGTATGCAAATACG
187 ATGCATTATCGAACTCAACGCCCTGCATTAGCATAGAGTCATT
188 GAGTACCTTGCAGCAGCTTGCAGACCCATAATGCATATCACCCACAAGCCTCAAT
189 CTAAGCAGCCTTATGGCCGTCAACATACCTATATCCTGAACTA
190 AGCAGGTTTCGGTGCCAAGCGTTGCTACTTTGAATGAGCTTAACGTC
191 GTGGAACAGATACAAACTCATCACGAATAGAGGCCTATCTAAA

192 TCGGTGACTCAAAAGCGGTCTGGAAACGTACGGATTCT
193 GTAGCATTGTGCCAATTCATCCATTAACTTGTTCAGAGAATCT
194 CTACCATGATCGTTAGTTAAGAGGGGATAAAACTCGGAGGCCT
195 TGCGTCCGATTTACAGTTTTTGACAGAAACAAAATGGGCG
196 CCAGTCCTTCCTCATCAAACTGCGCCGAAAGTGTTAACTTC
197 CATCCCTGCTTTCATATTAAGCCACTTCTGACGAACTTCT
198 AGAAAAACCATTTTTCGTCTGCGGCACAACGCGTATTCGTAAAC
199 CAGTTCTATAGTGTTATTAAAATATCCTTGATGGCGTCATTTTCCG
200 GCTGCGCAAGGATAGGTCATCTTGAAAATTATACTCA
201 CCAGCAGTCCACTTATGGAAGCCGTTCAGCAGCCAGCTCCCT
202 AAGCAGTAGTAATTAGAAATATTAACC
203 GTCTTCTAAGAGCCTCGATTTTGCTGAATCAAGATAT
204 AGTCAACCTATTCTGCGACGCTCAACCAATACCAATTTTTCGACT
205 AAAAAGCATTGGGGATTGAGTGACATATATGAGAAATTGTTCCA
206 TTGCAGTTGGTCATGGAAGCCAGACAGAATCTCTTCCAAGAGC
207 AGTATCGGCAACAGGGTGTCAAGTAATAAGAACGAACCCTGC
208 CAGCTTTACCGTCTAATTAGAGAGTCAAAATAATCAGCGAAA
209 TAGACATTCCAGAAGAGCCATACCGCTGCAGCACTAAGAA
210 TCTTTGATTAGCGCCATCAGAAGGTCCTGACGGTTATTTCC
211 AAAACGACATTAATACCATGAAAAATATCAACC
212 AAAACATACAATTGGGAGCTTTATCAGAAATATCCT
213 TAATTTCACAAGTAAGGGGCCGAGACATAAT
214 GTCAATAGATAGTCTCAGGAGTTTTTGAAGCGGAGCCGGCAGAAGCC
215 TTATCCTACTTTAATCATTGTGAAGATGGTT
216 GTATCGGTTTGAAGA
217 TAGTAATTTTTATTGGGCTTGATTACCTTATGTTTTTCGATT
218 TTAAGCAGCTTGATACTTTTTCGATAGTTGCGGCCG
219 ATTTCTTAAAAACTGGCTCA
220 AGGACGTTGGATCAGCTTGCTTTCGAGGTGATTATACCAGTC
221 AAAATCTTTTTTACGTTAATAAGAAAGATTCA
222 GGAAAGGCAACATTATTACAGGTAAACGAAC
223 TAACGGAATCATGCGGCATACGCCCAAGATG
224 ACAACAACCATTGAGGCTTGCAGGGAGTTAAAGCCGACAATG
225 CTTTTGTTTTTCGGGATCGTCGGGTA
226 CAGACGTGACAGCATCGGAACGAACCCTCAG
227 CTACAACGCCCGTAACGATCTTTTTTAAAGTTTTGTCTGTATGGGAT
228 CAGCGAAATAGTAAATGAATTTTCGTCTTTC
229 GCCACTACAGCCCTCATAGTTAGTGTAGCAT
230 TCCACAGACGAAGGCACCAACCTTACGTAAT
231 GCAACGTTTTTGCTACAGAGGTAACAAAGCTGTTTTTCTCATTCAGTACGAG
232 CAAATCAACGCTTTGAGGACTAAAGACTTTTTATTCATTACC
233 TCATGAGGAAAAGAACCGGA
234 CAAGAGTTTTTTAATCTTGACGTTTCCATTAATTTTTACGGGTAAAAAAAAC
235 GAAAGATTTTTGGCAAAAGAATCATC
236 CACTCATCTTTAAAGTACAACGGAGATTTGTATACACTAAAA
237 GCCTGATTTTTTAAATTGTGTCGGAA
238 CGGAATACTCCATGTTACTTAGCCGAAATCC
239 TTAGGATTAGCCGTCGAGAGGTTTTTGTTGATATAATCAGGAGGTTT
240 GCGACCTGGGTGTATCACCGTACGTATAGCC

241 CCACCACACCAGGCGGATAAGTGCGGGGTTT
242 CAGTAGCACCAATGAAACCATTTTTTCGATAGCAGCGTACTGGTAAT
243 TGCTCAGTCAGAGCCGCCGCCAGCACCAGAA
244 GCCGCCATTGACAGGATTTTTGGTTGAGGCATGAAT
245 TTGGCCTTGATCAGAATGGAAAGCGCAGTCTCGGTCAGACGA
246 TTACCGTTTTTTTCCAGTAAGCCTTT
247 ATCAAGTTTGCGTCATACATGGCTTTTGATGGTAGCGACAGA
248 ATACAGGAGTACCGTAATCA
249 ATGACGGCGCCGGAAACGTCACCATTACCAT
250 TAGCAAGAGCAATAAACTCAACAAATAAGCA
251 AGCGTCTTTTTAGACTGTAGCCTTATTAGCGTTTTTTTTGCCATCTTACCAC
252 TCCATGATTTCGGTCATAGCCCCGCGTTTTC
253 ATCGGCATTGAGACAGGCCGTTTCAGCGCCT
254 CAGAGCCTTCATAATCAAAATCGTTTCCTG
255 CGCGTACACAGTAAGAACGTCAGTACCGGAAC
256 CGGAACTTTTTCGCCTCCCTCAGCCACCACCCTTTTTTCAGA
257 GGGAACCGAACCGCCACCCTCAGAGAGCCGC
258 CACCCTCAGAACTGACCAACTTTAATCATAA
259 CGAGGCTTTTTGCAGACGGTCGAAAGAGGACATTTTTGATGAACGGTTTCAT
260 TCACTCCTATAGGCTGGCTGACCGTACAGAC
261 CAGGCGCTCCGCACGTAATTTTTACATTACA
262 TGCGGACGACGAGAAACACCAGAGAATAAGG
263 CTTGCCCTGACCAGGGCGAGCGCGCAACGGC
264 CTGACCTTTTTAGCAAGGAAGTCGGCGCCAGTTTTTTTTGAATATTAAGCCC
265 CTGCAATTTTTTTAAAATTGTGGCATTAACACTTTTTCATCCTTCATACGAT
266 GGAGAGGAGTTGACCACCTA
267 CGAGCGCCTTAACCAGTAGTGTTAACAGTCGCATACCAAAGA
268 GCGGCATTTTTTGGTCAATATTACGCTTGCCTTTTTTTTTAGTACCTCCAGAA
269 CGTTTTTTTTTTTACCTTTAGGACGCACGTTTTTTTTTCTTCTGCGTCGCAA
270 GGTAAATTTTTCGCGAACAATCCTGAAACAAATTTTTTGCTTAGGGAGAAAA
271 TTCAAATAACTCAGCGGCTTTAACCGGACGCTGTTATAGATA
272 TCGACGCCATTTAAAATAGT
273 AGGCATTTTTTCCACGGCGCTTAATAATGTTTTTTTTTCCGTAAATTGAATG
274 TTGACGTTTTTGGATGAACATGGAGCAGGAAATTTTTGCGAGGGTATCAAAC
275 CCAGCGTACCACGAGAGCGGTCAGTAGCAATCCCCACAAAGT
276 TTTGTTTTTTTACTCGTCAGAAAACCATAACGTTTTTAGCATCATCTCGGTC
277 GCAGCAACGGAAATCGAAAT
278 TTTTTGAGATGCATCTTCGGTTAAATCCAAAAAGTCCAAATG
279 GAAAGCTCGTGGTAGAAGTCGTCAAACGAAC
280 GCGAATAAGTTCCTGAATGAATTTTTTGGGAAGCCTGACAAGTAAAG
281 AAGCGCAATCGCAGTAGGCGGAATTTGGCGA
282 TTTAGGAGTAAACATATTTTTGTGCCATGCTTTTGG
283 GAAACGCGGCACAGAAAACTGGCCTAACGACGCAGGAACAAA
284 TCAGTTTTTTTCCATCAACATAAGGC
285 GAAACATACGCATAGCCAGA
286 TAGAGCGCATTCAAGAAGGTGATAAGCAGGATGCCCAGAGAT
287 CTACAGTATCACCAGAAGGCGGTACGCGTTC
288 TTGCAAAGAGTCAATAGCAAGGCAAAAATGT
289 GCATAATTTTTCGATACCACTTCACCAGAACGTTTTTGAAAACATCCATACA

290 TCCACTGAAACTTCTTAGACGAAGACCCTCA
291 GCAATCTTTTCACCATAAACGTGGAACTTAA
292 GTATCAGGCGGCGGCAAGTTGCCTTCATAGA
293 AATTTCACGGTTAATCGTGCCAATTTTATTG
294 AAACAGTTTTTGGTCGCCAGCTAAGGTACTGATTTTTATCTC
295 CTCATTAAAAGCACCTTTAGCGTAATATCGG
296 TATAAGTCGGGTTAGCCTCGGTATGATTAAG
297 GAGGGATTTTTCATAAAAAGTCACGACGCAATTTTTTGGAGAAAGACCCAAT
298 CCAACGGCGTCCAGTTGAAATGGTAATAAGACGAGGAGAGCG

References

1 Williams, S. *et al.* Tiamat: A Three-Dimensional Editing Tool for Complex DNA Structures. *Lect. Notes Comput. Sc.* **5347**, 90-101 (2009).

2 Rothemund, P. W. Folding DNA to create nanoscale shapes and patterns. *Nature* **440**, 297-302 (2006).

3 Han, D. *et al.* DNA origami with complex curvatures in three-dimensional space. *Science* **332**, 342-346 (2011).

4 Iinuma, R. *et al.* Polyhedra self-assembled from DNA tripods and characterized with 3D DNA-PAINT. *Science* **344**, 65-69 (2014).

5 He, Y., Tian, Y., Ribbe, A. E. & Mao, C. Highly connected two-dimensional crystals of DNA six-point-stars. *J. Am. Chem. Soc.* **128**, 15978-15979 (2006).

6 Wang, P. F. *et al.* Programming Self-Assembly of DNA Origami Honeycomb Two-Dimensional Lattices and Plasmonic Metamaterials. *J. Am. Chem. Soc.* **138**, 7733-7740 (2016).

7 Liu, W., Zhong, H., Wang, R. & Seeman, N. C. Crystalline two-dimensional DNA-origami arrays. *Angew. Chem. Int. Ed.* **50**, 264-267 (2011).

8 Mathieu, F. *et al.* Six-helix bundles designed from DNA. *Nano Lett.* **5**, 661-665 (2005).

9 He, Y. *et al.* Hierarchical self-assembly of DNA into symmetric supramolecular polyhedra. *Nature* **452**, 198-201 (2008).

10 Ye, X. C., Zheng, C., Chen, J., Gao, Y. Z. & Murray, C. B. Using Binary Surfactant Mixtures To Simultaneously Improve the Dimensional Tunability and Monodispersity in the Seeded Growth of Gold Nanorods. *Nano Lett.* **13**, 765-771 (2013).

11 Sweers, K., Werf, K. V. D., Bennink, M. & Subramaniam, V. Nanomechanical properties of α-synuclein amyloid fibrils: a comparative study by nanoindentation, harmonic force microscopy, and Peakforce QNM. *Nanoscale Res. Lett.* **6**, 270 (2011).

12 And, J. D. & Radmacher, M. Measuring the Elastic Properties of Thin Polymer Films with the Atomic Force Microscope. *Langmuir* **14**, 3320-3325 (1998).

13 Zhao, Y., Ge, Z. & Fang, J. Elastic modulus of viral nanotubes. *Phys. Rev. E. Stat. Nonlin. Soft. Matter. Phys.* **78**, 031914 (2008).

14 Derjaguin, B. V., Muller, V. M. & Toporov, Y. P. Effect of contact deformations on the adhesion of particles. *J. Colloid. Interf. Sci.* **53**, 314-326 (1975).

15 Hertz, H. Ueber die Berührung fester elastischer Körper. *J. Reine. Angew. Math.* **1882**, 156-171 (2009).

16 Doerner, M. F. & Nix, W. D. A method for interpreting the data from depth-sensing indentation instruments. *J. Mater. Res.* **1**, 601-609 (1986).

17 King, R. B. Elastic analysis of some punch problems for a layered medium. *Int. J. Solids. Struct.* **23**, 1657-1664 (1987).

18 Zlotnikov, I., Zolotoyabko, E. & Fratzl, P. Nano-scale modulus mapping of biological composite materials: Theory and practice. *Prog. Mater. Sci.* **87**, 292-320 (2017).

19 Maier, J. A. *et al.* ff14SB: Improving the Accuracy of Protein Side Chain and Backbone Parameters from ff99SB. *J. Chem. Theory. Comput.* **11**, 3696-3713 (2015).

20 Li, P. & Jr, M. K. Taking into Account the Ion-induced Dipole Interaction in the Nonbonded Model of Ions. *J. Chem. Theory. Compu.* **10**, 289-297 (2014).

21 Pérez, A. *et al.* Refinement of the AMBER Force Field for Nucleic Acids: Improving the Description of α/γ Conformers.

Biophys. J. **92**, 3817-3829 (2007).
22 Darden, T., York, D. & Pedersen, L. Particle mesh Ewald: An N·log(N) method for Ewald sums in large systems. *J. Chem. Phys.* **98**, 10089-10092 (1993).
23 Berendsen, H. J. C., Spoel, D. V. D. & Drunen, R. V. GROMACS: A message-passing parallel molecular dynamics implementation. *Comput. Phys. Commun.* **91**, 43-56 (1995).
24 Yesylevskyy, S. O., Schafer, L. V., Sengupta, D. & Marrink, S. J. Polarizable water model for the coarse-grained MARTINI force field. *PLoS. Comput. Biol.* **6**, e1000810 (2010).
25 Bussi, G., Donadio, D. & Parrinello, M. Canonical sampling through velocity rescaling. *J. Chem. Phys.* **126**, 014101 (2008).
26 Berendsen, H. J. C., Postma, J. P. M., Gunsteren, W. F. V., Dinola, A. & Haak, J. R. Molecular dynamics with coupling to an external bath. *J. Chem. Phys.* **81**, 3684-3690 (1984).
27 Liu, B., Cao, Y. Y., Huang, Z. H., Duan, Y. Y. & Che, S. N. Silica Biomineralization via the Self-Assembly of Helical Biomolecules. *Adv. Mater.* **27**, 479-497 (2015).
28 Bustamante, C., Bryant, Z. & Smith, S. B. Ten years of tension: single-molecule DNA mechanics. *Nature* **421**, 423-427 (2003).
29 Wang, T., Schiffels, D., Cuesta, S. M., Fygenson, D. K. & Seeman, N. C. Design and characterization of 1D nanotubes and 2D periodic arrays self-assembled from DNA multi-helix bundles. *J. Am. Chem. Soc.* **134**, 1606-1616 (2012).
30 Luan, B. & Aksimentiev, A. DNA attraction in monovalent and divalent electrolytes. *J. Am. Chem. Soc.* **130**, 15754-15755 (2008).
31 Qiu, X. *et al.* Inter-DNA attraction mediated by divalent counterions. *Phys. Rev. Lett.* **99**, 038104 (2007).
32 Pontoni, D., Narayanan, T. & Rennie, A. R. Time-Resolved SAXS Study of Nucleation and Growth of Silica Colloids. *Langmuir* **18**, 56-59 (2002).
33 Rimer, J. D., Lobo, R. F. & Vlachos, D. G. Physical basis for the formation and stability of silica nanoparticles in basic solutions of monovalent cations. *Langmuir* **21**, 8960-8971 (2005).
34 Surwade, S. P. *et al.* Nanoscale growth and patterning of inorganic oxides using DNA nanostructure templates. *J. Am. Chem. Soc.* **135**, 6778-6781 (2013).
35 Surwade, S. P., Zhao, S. & Liu, H. Molecular lithography through DNA-mediated etching and masking of SiO2. *J. Am. Chem. Soc.* **133**, 11868-11871 (2011).
36 Sun, W. *et al.* Casting inorganic structures with DNA molds. *Science* **346**, 1258361 (2014).
37 Estrich, N. A., Hernandez-Garcia, A., de Vries, R. & LaBean, T. H. Engineered Diblock Polypeptides Improve DNA and Gold Solubility during Molecular Assembly. *ACS Nano* **11**, 831-842 (2017).
38 Agarwal, N. P., Matthies, M., Gur, F. N., Osada, K. & Schmidt, T. L. Block Copolymer Micellization as a Protection Strategy for DNA Origami. *Angew. Chem. Int. Ed.* **56**, 5460-5464 (2017).
39 Zhou, X. F. *et al.* Radial compression elasticity of single DNA molecules studied by vibrating scanning polarization force microscopy. *Phys. Rev. E* **71**, 062901 (2005).
40 Kim, H., Surwade, S. P., Powell, A., O'Donnell, C. & Liu, H. Stability of DNA Origami Nanostructure under Diverse Chemical Environments. *Chem. Mater.* **26**, 5265-5273 (2014).
41 Chopra, A., Krishnan, S. & Simmel, F. C. Electrotransfection of Polyamine Folded DNA Origami Structures. *Nano Letters* **16**, 6683-6690 (2016).
42 Ponnuswamy, N. *et al.* Oligolysine-based coating protects DNA nanostructures from low-salt denaturation and nuclease degradation. *Nature Commun.* **8**, 15654 (2017).
43 Lacroix, R., Kermouche, G., Teisseire, J. & Barthel, E. Plastic deformation and residual stresses in amorphous silica pillars under uniaxial loading. *Acta. Mater.* **60**, 5555-5566 (2012).
44 Hogan, M., LeGrange, J. & Austin, B. Dependence of DNA helix flexibility on base composition. *Nature* **304**, 752-754 (1983).
45 Alessandro, B., Concezio, F., Maria, A. M., Vittorio, G. & Massimo, G. Raman and infrared spectra on silica gel evolving toward glass. *J. Non-Cryst. Solids* **48**, 117-128 (1982).
46 Shiv, K. S., Joseph, F. M. & Malcolm, F. N. Raman investigaion of configuration in vitreous silica. *Nature* **292**, 140-141 (1981).
47 Goodman, R. P. *et al.* Rapid chiral assembly of rigid DNA building blocks for molecular nanofabrication. *Science* **310**, 1661-1665 (2005).